Radial electron fluence around ion tracks as a new physical concept for the detection threshold of PADC detector

Tamon Kusumoto

KOBE UNIVERSITY
UNIVERSITÉ DE STRASBOURG

Graduate School of Maritime Sciences, Kobe University
Laboratory of Radiation Science & Application
École Doctorale de Physique et Chimie-Physique
Institut Pluridisciplinaire Hubert Curien – UMR CNRS 7178

Doctoral Dissertation

Tamon Kusumoto

December 15th 2017

Doctor from Kobe University
Doctor of Philosophy in Engineering
Doctor from Univerité de Strasbourg
Doctor of Philosophy in Physical Chemistry

Radial Electron Fluence around Ion Tracks as a New Physical Concept for the Detection Threshold of PADC Detector

Thesis directed by:

Tomoya Yamauchi	Prof., Kobe University
Rémi Barillon	Prof., Université de Strasbourg

Member of juries:

Yvette Ngono-Ravache	Dr., CIMAP-CIRIL-Ganil (rappporteur)
Mitsumasa Taguchi	Dr., QST Takasaki (rappporteur)
Michel Fromm	Prof., Université de Franche-Comté
Keiji Oda	Prof., Kobe University
Hisaya Kurashige	Prof., Kobe University
Koji Kuraoka	Prof., Kobe University

Doctoral Dissertation

Radial Electron Fluence around Ion Tracks as a New Physical Concept for the Detection Threshold of PADC Detector

Fluence radiale d'électrons autour de la trace d'ions nouveau concept pour le seuil d'enregistrement du détecteur de traces PADC

PADC 検出器の閾値に対する新しい物理指標としてのイオントラック内径方向電子フルエンス

January, 2018

Graduate School of Maritime Sciences, Kobe University
Ecole Doctorale de Physique et Chimie-Physique,
Universite de Strasbourg

Tamon Kusumoto

Abstract

Fourteen years have passed since the discovery of poly(allyl diglycol carbonate), PADC, as an etched track detector (ETD) with excellent track registration property. Owing to its high sensitivity and the smooth surface even after the heavy chemical etching, PADC has been utilized in various branches of science and technology such as space radiation dosimetry, nuclear physics, neutron dosimetry, radon detections, decommissioning of nuclear faculties, inertial confinement fusion experiments, laser driven ion acceleration experiments and so on. While PADC is highly sensitive to energetic protons and heavy ions, it has no response to the low Linear Energy Transfer, *LET*, radiations such as X-ray, and electrons in practical terms. This unique feature makes it possible to identify the ion species and the energies even in a complex mixed radiation fields, like space and intense laser plasma. Namely, PADC has high sensitivity to ions, and it also has an appropriate detection threshold on the *LET* of radiations. From this aspect, PADC is clearly different from the Nuclear Emulsion and the Fluorescent Nuclear Track Detector as a radiation detector. Nowadays, the application fields of ETDs are spreading out but there remain several unknown points about the structure of latent tracks and its formation mechanism.

In this study, the latent track structure formed in PADC by protons and heavy ions has been examined, covering the stopping powers ranging from 1.2 to 12000 eV/nm. Irradiation effects of the low *LET* radiations, including gamma ray from Co-60 source, 1.5 keV Ultra Soft X-ray, 28 MeV electrons and UV photons with a wavelength of 222 nm were also investigated. PADC consists of the combination of a radio-sensitive section and a radio-tolerant one. The former contains ether and carbonate ester and the latter is “polyethylene-like” network formed during the polymerization. A single electron cleaves ether but it cannot break carbonate ester. At least two electrons should hit the radio-sensitive section to leave the permanent damage. To reach the detection threshold, at least two radio-sensitive sections should be destroyed in the radial direction of ion tracks. A new physical parameter, Radial Electron Fluence around Ion Tracks, *REFIT*, is proposed to describe the response of PADC, which is the number density of secondary electron passing through the cylinder with identical axis to the ion pass.

Résumé

Quarante années se sont écoulées depuis la découverte du poly (allyl diglycol carbonate), PADC, comme détecteur solide de traces nucléaires. En raison de sa haute sensibilité et de sa surface lisse même après gravure chimique, le PADC a été utilisé dans divers domaines scientifiques et technologiques comme la dosimétrie spatiale, la physique nucléaire, la dosimétrie neutronique, la détection du radon, le démantèlement d'installation nucléaires, l'accélération de particules avec des Lasers. Alors que le PADC est très sensible aux protons énergétiques et aux ions lourds, il est insensible aux rayonnements de faible transfert d'énergie tels que les rayons X et les électrons. Cette caractéristique unique permet l'identification des ions même dans des champs de rayonnement mixtes complexes, comme dans l'espace et les plasmas de Laser. Le seuil de détection du PADC pour un ion donné dépend du transfert linéique d'énergie. Le PADC se distingue d'autres détecteurs comme les émulsions nucléaires et les détecteurs fluorescents. De nos jours, les champs d'application des détecteurs solides de traces nucléaires s'étendent mais de nombreux points restent inconnus sur la structure des traces latentes et de leur mécanisme de formation.

Dans cette étude, la structure de la trace latente induite par des protons et des ions lourds dans le PADC a été examinée, pour des transferts d'énergie allant de 1,2 à 12000 eV/nm. Les effets d'irradiation des rayonnements de faibles transfert d'énergie, photons gamma, RX mous, électrons de 28 MeV et photons UV (222 nm) ont également été étudiés. Le PADC consiste en la combinaison d'une partie très radio-sensible et d'une autre plus résistante. La première contient des fonctions éther et ester de carbonate la seconde est constitué d'un réseau de type "polyéthylène". Dans ce travail de thèse une étude systématique des modifications chimiques du PADC permet de proposer un mécanisme pour le seuil de détection. Un nouveau paramètre physique, la Fluence électronique radiale autour du passage de l'ion, *REFIT*, est proposé pour décrire la réponse du PADC.

Contents

Chapter 1 Introduction 1
1.1. Etched Track Detector (ETD) 1
1.1.1. Detection principle of ETD 1
1.1.2. A short history of track detectors 3
1.2. Poly(ally diglycol carbonate), PADC 5
1.2.1. A short history and application of PADC 5
1.2.2. Some PADC based detectors 6
1.2.3. Analysis of the latent track structure in PADC 6
1.3. Proposed physical parameters 8
1.3.1. Stopping power 8
1.3.2. Z_{eff}/β 9
1.3.3. Primary Ionization (*PI*) 9
1.3.4. Restricted Energy Loss (*REL*) 9
1.3.5. Radial dose distribution theory 11
1.4. Purpose of this thesis 12
1.5. Structure of the thesis 15

Chapter 2 Experiments, Track overlapping model and Simulation code 17
2.1. PADC samples 17
2.2. FT-IR spectrometry 18
2.3. Combined use of Karl Fischer titration and FT-IR 20
2.4. Gamma ray irradiation 21
2.5. Ultra Soft X-ray (USX) irradiation 22
2.6. 28 MeV electron beam irradiation 23
2.7. UV irradiation 25
2.8. High energy protons and other ions irradiation 26
2.9. Track overlapping model 28
2.10. Monte Carlo simulation using Geant4-DNA toolkit 31

Chapter 3 Generation of OH groups after the irradiation 33
3.1. Molar absorption coefficient of OH groups in PADC 33
3.2. Quantitative estimation of OH groups in PADC after the irradiation 36
3.3. Summary for the quantitative analysis of OH groups 39

Chapter 4 Effects of low *LET* radiations and 222 nm UV photons 40
4.1. Gamma ray and Ultra Soft X ray exposures 40
4.1.1. Reduction of the relative absorbance 40
4.1.2. Radiation chemical yields for losses of typical functional groups 42
4.2. Effects of 28 MeV electron irradiation 44
4.2.1. Changes in the absorbance of ether, carbonate ester, CH groups and OH groups 44
4.2.2. Breaking of ether 45
4.2.3. Losses of carbonate ester and CH groups 47
4.2.4. Generation rate of OH groups 47
4.2.5. Radiation chemical yields for typical functional groups in PADC 48
4.3. Elucidation of the layered structure of latent track 49
4.4. Estimation of the defect size of 222 nm UV photons 50
4.4.1. Quantum yields for typical functional groups in PADC 50
4.4.2. Size estimation of the defect of 222 nm UV photons 52
4.5. Summary for the low *LET* radiations and 222 nm UV photon irradiations 54

Chapter 5 Radiation chemical yields for high energy protons below the detection threshold 57
5.1. Scissions of ether and carbonyl 57
5.2. Scissions of CH groups 61
5.3. Radiation chemical yields for losses of typical functional groups in PADC 63
5.4. Radial dose distributions around the detection threshold 65
5.5. Summary for the latent track structure of high energy protons 66

Chapter 6 Physical criterion for the detection threshold 69
6.1. Radial Electron Fluence around Ion Tracks for the detection threshold 69
6.1.1. Detection thresholds of PADC 69
6.1.2. Radial Electron Fluence around Ion Tracks at the detection thresholds 71
6.1.3. Future issues of the new physical concept 74
6.2. Estimation of the removal cross section for each track 76
6.2.1. Radial dose distributions around the ion tracks 76
6.2.2. Estimation of the removal cross sections for protons and heavy ions 77
6.3. Summary for the new physical criterion 79

Chapter 7 Conclusions 81

Acknowledgments 91

List of published papers 93

List of lectures 95

Awards 99

References 100

Figure Contents

1.1.1. A latent track and an etch pit. 1
1.1.2. Optical microscopic images of etch pits of C and Fe ions after the 4 h treatments: (a) the open mouth of etch pits, (b) the profile of etch pits. 2
1.1.3. The geometry of an ideal etch pit. 2
1.1.4. Photos of etch pits found in the helmet of Apollo program (Fleischer, 1998). 3
1.1.5. An example of (a) fluorescence image after the irradiation with C ion with an energy of 290 MeV/u and images of Nuclear Emulsion after the exposure to (b) a 1 MeV and (c) a 100 MeV electron track (Fukuda et al., 2010). 4
1.2.1. A repeat unit of PADC. 5
1.2.2. Track core radius in PADC evaluated from different methods as a function of the stopping power. 7
1.3.1. Track response data measured by AFM as a function of *REL* (ω_0=200 eV) together with the conventional data measured by optical microscope (Kodaira et al., 2013). 11
1.3.2. Radial dose distributions around ion tracks of He ions with energies of 0.5 MeV/u (solid line in red), 5.5 MeV/u (dotted line in green) and 50 MeV/u (broken line in blue). 12
1.4.1. G value for loss of carbonyl in PET against the stopping power (Yamauchi et al., 2012&2017). 13
2.1.1. A repeat unit of PADC. 17
2.2.1. An IR spectrum of pristine PADC measured under vacuum using FT/IR-6100S. 18
2.3.1. Karl Fischer Coulometric Titrator, EV-200 (a), and electronic balance, AG245 (b),. 20
2.3.2. IR spectra of pristine PADC film around OH groups. The spectrum in red is measured in ambient air, in green measured in air after the Karl Fischer measurement with 160℃ and in blue measured in vacuum. 21
2.4.1. Experimental set up for gamma exposures from Co-60. 22
2.5.1. Air Kerma rate measured by an ionizing chamber against the distance from the Al source (Groetz et al., 2014). 23
2.6.1. Simulated energy spectrum of the electrons by the Bremsstrahlug photons. 24
2.6.2. Absorbed doses of electrons per each event produced by Bremsstrahlug photons. 25
2.7.1. UV-Visible spectrum of the pristine PADC film with a thickness of 3.3 μm. The inset is the monochromatic photon emission spectrum with a photon energy of

5.59 eV. 26
2.8.1. Experimental conditions for the incident energy plotted on the graph of the stopping power against the normalized ion speed β. The experimental points in cyclotron are plotted as the square symbols, as well as those in MEXP as the circle symbols. 27
2.9.1. Track accumulation process with a radius of 3.5 nm (Yamauchi et al., 2000). The length of one side is set as 100 nm. 29
2.9.2. Fraction of area occupied by tracks with different folds. 30
2.9.3. Relation between track size and critical fluence. Plotted points are the results derived by track overlapping model (Yamauchi et al., 2000). 31
2.10.1. The track structure of single proton track with an energy of 5.7 MeV in liquid water. 32
3.1.1. Schematic views of the latent tracks formed in PADC. 34
3.1.2. Drying process of water absorbed in PADC with a thickness of 100 μm measured in ambient air (Kusumoto et al., 2015). 34
3.1.3. Evaporation behavior of water absorbed in PADC as a function of time. The mass of water is measured by electronic balance. 34
3.1.4. Proportional relation between the absorbance on IR spectra and mass of water absorbed in PADC (Kusumoto et al., 2015). The line is guide for eye. 35
3.1.5. Proportional relation between the absorbance per thickness and molar concentration of OH groups in PADC. 35
3.2.1. IR spectra of pristine PADC film with a thickness of 15 μm measured in ambient air (green) and under vacuum (red). 36
3.2.2. Increase of OH groups in PADC exposed to C, Ne and Ar ions with fluence. Inset shows the evolution of IR spectra of PADC around 3500 cm^{-1} measured under vacuum after the irradiation with Ne ion with an energy of 4.1 MeV/u (Kusumoto et al., 2015). 37
3.2.3. Reduction of the relative absorbance, A/A_0, of ether, carbonyl and C-O-C in PADC against the fluence of Ne ions. 38
3.2.4. Amount of OH groups per unit distance of track length as a function of the stopping power (Kusumoto et al., 2015). 38
3.2.5. Correlation between the generation density of OH groups and damage density of ether. The line is guide for eye (Mori et al., 2011; Kusumoto et al., 2015). 38
4.1.1. IR spectra of PADC films before and after exposures to gamma ray with absorbed doses of 60 kGy (a) and 120 kGy (b). 40
4.1.2. Reduction of the relative absorbance of ether, carbonyl, C-O-C and CH groups in

PADC exposed to gamma ray. Solid symbols indicate the present results and open symbols indicate previous ones (Mori et al., 2009). 41

4.1.3. Reduction of the relative absorbance of ether, carbonyl, C-O-C and CH groups in PADC irradiated with USX. 41

4.1.4. G values for loss of ether against the stopping power. The horizontal axis is applied to average *LET* in water as 0.2 eV/nm for gamma ray. The present results are plotted as solid symbols and the previous ones are indicated as open symbols (Mori et al., 2009&2011; Kusumoto et al., 2016a&b). 42

4.1.5. G values for loss of carbonyl against the stopping power for protons and heavy ions. The horizontal axis is applied to average *LET* in water as 0.2 eV/nm for gamma ray. The present results are plotted as solid symbols and the previous ones are indicated as open symbols (Mori et al., 2009&2011; Kusumoto et al., 2016a&b). 42

4.2.1. Reduction of the relative absorbance of ether, carbonyl, C-O-C and CH groups (left axis) and increase of the absorbance around OH groups (right axis) against the fluence (Kusumoto et al., 2016b). 44

4.2.2. Damage density for loss of ether against the stopping power (Kusumoto et al., 2016b). The deposited energy per unit distance is applied to 28 MeV electron. 46

4.2.3. Relation between track size and critical fluence. Plotted points are the results derived by track overlapping model (Yamauchi et al., 2000; Kusumoto et al., 2016b). 46

4.2.4. Two steps damage formation process in PADC. The ether is broken in Single-hit zone (a) and carbonate ester is lost with the OH groups in Multi-hits zone (b). 48

4.2.5. G values for loss of ether against the stopping power (2016b). The horizontal axis of 28 MeV electron and gamma ray are applied to deposited energy per unit distance and average *LET* in water, respectively. 48

4.2.6. G values for loss of carbonyl against the stopping power (Kusumoto et al., 2016b). The deposited energy per unit distance and average *LET* in water are adopted to 28 MeV electron and gamma ray, respectively. 49

4.2.7. G values for loss of CH groups against the stopping power (Kusumoto et al., 2016b). The deposited energy per unit distance and average *LET* in water are adopted to 28 MeV electron and gamma ray, respectively. 49

4.3.1. Layered structure of C ion track with an energy of 4.8 MeV/u. 50

4.4.1. Subtracted IR spectra of PADC exposed to UV photons (Sakamoto et al., 2000). 51

4.4.2. Changes in absorbance under the UV irradiations up to 5.4×10^{18} photons/cm^2 (Sakamoto et al., 2010). The absorbance is evaluated using the area under each

peak in subtracted spectra. 52
4.4.3. Changes in absorbance under the UV irradiations up to 2.3×10^{20} photons/cm^2 (Sakamoto et la., 2010). The absorbance is the height of each peak in subtracted spectra. 53
4.4.4. The relation between the critical fluence of the photon and the effective radius of the UV damage. Inset is an example of the accumulated UV defects in the volume of $2\times2\times10$ nm^3 at the critical condition. 54
5.1.1. IR spectra before and after the exposure to 70 MeV proton with a fluence of 7.1×10^{13} ions/cm^2. 58
5.1.2. Relative absorbance of ether, carbonyl and CH groups in PADC irradiated with 70 MeV proton against the fluence (Kusumoto et al., 2016a). The slope of each fitted line corresponds to the removal cross sections. 58
5.1.3. Damage density for loss of ether in PADC as a function of the stopping power. Solid symbols indicate the present results (Kusumoto et al., 2016a) and open symbols indicate previous ones (Mori et al., 2011&2012). 59
5.1.4. Damage density for loss of carbonyl in PADC as a function of the stopping power. Solid symbols indicate the present results (Kusumoto et al., 2016a) and open symbols indicate previous ones (Mori et al., 2011&2012). 60
5.1.5. Effective track core radius for loss of ether in PADC as a function of the stopping power. Solid symbols indicate the present results (Kusumoto et al., 2016a) and open symbols indicate previous ones (Mori et al., 2011&2012). 61
5.1.6. Effective track core radius for loss of carbonyl in PADC as a function of the stopping power. Solid symbols indicate the present results (Kusumoto et al., 2016a) and open symbols indicate previous ones (Mori et al., 2011&2012). 61
5.2.1. Damage density for loss of CH groups in PADC as a function of the stopping power. Solid symbols indicate the present results (Kusumoto et al., 2016a) and open symbols indicate previous ones (Kusumoto et al., 2015). 62
5.2.2. Effective track core radius for loss of CH groups in PADC as a function of the stopping power. Solid symbols indicate the present results (Kusumoto et al., 2016a) and open symbols indicate previous ones (Kusumoto et al., 2015). 63
5.3.1. G value for loss of ether in PADC against the stopping power. Solid symbols indicate the present results of high energy protons (Kusumoto et al., 2016a) and open symbols indicate previous ones of low energy proton and heavy ions (Mori et al., 2011&2012) and of gamma ray in chapter 4 (Kusumoto et al., 2017a). 64
5.3.2. G value for loss of carbonyl in PADC against the stopping power. Solid symbols indicate the present results of high energy protons (Kusumoto et al., 2016a) and

open symbols indicate the previous ones of low energy proton and heavy ions (Mori et al., 2011&2012) and of gamma ray in chapter 4 (Kusumoto et al., 2017a). 64

5.3.3. G value for loss of CH groups in PADC against the stopping power. Solid symbols indicate the present results (Kusumoto et al., 2016a) and open symbols indicate the previous ones (Kusumoto et al., 2015). 65

5.4.1. Radial dose distribution around the proton tracks in PADC with energies of 2.7, 5.7, 20, 30 and 70 MeV. The plots show the experimentally obtained effective track core radius for ether. 66

5.5.1. Effective track core radius for losses of ether, carbonyl and CH groups in PADC against the stopping power (Kusumoto et al., 2016a). There are three regions for the modified track structure in PADC irradiated with protons and heavy ions. 67

6.1.1. Track response data as a function of the stopping power. 70

6.1.2. A single C ion track with an energy of 46 MeV/u in the virtual stopping media: the blue arrow is the C ion track, the red lines are secondary electrons and yellows are interaction points. 71

6.1.3. Schematic views of electrons crossing borders without back scattering (a) and with back scattering (b). The purple points are interaction points and the red arrows are trajectory of secondary electrons. 71

6.1.4. Radial Electron Fluence around Ion Tracks, *REFIT*, at the detection thresholds for each ion. 72

6.1.5. Local dose distributions calculated using Geant4-DNA for proton, He and C ions at each detection threshold. 73

6.1.6. Track response data as a function of the *REFIT* at a radius of 1 nm. 74

6.1.7. Impact parameter, *b*, against the energy of ions. The plotted points are impact parameters at the detection thresholds for each ion. 75

6.2.1. Radial dose distributions around the paths of proton, He, C and Fe ions calculated by Geant4-DNA (solid lines) and radial distribution model (broken lines). 76

6.2.2. Probability of carbonate ester breaking at radial distance from ion's path. The simulations are made using Eq. 6.2.1 for a D_0 value of 5 MGy. 77

6.2.3. Removal cross sections for each track of proton, He, C and Fe ions. The present results, experimental results (Mori et al., 2011&Kusumoto et al., 2016a) and previous results (Barillon et al., 2013) are plotted as solid circles, open triangles and open diamonds, respectively. 78

Table Contents

2.2.1. IR absorption peak assignment for PADC. 19
2.8.1. Irradiation conditions in NIRS. 28
4.2.1. List of the removal cross sections for typical functional groups in PADC exposed to 28 MeV electrons (Kusumoto et al., 2016b). 46
4.4.1. Quantum yields for typical functional groups in PADC 52
5.1.1. Removal cross sections of ether, carbonyl and CH groups for high energy protons. 58
6.1.1 The detection thresholds of PADC for each ion 70
6.1.2. List of the *REFIT* at the detection threshold. 74
6.2.1. Comparison of the removal cross section for carbonyl in PADC simulated by Geant4-DNA to previous ones and experimental ones. 79

Chapter 1
Introduction

1.1. Etched Track Detector (ETD)

The detection principle and a short history of track detectors are described in this section. The author shows advantages of the Etched Track Detector, ETD, compared to other track detectors, such as Fluorescent Nuclear Track Detector and Nuclear Emulsion.

1.1.1. Detection principle of ETD

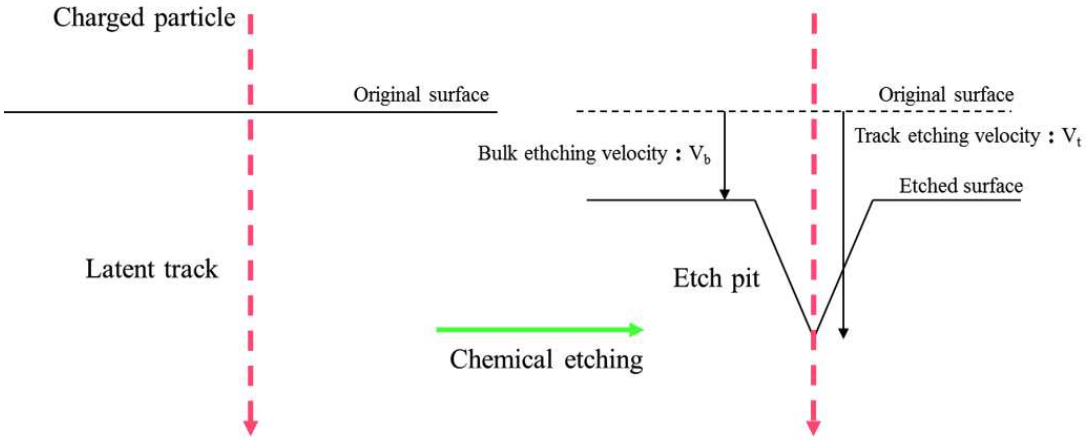

Fig. 1.1.1. A latent track and an etch pit.

ETD is a passive nuclear track detector, which makes it possible to observe each ion path as an enlarged etch pit after chemical etching. The main advantages of ETDs are their small size, light weight and no power supply required. In addition, ETDs record only protons and heavy ions. This implies that the author can avoid the influences from X-rays and gamma rays in the mixed radiation field. Figure 1.1.1. shows the detection principle of the ETDs. When charged particles passed through the ETDs, permanent damages, named latent track, are created. The latent track is preferentially etched by the chemical etching compared to un-irradiated region (Somogyi et al., 1976). The enhanced latent tracks are called etch pits, of which size, shape and length depend not only on deposited energies but also on ion species. Optical microscopic images of etch pits of C and Fe ions on Poly(allyl diglycol carbonate), PADC, after the 4 h etching treatments are shown in Fig. 1.1.2. (a-1) and (a-2) indicate the top views and (b-1) and (b-2) show top views. The open mouth of the etch pits of Fe ions are larger than those of C ions. As shown in Fig. 1.1.1., the V_t is the longitudinal etching velocity along the latent track and V_b is isotropic etching velocity of undamaged region (Somogyi&Szalay, 1973). The etch rate ratio, V, is simply defined as the ratio of the track etching velocity, V_t, to the bulk etching velocity,

V_b, as,

$$V \equiv \frac{V_t}{V_b}. \tag{1.1.1}$$

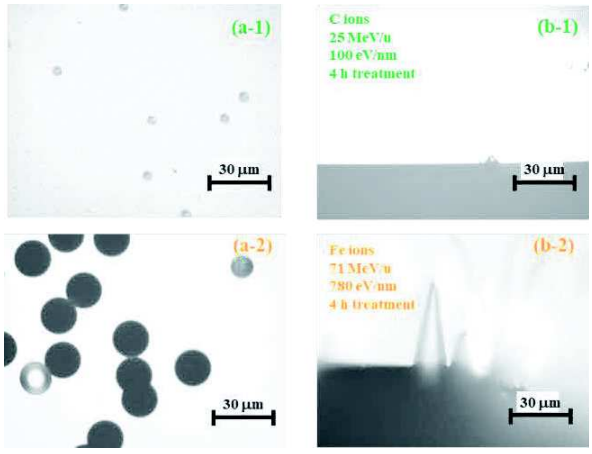

Fig. 1.1.2. Optical microscopic images of etch pits of C and Fe ions after the 4 h treatments: (a) the open mouth of the etch pits, (b) the profile of etch pit.

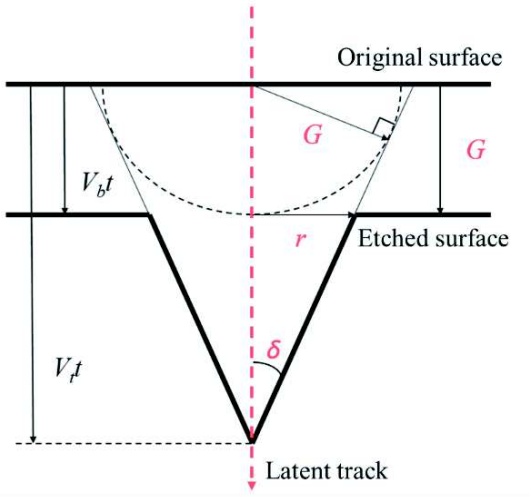

Fig. 1.1.3. The geometry of an ideal etch pit.

As far as the etch pit profiles are conical in shape, as shown in Figs 1.1.2 (b-1) and (b-2), one can assume that V_t is constant along the latent tracks. In such cases, the following equations can be applied to evaluate the etch rate ratio, V, as,

$$V = \frac{1+\left(\frac{r}{G}\right)^2}{1-\left(\frac{r}{G}\right)^2}, \tag{1.1.2}$$

where r is the etch pit radius and G thickness of layer removed, which are easily obtained by microscopic observation as shown in Fig. 1.1.3. The etch rate ratio is also able to be determined using the cone angle, δ, as,

$$V = \frac{1}{\sin\delta}. \tag{1.1.3}$$

This determination is effective even if the V_t varies along the ion tracks. The track registration sensitivity, S, for charged particles is then evaluated using reduced etch rate ratio as,

$$S = V - 1. \tag{1.1.4}$$

Many response studies have been performed to construct the calibration curve, in which the sensitivity is expressed as a function of the stopping parameters of each ion (Kodaira

et al., 2013; Hassan et al., 2013). Using the calibration curve, one can identify the ion species with a certain energy, in principle.

1.1.2. A short history of track detectors

The history of ETDs, started in 1958. The etch pits of fission fragments from the U_3O_8 film were found on the lithium fluoride after the chemical etching using the mixture of concentrated hydrofluoric acid and glacial acetic acid saturated lithium (Young, 1958). The dislocations in the LiF crystal were also observed as etch pits after the identical chemical etching. The origin of the ETDs is the research of lattice defect from the view point of the methodology. In 1959, the cleavages from surface layers of mica exposed to the fission fragments were observed using Transmission Electron Microscope (Silk&Barnes, 1959). Furthermore, Price and Walker indicated that the chemical etching was proceeded along the particle paths in mica (Price&Walker, 1962). Taking this as an opportunity, the chemical etching for observing the latent tracks as etch pits was extended to the various materials such as glasses and plastics. By expanding the latent tracks up to several μm, etch pits could be observed using optical microscope in wide area. Specially, poly ethylene terephthalate, PET, and poly bisphenol A carbonate, PC, which are synthetic products have been utilized as ETDs. The PET has been adapted to investigate the ultra-heavy components in galactic cosmic rays, including U ions (Drach et al., 1987). Figure 1.1.4. shows etch pit replicas on the helmet of astronaut on the Apollo program (Fleischer, 1998). Etch pits of C or Zn ions were observed on the PC based helmets.

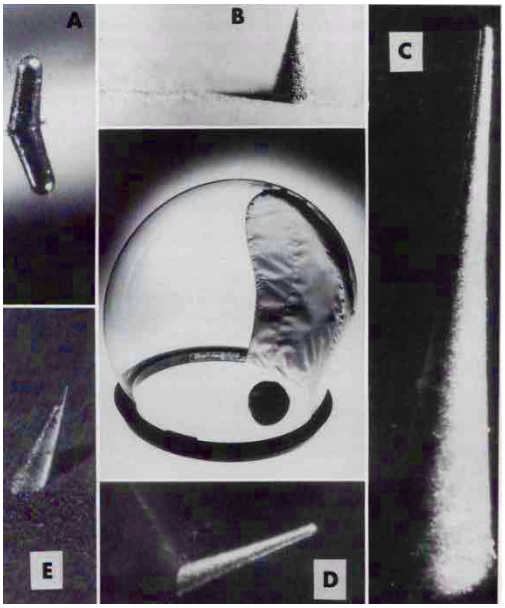

Fig. 1.1.4. Photos of etch pits found in the PC based helmet on Apollo program (Fleischer, 1998).

In recent years, a novel Al_2O_3 Fluorescent Nuclear Track Detector, FNTD, which is based on single crystals of anion-deficient aluminum oxide doped with carbon and magnesium has demonstrated high performance in the fields of radiation measurements (Akselrod et al., 2006). The FNTD have aggregate oxygen vacancy defects denoted as F_2^{2+}(2Mg)-centers characterized by a 620 nm absorption band and a 750 nm fluorescence emission with a 75 ns lifetime. The advantages of the FNTD are that (1) no chemical treatment required after the ion irradiations, (2) thermal stabilization (~600℃), (3) capability of multiple readout and (4) no fading effect. Furthermore, the FNTD can record the protons with energy higher than 100 MeV. This excellent track registration sensitivity enables us to observe tracks of secondary electrons. Figure 1.1.5 (a). shows C ion tracks with an energy of 290 MeV/u on the FNTD. High energy secondary electron tracks are clearly observed along the C ion path as indicated by yellow arrows in Fig. 1.1.5. The luminescence corresponds to the ion path as with ETDs. The geometric locations of ion traversals can be identified on the FNTD crystal. This technique is applied for investigating damages due to ion irradiations in mammalian cells (Kodaira et al., 2015).

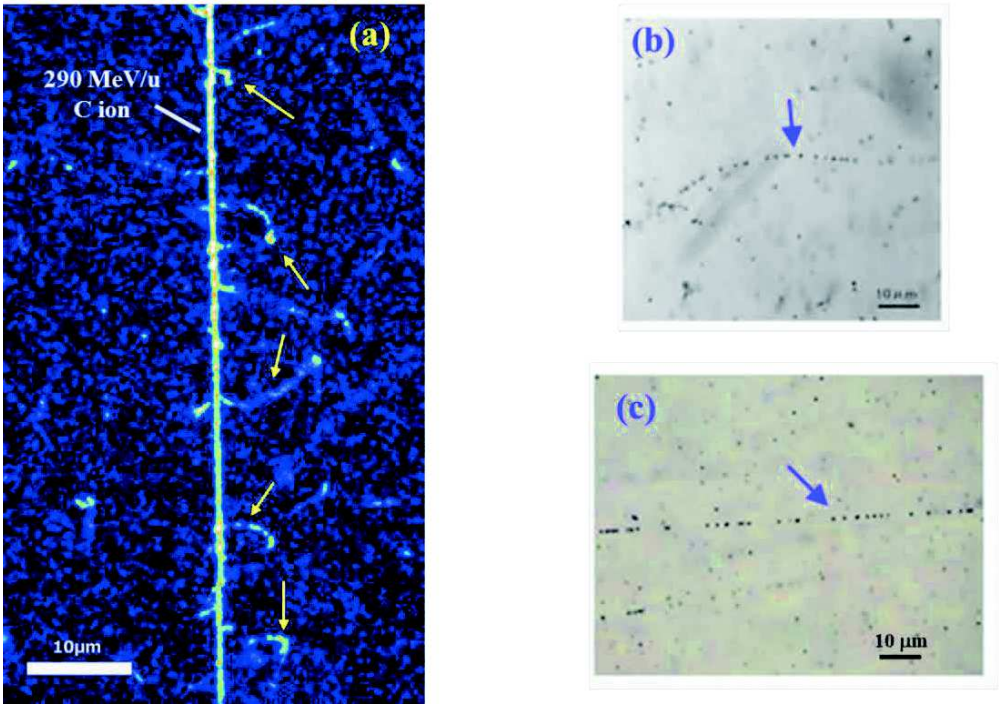

Fig. 1.1.5. An example of (a) fluorescence image after the irradiation with C ion with an energy of 290 MeV/u and images of Nuclear Emulsion after the exposure to (b) a 1 MeV electron and (c) a 100 MeV electron track (Fukuda et al., 2010).

The Nuclear Emulsion to which photographic technique is applied has been re-focused as well. Figure 1.1.5 (b) and (c) show, respectively, an electron track with energies of 1 MeV and 100 MeV, respectively, in Nuclear Emulsion under the microscopic observation (Fukuda et al., 2010). One of the advantages of the Nuclear

Emulsion is that it can record the trajectory of low Linear Energy Transfer, *LET*, radiations, such as high energy electrons. The Nuclear Emulsion can also record the track of muon contained in cosmic ray. Nowadays, the Nuclear Emulsion has been utilized in order to investigate a big void in Khufu's Pyramid in Egypt and the status of the melted nuclear cores in Fukushima Daiichi nuclear power plant (Morishima, 2016; Morishima et al., 2017). Different from the FNTD and the Nuclear Emulsion, PADC has no response to electrons. From another point of view, the relatively high threshold of PADC has the advantage of recording only ions under high flux of electrons.

1.2. Poly(allyl diglycol carbonate), PADC

In this section, a short history and characteristics of PADC are given. In addition, previously obtained results are indicated.

1.2.1 A short history and application of PADC

PADC was developed as an optical material by Columbia Chemical division in 1940s. PADC has radio-sensitive sections of an ether in the center and two carbonate esters in the symmetrical positions (Figure 1.2.1.). These sections are combined each other by "polyethylene-like" network. The PADC is the most sensitive ETD, which is known under the trade name of CR-39. The excellent track registration property of PADC, which has the high charge resolution, the clear open mouth and the smooth sample surface after the chemical etching was shown just 40 years ago (Cartwright et al., 1978). The PADC has been utilized in various fields such as neutron dosimetry (Oda et al., 2005), space radiation dosimetry (Doke et al., 1997; Benton et al., 2002), radon detections (Font, 2009), inertial nuclear fusion experiments (Zylstra et al., 2012) and intense laser driven ion acceleration experiments (Fukuda et al., 2009; Nishiuchi et al., 2015; Kanasaki et al., 2016). In laser driven ion acceleration experiments, not only PADC but also other ETDs, including PC, PET, and polyimide, PI, are used. This makes it possible to identify the

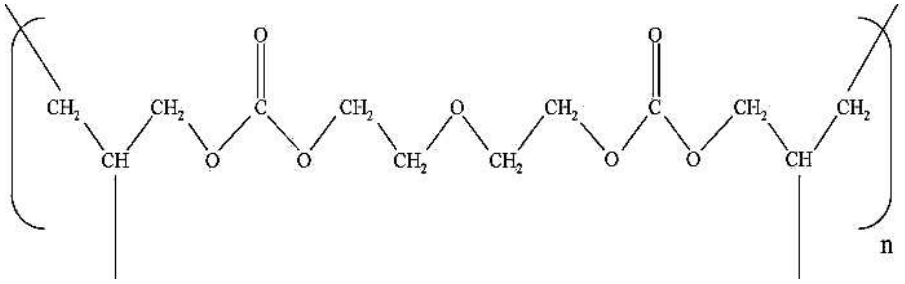

Fig. 1.2.1. A repeat unit of PADC.

heavy ion components utilizing the difference in sensitivities and thresholds of each ETD. While the application fields are spreading out, there are still unsolved aspects concerning the latent track structure and creation mechanism of it in ETDs.

1.2.2. Some PADC based detectors

Two kinds of PADC based detectors were developed by Prof. Ogura and Fukuvi Chemical Co., Ltd. (Japan) to improve the track registration sensitivity and the detection threshold, based on the purified monomer, named BARYOTRAK, (Ogura et al., 1997&2001). HARZLAS TD-1 which contains a small quantity of antioxidant can record the proton tracks up to 20 MeV, which is higher than BARYOTRAK (Hassan et al., 2013). HARZLAS TNF-1, which is co-polymerized with *N*-isopropulacrylamide, NIPPAm, archived the highest sensitivity in PADC, that it can register proton tracks up to 27 MeV.

Several attempts were also made to improve the track registration sensitivity and the detection threshold from the view of molecular arrangement. The SR-86 and SR-90 were developed as new ETDs with higher sensitivity by Prof. Fujii. SR-86 has sulfonate groups in place of carbonate esters of PADC (Fujii et al., 1988). The average length of carbonate linkages of SR-90 is 1.6 times longer than PADC (Fujii et al., 1993). The series of “SR” indicated the high track registration sensitivity compared to the original PADC. However, the detection threshold hardly changed. Unfortunately, the fundamental reason for high performance of PADC has not been understood yet. Systematic and comprehensive studies on the chemical damage structure in PADC after the ion irradiation is mandatory in order to clarify the reason of its high track registration property. Without such fundamental knowledge, the author can not develop new ETDs with desired sensitivity.

1.2.3. Analysis of the latent track structure in PADC

In 2011, the extensive breadth of studies on the track core radius in PADC was summarized by Mori et al., (Figure 1.2.2). A lot of studies have been performed using the conductometric method (Oganesyan et al., 2005), Small Angle Neutron Scattering, SANS, (Lounis-Mokurani et al., 2003), Electron Spin Resonance, ESR, (Böhlke&Hermsdorf, 2008), atomic force microscope, AFM, (Yamauchi et al., 2003a&2005a; Mori et al., 2011), UV-Visible spectrometry (Yamauchi, 2003; Yamauchi et al., 2003a&2005a) and Fourier Transform Infrared, FT-IR, spectrometry (Mori et al., 2011). Based on the conductivity changes in electrodes by chemical etching, the track core diameter for 7

MeV proton was estimated as 0.5 nm plotted as the solid square (1). The track core radius for 22.5 MeV proton was determined by SANS as 0.7 nm as shown in solid circle (2). The core size of proton with an energy of 3.4 MeV was obtained using the spatial

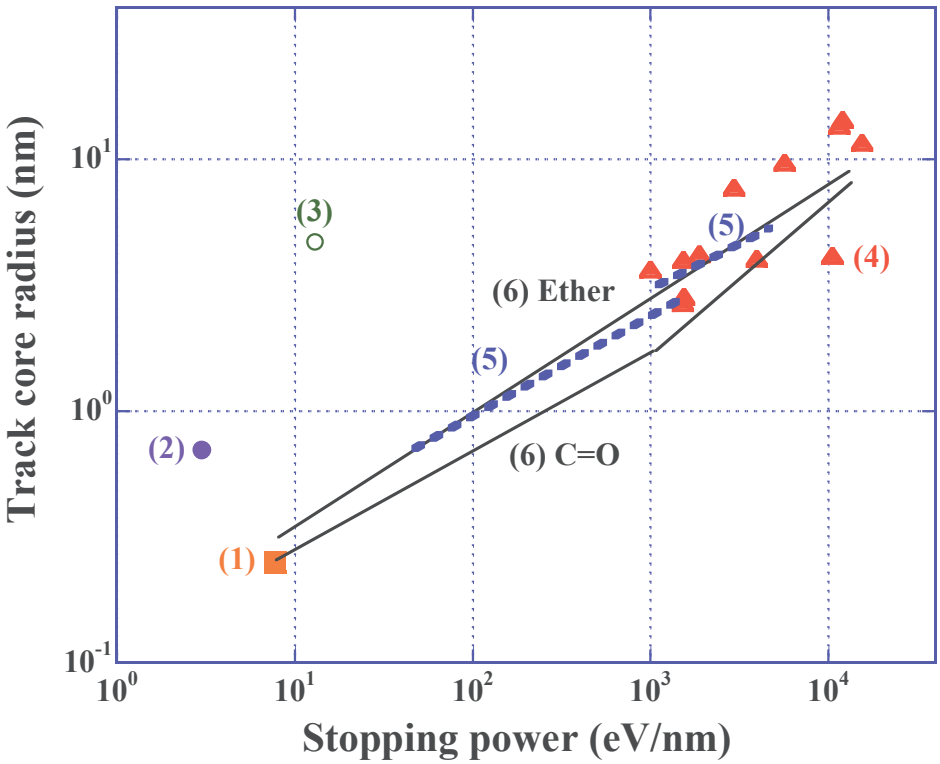

Fig. 1.2.2. Track core radius in PADC evaluated from different method as a function of the stopping power.
(1): Conductmetric method, solid square (Oganesyan et al., 2005).
(2): Small angle neutron scattering, solid circle (Lounis-Mokrani et al., 2003).
(3): Electron spin resonance, open circle (Böhlke&Hermsdorf, 2008).
(4): AFM, solid triangles (Yamauchi et al., 2003a&2005a; Mori et al., 2009).
(5): UV-Visible, broken line (Yamauchi, 2003; Yamauchi et al., 2003a&2005a).
(6): FT-IR, solid lines (Mori et al., 2009).

distributions of free radicals measured by ESR indicated as the open circle (3). At the higher stopping power region, AFM can be adapted to examine the track core radius in PADC. The results are plotted as the solid triangles (4). In the cases of lighter ions, etch pits were hardly observed because of the original surface roughness of PADC. The etch pits growth curves, which are the etch pit radius against the thickness of layer removed, after the short time etching below 1 min did not pass through the original points. In this case, the track core can be attained as the intersections by extrapolating the fitted growth curves against the thickness of layer removed to zero, where the etching rate of tracks in the radial direction was significantly enhanced. The critical fluence where track overlapping becomes statistically significant was obtained based on the track overlapping model and fluence dependence of the UV-Visible spectra. The critical fluence was

converted to the track core radius as shown in dotted lines (5). In this method, the track core is defined as the region where optical property is modified. FT-IR spectrometric studies have been carried out focusing on ether and carbonate ester composing the PADC. The core radius estimated by the conductmetric method was concordant with the trend of that for losses of ether and carbonyl estimated by IR method as shown in the solid lines (6). The core radius evaluated by SANS and ESR was greater than the trends of the other methods. The core size obtained by AFM method was also slightly greater than UV-Visible and FT-IR method. However, the core radius for ether by FT-IR method was in great agreement with that assessed by UV-Visible method within experimental error. These studies focused on the radio-sensitive sections. In 2015, the damage registration property of CH groups which is the radio-tolerant section in PADC was also examined using FT-IR spectrometry (Kusumoto et al., 2015). Examined region in the stopping power is also extended down to 1.2 eV/nm. The details are shown in the body of this thesis in chapter 5.

1.3 Proposed physical parameters

In 1960s studies, several physical parameters were proposed in order to universally express the track registration properties in PADC.

1.3.1. Stopping power

The stopping power, *-dE/dx*, (in eV/nm) is the linear rate of energy loss of a heavy charged particle in a medium, which is the most fundamental but the most important parameter in radiation physics, radiation chemistry and radiation biology. Using relativistic quantum mechanics, the Bethe-Bloch formula was attained to obtain the stopping power of a uniform medium for a heavy charged particle as,

$$\left(-dE/dx\right)=\frac{4\pi Z_1^2 e^4 N Z_2}{mv^2}\left\{ln\frac{2mv^2}{I}-ln(1-\beta^2)-\beta^2-\frac{C}{Z_2}+L_1Z_1+\phi-\frac{\delta}{2}\right\}. \quad (1.3.1)$$

Z_1 : Effective charge of incident particles
v : Velocity of incident particles
Z_2 : Atomic number of the medium
N : Number density of electrons in the medium
I : Mean excitation energy of the medium
β : Velocity of the particle relative to light speed
C/Z_2: Correction term of inner shell
L_1Z_1: Correction term of Z_1^3
Φ : Correction term of Bloch
$\delta/2$: Correction term of density effect
m : Mass of electron

Unfortunately, the stopping power failed to express the sensitivity and the detection threshold of PADC (Hassan et al., 2013). The sensitivities of He and C ions are apparently different from each other at the same stopping power. This means that the stopping power is not a universal parameter to describe the response of PADC. The stopping power is, however, one of the most important parameter to describe the stopping behaviors of each ion in matters. In this study, the stopping power calculated by SRIM code is used to present the experimental data as the stopping parameter in the horizontal axis (Ziegler, 2004).

1.3.2. Z_{eff}/β

The Z_{eff}/β is the ratio of the effective charge of heavy ions to the velocity of the ion speed normalized to the light speed in vacuum. It has been used to express the sensitivities of PET (Drach et al., 1987) and PI (Yamauchi et al., 2013). However, the derivation process of the effective charge has been ambiguous (Barkas&Berger, 1963; Schiwietz&Grande, 2001). The Z_{eff}/β can be seen as an improved parameter compared to the stopping power, but not sufficient to discuss the latent track formation process (Yamauchi et al., 2013).

1.3.3. Primary Ionization (PI)

The Primary Ionization rate, *PI*, is considered as the number of ions formed from the projectile interaction with matters per unit distance (Fleischer et al., 1967). In accordance with the *PI*, the contribution of secondary electrons is negligible for the creation of permanent damages. There has been mainly two criticism concerning the *PI*. The first one is that the ionizations produced by even the low energy secondary electrons are ignored. The other one is that the experimentally obtained ionization potentials were not realistic (Durrani&Bull, 1987). Indeed, *PI* failed to describe the response of PADC.

1.3.4. Restricted Energy Loss (REL)

The restricted energy loss, *REL*, in which high energy components of secondary electrons were assumed to not contribute to the track formation, can be calculated from the following expressions, (Benton&Nix, 1969).

$$(REL)_{\omega<\omega_0} = \{2\pi n(z_{eff})^2 r_0^2 m_0 c^2 / \beta^2\}\left[\ln(2m_0 c^2 \beta^2 \gamma^2 \omega_0 / I_{adj}^2) - \beta^2 - 2(C/Z) - \delta\right],$$

(1.3.2)

and

$$(REL)_{\omega>\omega_0} = \{2\pi n(z_{eff})^2 r_0^2 m_0 c^2 / \beta^2\}\left[\ln(\omega_{max}/\omega_0) - \beta^2\right], \quad (1.3.3)$$

where

$$\omega_{max} = \{2\beta^2/(1-\beta^2)\} m_0 c^2 \quad (1.3.4)$$

m_0c^2 : 0.511 MeV, the rest energy of electron
n : Density of electrons in the stopping material
r_0 : Classical electron radius
γ : $(1-\beta^2)^{1/2}$
I_{adj} : Mean excitation energy of the medium
C/Z : Tight binding shell correction
δ : Correction term of density effect
ω : Energy of secondary electrons
ω_0 : Cut off energy of secondary electrons

A certain cut-off energy, ω_0, has been adapted as the fitting parameter to reproduce the experimental results of each ETD. Figure 1.3.1 shows the track response data against the *REL* (Kodaira et al., 2013). The 200 eV was developed as the cut-off energy to express the sensitivity of PADC irradiated with protons and heavy ions. The sensitivity is expressed uniformly as a function of the *REL*. However, some problems of *REL* have been indicated, as well as Z_{eff}/β and *PI* (Durrani&Bull, 1987). One of the problem is the arbitrariness of ω_0 in the calculation. Namely, the physical basis of ω_0 is not well understood. This implied that the ω_0 of 200 eV cannot be applied to other ETDs of PC, PET and PI (Yamauchi et al., 2013). In addition, the secondary electrons with energies higher than 200 eV deposit their energies at a distant position from the ion path. Judging from these views, *REL* is not a universal parameter for the sensitivity and the detection threshold of ETD.

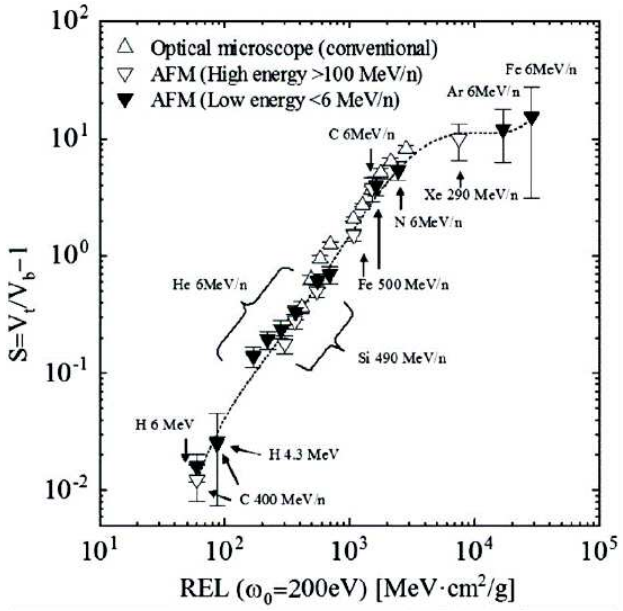

Fig. 1.3.1. Track response data measured by AFM as a function of *REL* (ω_0=200 eV) together with the conventional data measured by optical microscope (Kodaira et al., 2013).

1.3.5. Radial dose distribution theory

The radial dose distribution theory has been developed to express the response of Nuclear Emulsion (Waligórski et al., 1986). The advantage of the radial dose distribution theory is that the author can estimate the damage distribution at a certain position in the radial direction. Figure 1.3.2 shows radial dose distributions for He ions with energies of 0.5, 5.0 and 50 MeV/u. The dose decreases with the increasing incident energy. The most energetic secondary electron produced by ion deposit its energy at a distant position from the particle trajectory. In previous studies, it was considered that the track core was formed where radial dose was higher than 1 MGy (Yamauchi et al., 2008a). In addition, a criterion which states that etch pits are formed when the local dose is more than 100 kGy at 1 nm from the track center was proposed (arrows in Fig. 1.3.2). This has a certain agreement with experimental results, which the detection thresholds of PADC for He ions is 5.5 MeV/u as shown in arrows in Fig 1.3.2. The radial dose distribution model was considered as the suitable parameter for expressing the track registration property. However, the bulk etching velocity depends not only on the absorbed dose but also on the dose rate (Yamauchi et al., 1999). Furthermore, the molecular network of PADC is never uniform in such a small volume. It suggests that one can not simply apply this theory to express the sensitivity of ETDs.

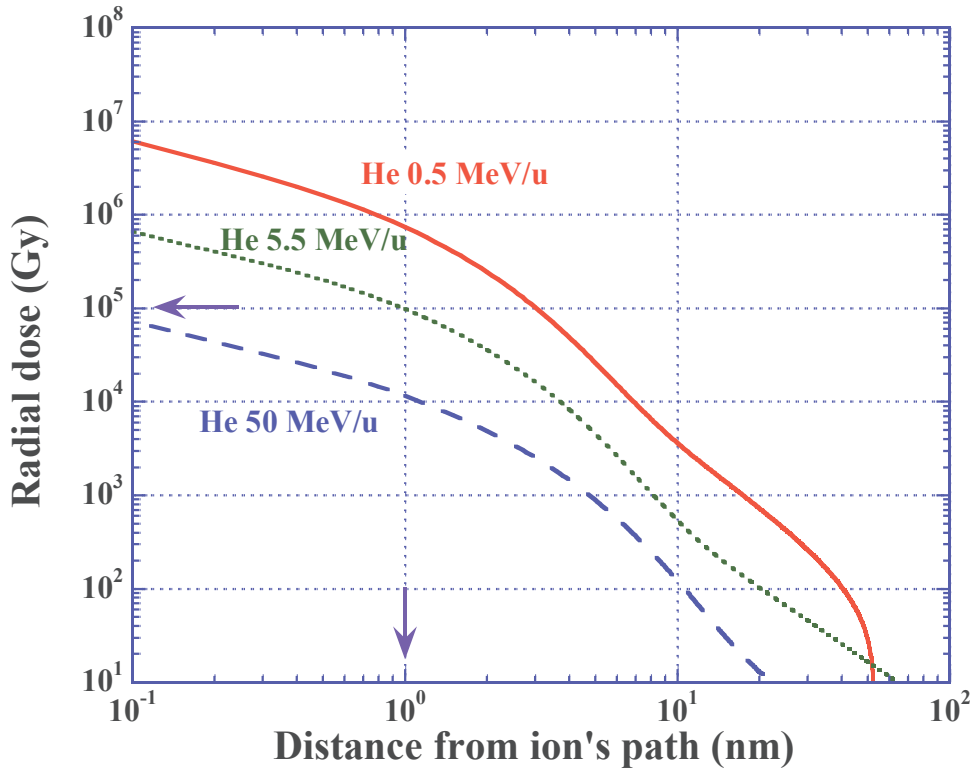

Fig. 1.3.2. Radial dose distributions around ion tracks of He ions with energies of 0.5 MeV/u (solid line in red), 5.5 MeV/u (dotted line in green) and 50 MeV/u (broken line in blue).

1.4. Purpose of this thesis

In this decade, FT-IR spectrometric studies have been performed to clarify the latent track structure in PADC. However, some unsolved issues of structure and formation mechanism of latent tracks are still remained as followings:

(i) The first issue is generation amount of OH groups after the irradiation. OH groups, which are hydrophilic groups, have been considered to dominate the longitudinal etching velocity along the latent track. The author has to evaluate the amount of OH groups quantitatively which formed along the tracks to elucidate the modified structure of PADC. In this thesis, molar absorption coefficient of OH groups of water absorbed in PADC is determined to assess the newly generated OH groups in PADC exposed to proton and heavy ions.

(ii) The second issue is to try to correlate the formation of latent tracks with the number of secondary electrons produced by the incoming ion. The latent tracks in PADC have at least three regions, named layered structure, (Mori et al., 2011). All functional sections of ether, carbonate ester and CH groups are lost around the track center. Only the ether is broken at distance positions from the track center. Between these, the second region

where ether and carbonate ester are damaged is observed. In order to avoid the interactions between damages along the particle trajectory and to give an interpretation of the layered structure, the effects of low *LET* radiations, including gamma ray, 1.5 keV X-ray and 28 MeV electron are examined. In addition, the previous results related to 222 nm UV photons reported by Sakamoto et al, are reproduced (Sakamoto et al., 2010). The track overlapping model is extended to estimate the size of the point-like defects after the UV exposures.

(iii) The third issue is to clarify the difference in damage structure between etchable tracks and unetchable ones. The chemical modification along proton and heavy ion tracks not only in PADC (Mori et al., 2009&2011) but also in PET and PC (Yamauchi et al., 2011&2012) has been investigated at the stopping powers ranging from 10 to 12,000 eV/nm. The radiation chemical yield, G value, for loss of carbonyl in PC was independent of the stopping power. Figure 1.4.1 indicates the G value for loss of carbonyl in PET

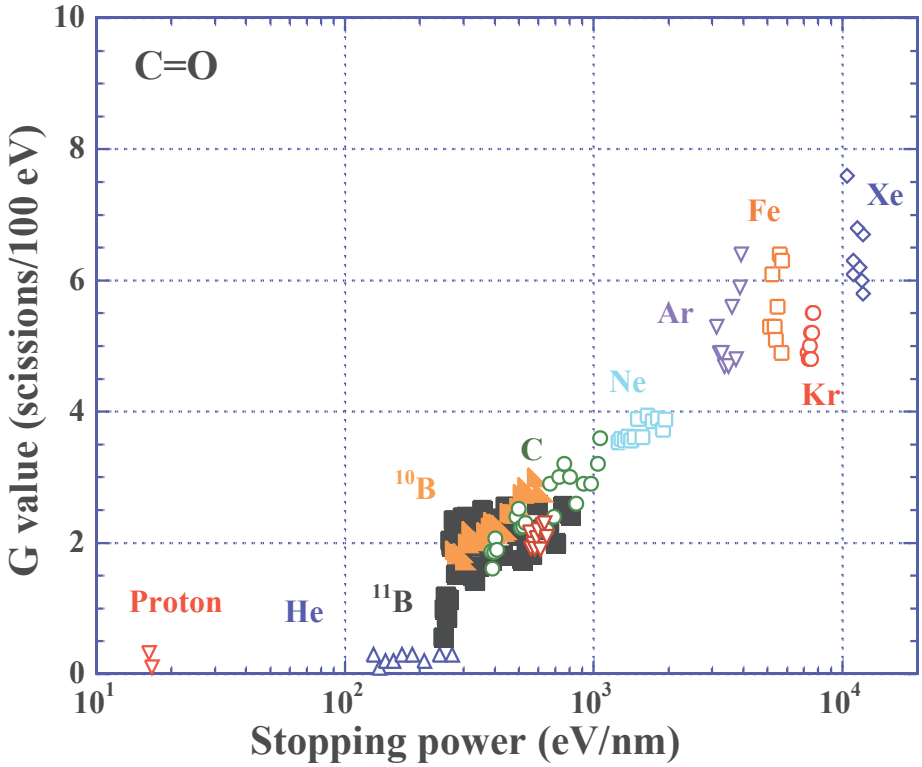

Fig. 1.4.1. G value for loss of carbonyl in PET against the stopping power (Yamauchi et al., 2012&2017).

against the stopping power. The distinct step-like change was observed at the stopping power of 250 eV/nm, between He and C ions, which is concordant with the detection threshold. The step was complemented by B^{11} ions (Yamauchi et al., 2017). The step shows structure change of latent tracks in PET around the detection threshold. In comparison to PC and PET, a lot of authors examined the latent track structure using

various methods (see Fig. 1.2.2.), but there were not enough data-sets to compare the chemical damage structure in PADC at the two ends of the detection threshold. In the present study, the examined stopping power is started from 1.2 eV/nm using high energy proton beams (20, 30 and 70 MeV) to investigate the latent track structure below the detection threshold.

(iv) The fourth issue is to propose a new universal parameter for the detection threshold of PADC. As mentioned earlier, a universal parameter that can express the detection threshold and the sensitivity of ETDs has not been reported yet. In this thesis, based on the experimental results, the author propose a new physical concept to universally express the detection threshold of PADC using Geant4-DNA.

The author tackles the above four issues to find the way to develop the new ETD which has higher track registration sensitivity than PADC from the view of the molecular arrangement. The present study is the first attempt to investigate the structure and the formation mechanism of latent tracks by combining FT-IR spectrometry and a Monte Carlo simulation.

Au cours de cette décennie, des études spectrométriques FTIR ont été réalisées pour clarifier la structure de la trace latente dans le PADC. Cependant, certaines questions sont encore non résolues :

- Le premier point concerne la quantité de groupes OH formé après irradiation. Les groupes OH, qui sont des groupes hydrophiles, jouent un rôle crucial dans la vitesse d'attaque lors de la révélation chimique d'une trace latente.

- Le second consiste à essayer de corréler la formation des traces latentes avec le nombre d'électrons secondaires produits par l'ion incident. On peut distinguer au moins trois régions dans la structure d'une trace latente, (Mori et al., 2011). Tous les groupes fonctionnels éther, ester de carbonate, et les liaisons CH sont perdus dans le cœur de la trace. Les liaisons éther sont principalement affectées à de large distance du cœur. Entre deux, on observe une région où les fonctions éther et ester de carbonate sont principalement endommagées. Afin de corréler cette structure en couches avec les électrons produits par l'ion incident, nous examinons dans ce travail de thèse les effets des rayonnements à faible *TLE* ; rayons gamma, rayons X de 1,5 keV et électrons de 28 MeV. Des irradiations aux photons UV de 222 nm rapportés par Sakamoto et al., sont également effectués (Sakamoto et al., 2010). Le modèle de chevauchement des traces est étendu pour estimer la taille des défauts ponctuels induits par une expositions aux UV.

- Le troisième point est de clarifier la différence au niveau de la structure d'une trace latente, entre une trace qui est révélable et une trace qui ne l'est pas. La modification chimique le long des traces de protons et d'ions lourds pour le PADC (Mori et al., 2009 & 2011) mais aussi pour le PET et le PC (Yamauchi et al., 2011 & 2012) a été étudiée pour des *TLE* compris entre 10 et 12 000 eV / nm . Le rendement radiolytique, valeur G, pour la perte des fonctions carbonyle dans le PC est indépendante du *TLE*. La figure 1.4.1 indique cette même valeur de G dans le PET. Un changement net est observé pour une valeur de 250 eV / nm, entre les ions He et C, concordant avec le seuil de détection. L'étude a été complétée avec des ions Bore (Yamauchi et al., 2017). Cette étude confirme le changement de structure des traces latentes dans le PET autour du seuil de détection. Il n'y a pas de données expérimentales autour du seuil de détection pour le PADC. Dans la présente étude, des faisceaux de protons de haute énergie (20, 30 et 70 MeV) permettent d'étudier la structure d'une trace latente latente en dessous du seuil de détection du PADC.

- Le quatrième point consiste à proposer un nouveau paramètre universel pour déterminer le seuil de détection dans le PADC. Dans cette thèse, l'auteur propose pour la première fois en partant des résultats expérimentaux obtenus avec la spectrométrie FTIR un nouveau concept physique pour exprimer ce seuil de détection à l'aide du code Geant4-DNA.

1.5 Structure of the thesis

Chapter 1 explains the history and the definition of the track registration sensitivity of ETDs. The issues of past studies are pointed out and the author mentions the purpose of the present study.

Chemical structure of the PADC is represented in chapter 2. The experimental sets up of the facilities, conventional track overlapping model and the Geant4-DNA Monte Carlo simulation code are also explained.

In chapter 3, the molar absorption coefficient of OH groups in PADC is determined. The author evaluates amount of OH groups decorating new ending groups in PADC exposed to proton and heavy ions.

Chapter 4 represents the irradiation effects of gamma ray, 1.5 keV X-ray and 28 MeV electrons. The track overlapping model is extended to estimate the size of defects of 222 nm UV photons.

The modified structures of latent tracks in PADC are investigated below the detection threshold in chapter 5.

In chapter 6, a new physical concept for the detection threshold of PADC is proposed using Geant4-DNA. The size of removal cross sections for protons and heavy ions is also estimated using the radial dose distribution theory.

This thesis is concluded in chapter 7.

Le premier chapitre présente l'historique et définie le seuil de détection. La structure chimique du PADC est représentée au chapitre 2. Les moyens d'irradiations, les techniques expérimentales ainsi que le modèle de chevauchement des traces et le code de simulation Monte-Carlo Geant4-DNA sont également présentés. Dans le chapitre 3, le coefficient d'absorption molaire des groupes OH dans le PADC est déterminé. L'auteur évalue la quantité de groupes OH formés dans le PADC après exposition aux protons et aux ions lourds. Le chapitre 4 représente les effets d'irradiation des rayons gamma, des rayons X de 1,5 keV et des électrons de 28 MeV. Le modèle de chevauchement des traces est étendu pour estimer la taille des défauts initiés par des photons UV de 222 nm. Les structures des traces latentes dans le PADC en dessous du seuil de détection sont présentées au chapitre 5. Au chapitre 6, un nouveau concept physique pour le seuil de détection du PADC est proposé en utilisant le code Geant4-DNA

Chapter 2
Experiments, Track overlapping model and Simulation code

In this chapter, experimental methods, track overlapping model and simulation code are explained. The author prepared thin PADC films to obtain unsaturated IR spectra by chemical etching. The experimental set up for the exposures to low *LET* radiations, 222 nm UV photons, proton and heavy ions are given. Furthermore, the conventional track overlapping model and simulation code are shown.

Dans ce chapitre, les méthodes expérimentales, le modèle de chevauchement de traces et le code de simulation sont présentés. L'auteur a préparé de minces films PADC pour obtenir des spectres IR insaturés.

2.1. PADC samples

As PADC samples, commercially obtained sheets of BARYOTRAK with a nominal thickness of 100 μm (Fukuvi Chemical Industry Co., Ltd., Japan) have been utilized throughout the present study. The sheets were made from purified monomer higher than 99.99%, which can keep their flat surface even after heavy chemical etchings. A repeat unit of PADC has an ether in the center and two carbonate esters in symmetric positions (Figure 2.1.1). These parts are easily lost after the ion and gamma ray

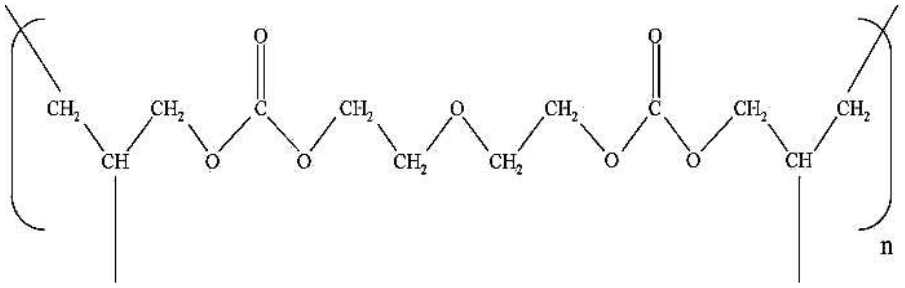

Fig. 2.1.1. A repeat unit of PADC.

irradiations (Mori et al., 2009&2011). This implies that ether and carbonate esters have been known as the radio-sensitive sections in PADC. The repeat units are combined to each other by “polyethylene-like” segments that are relatively radio-tolerant in the network. Excluding the two methines at the three-way junctions, most of CH belongs to the methylene groups. For the purpose of FT-IR measurements, two types of PADC samples were prepared by chemical etching in 6 M KOH solution kept at 70℃ (Yamauchi et al., 2008b). The first ones have thicknesses below 3 μm to evaluate the chemical damage parameters for losses of all functional groups including carbonate ester (carbonyl

and C-O-C) which has the strongest absorption of IR in PADC. The thickness of the other ones is 15 μm in order to analyze the amount of OH groups that is produced as new end-points after the irradiation.

PADC films with thicknesses of 15, 20, 30, 40 and 50 μm were prepared to determine the mass of water in PADC at room condition using the Karl Fischer method (See section 2.3). The sample with a thickness of 100 μm was also used to follow the drying process of water absorbed in PADC using both FT-IR spectrometer and electronic analytical scale.

2.2 FT-IR spectrometry

Infrared absorption spectrometry is one of the suitable methods to analyze polymer structure. Because each absorption band in the spectra is well assigned to each functional section composing the polymers, one can obtain qualitative and quantitative information from them.

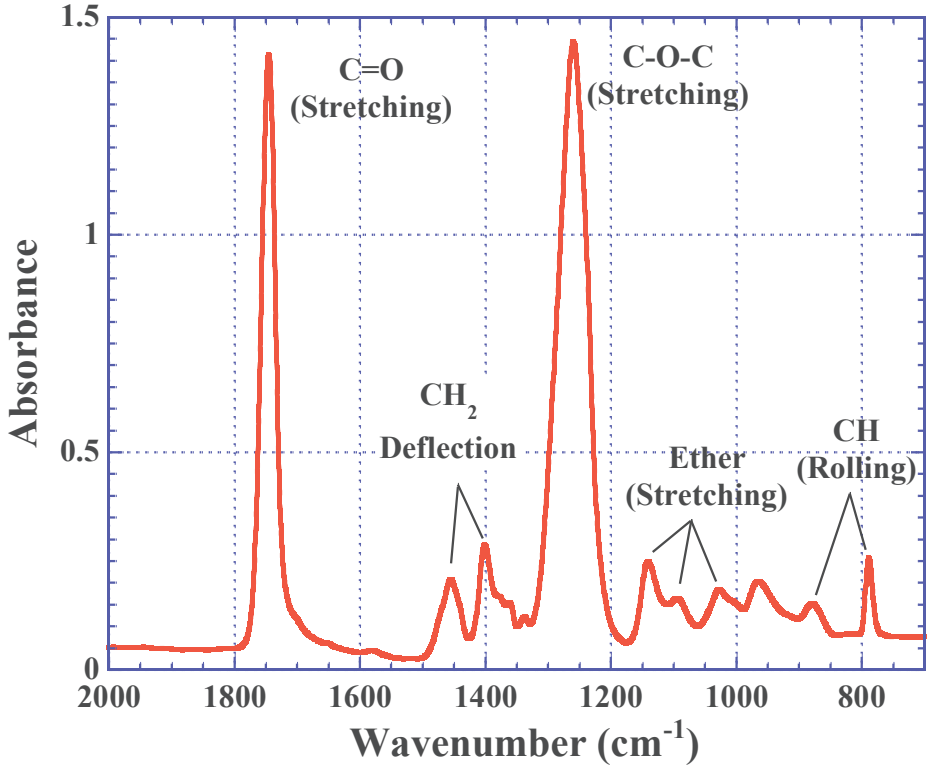

Fig. 2.2.1. An IR spectrum of pristine PADC measured under vacuum using FT/IR-6100S.

Several authors have reported the IR absorption peak assignment of PADC as listed in Table 2.2.1 (Darraud et al., 1994; Lounis-Mokrani et al., 2003). The three peaks at 1028, 1092 and 1142 cm^{-1} are assigned to the ether, which is the most radio-sensitive

Table 2.2.1 Absorption peak assignment for PADC.

		Wavelength (cm^{-1})		
Bonds	Vibration mode	Present study	Darraud et al.,	Lounis-Mokrani et al.,
CH	Rolling	789	791	784
CH	Rolling	878	878	871
Ether	Stretching	1028	1028	1022
Ether	Stretching	1092	1100	1080
Ether	Stretching	1142	1140	1133
C-O-C	Stretching	1250	1260	1226
CH_2	Deflection	1401	1400	1398
CH_2	Deflection	1456	1458	1452
C=O	Stretching	1750	1745	1734

section in PADC (Mori, 2014). Among them, the absorbance of stretching vibration peak at 1028 cm^{-1} has been utilized in order to estimate the chemical damage parameters for the ether because the peak is relatively isolated compared to the two others (Figure 2.2.1). The density of carbonate ester has been evaluated from the absorbance of peaks at 1250 cm^{-1}, which corresponds to the stretching vibration of C-O-C, and at 1750 cm^{-1}, which is assigned to stretching vibration of carbonyl, C=O (Mori et al., 2011). In the case of CH groups, the author has used the peak of rolling vibration of methine and methylene at 789 cm^{-1}, which is clearly isolated (Kusumoto et al., 2015). The absorbance of this peak indicates the amount of methine and methylene groups.

FT-IR spectrometric measurements were performed in vacuum with a spot of 1 cm in a diameter using FT/IR-6100S (JASCO, Japan). The entire system of FT/IR-6100S can be evacuated, including the photon-detector, interferometer and sample room, during the measurements. This made it possible to evaluate the amount of OH groups formed in PADC after the irradiation excluding the influence of water and CO_2 in ambient air.

Microscopic FT-IR measurements were also carried out in ambient air with a spot area of 50×50 μm^2 using IRT-5000 (JASCO, Japan) in order to investigate the damage density produced by pencil beam with a diameter of several mm.

The Beer-Lambert law helps us to determine the density of the considered functional groups from the measured absorbance. The law expresses the absorbance as the product of molar concentration of considered functional groups, c (in M = mol/L), the thickness of the sample, l (in cm), and molar absorption coefficient, ε (in $M^{-1}cm^{-1}$) of a proportional constant as,

$$A = \varepsilon c l. \tag{2.2.1}$$

The molar absorption coefficient and the sample thickness are considered as unchanged during the irradiation. This means the change in absorbance corresponds to the change in molar concentration in the sample, which leads us to the quantitative analysis.

2.3. Combined use of Karl Fischer titration and FT-IR

In order to determine the amount of water absorbed in PADC, the author applied the Karl Fischer titration method, which is widely used to trace the amount of water in various kinds of samples. Figure 2.3.1. (a) shows the body of the system (AQ-2200,

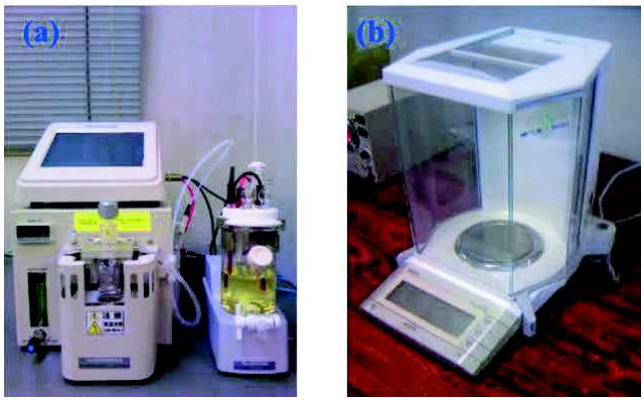

Fig. 2.3.1. Karl Fischer Coulometric Titrator, EV-200 (a), and electronic balance, AG245 (b),.

Hiranuma Sangyo Co., Ltd., Japan), which is connected to the Evaporator with the maximum temperature of 350℃ (EV-200, Hiranuma Sangyo Co., Ltd., Japan). The detection lower limit of AQ-2200 is 10 μg of water. In the present study, we set the temperature of the Evaporator as 160℃, by which almost all water desorbed from the PADC samples.

An electronic analytical scale (AG245, METTLER TOLEDO, Japan) was also used to determine the mass of water absorbed in the PADC (Fig. 2.3.1 (b). In this method, the lower detection limit is 0.1 mg.

Figure 2.3.2 shows three different IR spectra of un-irradiated PADC films around the peaks of OH in the vibration mode. The spectrum in red is of the pristine film measured in ambient air, exhibiting three peaks; (1) the peak of anti-symmetric vibration of water at 3620 cm^{-1}, (2) that of symmetric vibration of water or OH group on the polymer network at 3570 cm^{-1} and (3) that of first over-tone of carbonyl at 3480 cm^{-1}. The spectrum in blue is obtained under vacuum condition during the measurements. The

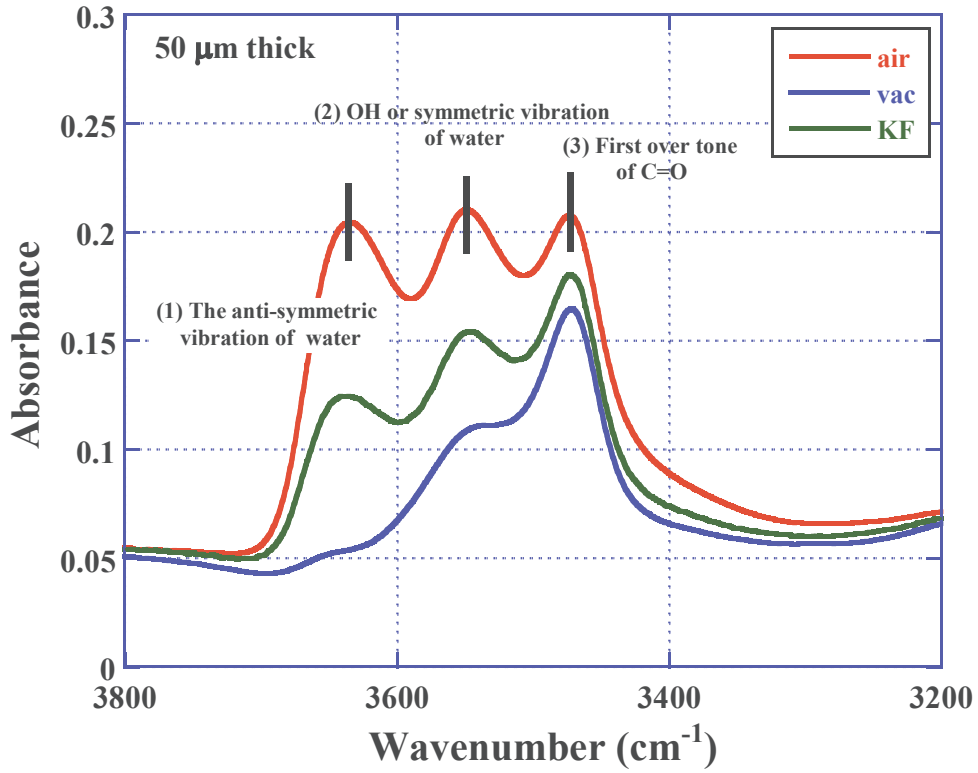

Fig. 2.3.2. IR spectra of a pristine PADC film around OH groups. The spectrum in red is measured in air before measurements, in green measured in air after the Karl Fischer measurement with 160℃and in blue measured in vacuum.

height of the peak (1) is remarkably reduced, indicating the desorption of water from the PADC film. The residual signal at the peak (2) should correspond to the density of OH groups existing in pristine PADC films. The spectrum in green is obtained after Karl Fisher measurement with 160℃. By this temperature, almost all water is released from the PADC films. The observed peaks (1) and (2) are caused by the absorption of water in PADC film between the measurements by Karl Fisher and FT-IR.

2.4. Gamma ray irradiation

The PADC samples were exposed to gamma ray in ambient air generated by the Co-60 source of the "Rabbit11" at The Institute for Scientific and Industrial Research (ISIR) Osaka University, Japan, of which the intensity was 167.7 TBq at October 1st in 2016. Each sample was sandwiched in between 2 mm thick PMMA sheets in order to achieve the electron equilibrium condition. The samples were installed at 25 cm from the source (Figure 2.4.1), where the absorbed dose rate was 1.6 Gy/s. The examined absorbed doses were ranging from 30 to 150 kGy. In the present study, the value of 0.2 eV/nm was used as the averaged *LET* for the secondary electrons produced by the gamma ray. This value was reported as *LET* for water (Kondo&Shinozaki, 1980).

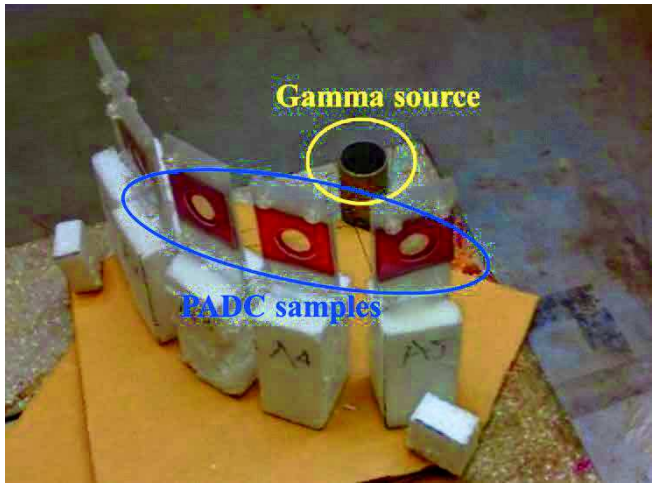

Fig. 2.4.1. Experimental set up for gamma exposures from Co-60.

2.5. Ultra Soft X-ray (USX) irradiation

Ultra Soft X-ray (USX): photon energy < 5 keV, exposures were made at room condition at the Université de Bourgogne-Franche-Comté, France. In this study, the USX from Kα line of Al was utilized. The energy of USX was around 1.5 keV. The uniform beam profile was guaranteed to be at least 3 mm in a diameter (Ounoughi et al., 2013). Figure 2.6.1 shows the air Kerma rate measured by ionizing chamber against the distance from Al chamber. The air Kerma rate increases with decreasing the distance from the Al source. The results corresponded well with the estimation using FLUKA code (Groetz et al., 2014). The PADC samples were installed at 3 mm from the Al source, where the air Kerma rate was 1.3 Gy/s (Figure 2.5.1). The air Kerma rate was easily converted to the photon fluence rate, φ, as,

$$\varphi = d\left[E(\mu_{en}/\rho)_{air}\right]^{-1}, \tag{2.5.1}$$

where d is distance from the source, E the average photon energy and $(\mu_{en}/\rho)_{air}$ the mass energy absorption coefficient in the air as 1.188×10^{3} cm^2g^{-1} (Groetz et al., 2014). The author can obtain the absorbed dose rate, D_s, at the incident surface using (Fullford et al., 1999),

$$D_s = \varphi(\mu_{en}/\rho)_{air}E. \tag{2.5.2}$$

Since the USXs are attenuated in the samples, the mean absorbed doses, D_m, are calculated from following formula (Fullford et al., 1999),

$$D_m = D_s \frac{1-\exp\{-(\mu/\rho)_{PADC}\,\rho l\}}{(\mu/\rho)_{PADC}\,\rho l}, \qquad (2.5.3)$$

where $(\mu_{en}/\rho)_{PADC}$ is the mass energy absorption coefficient in PADC, ρ the density of PADC and the l sample thickness. In the present study, the D_m was about 1.0 Gy/s. The stopping power of electrons produced by photoelectric effect in PADC was estimated as 13.3 eV/nm using the stopping power and range tables for electron, ESTAR, (Berger et al., 2005).

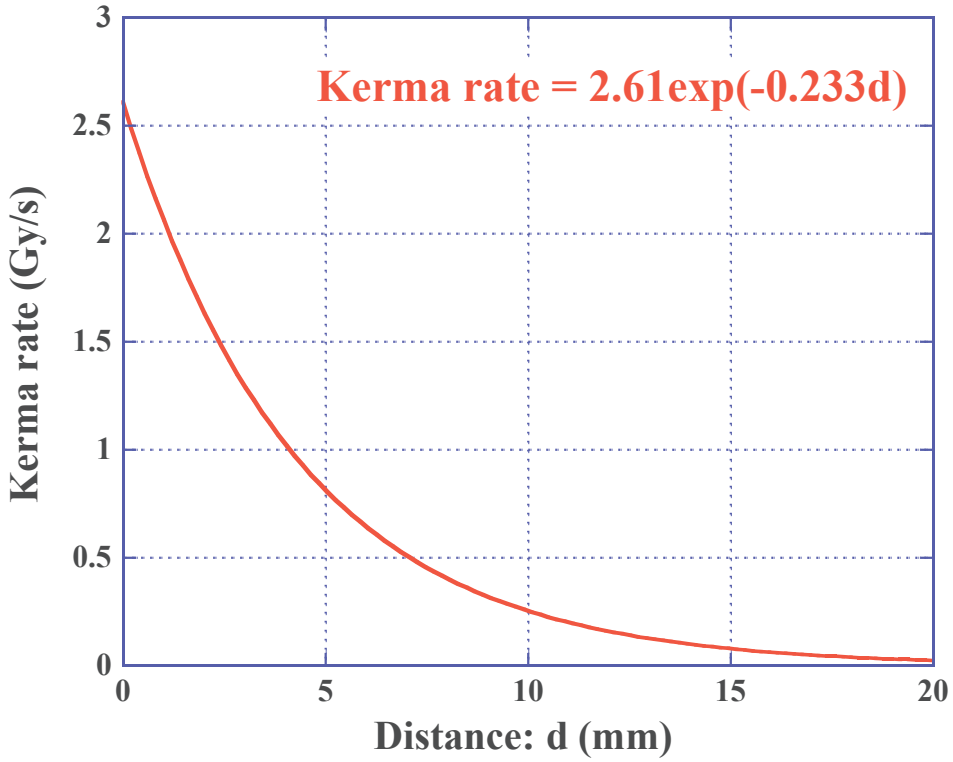

Fig. 2.5.1. Air Kerma rate measured by ionizing chamber against the distance from the Al source (Groetz et al.,2014).

2.6. 28 MeV electron beam irradiation

The thin PADC films were exposed to 28 MeV electrons at the L-band linear accelerator installed at ISIR (pulse duration: 8 ns, peak current: 10.5 A). The average flux was 5.2×10^{13} electrons/cm^2/s, which was concordant with 1.6 kGy/s. The size of beam spot was 2 mm in a diameter which was measured by Gafchromic HD-810 films (ISP, USA) before each irradiation. FTR-125 cellulose triacetate (CTA) dosimeter (Fuji Film, Japan) was used in order to measure the absorbed doses (Oda et al., 1997). As an approximation, the deposited energy of 28 MeV electron per unit distance in PADC was

estimated as 0.03 eV/nm using the relation between the absorbed dose and the electric current. The thin PADC samples were set at 40 cm from the beam port of Ti window. In order to investigate the influence of Bremsstrahlug photons from Ti window and the air, the energy spectrum of electrons was calculated using the Monte Carlo particle and heavy ion transport code system, PHITS Ver.2.76 as shown in Fig. 2.6.1 (Sato et al., 2013). The energy was widely spread from 0 to 28 MeV. The absorbed doses of each electrons produced by Bremsstrahlug photons were then obtained as indicated in Fig. 2.6.2. The absorbed dose of 28 MeV electron was at least 4 order magnitude greater than low energy ones. This implies that the influence of Bremsstrahlug photons is negligible in the present experiment.

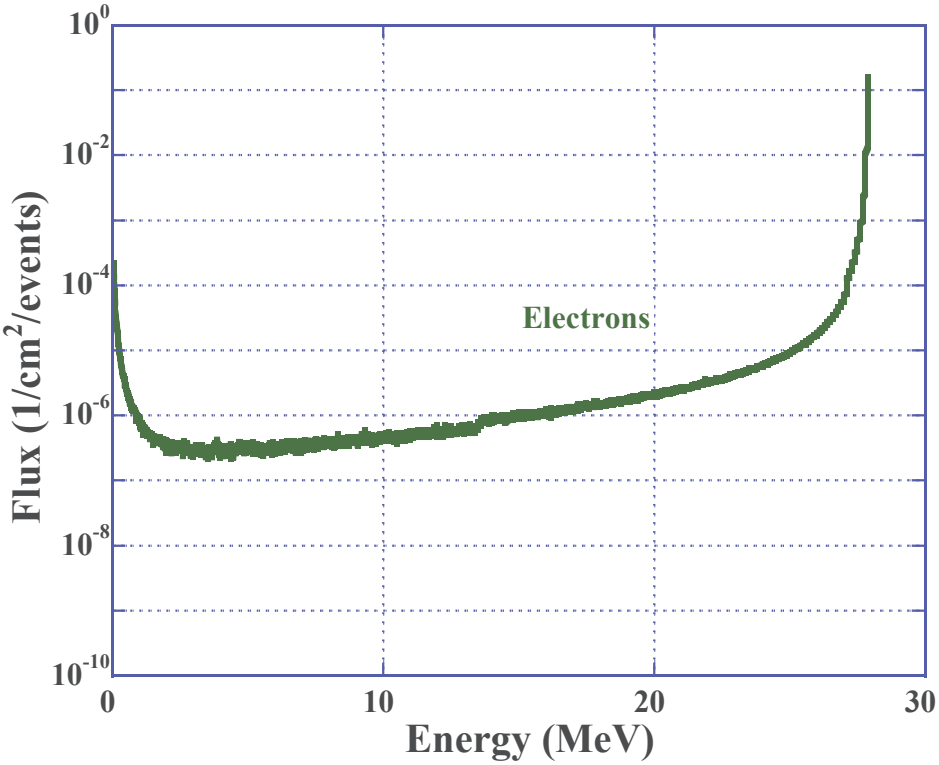

Fig. 2.6.1. Simulated energy spectrum of the electrons by the Bremsstrahlung photons.

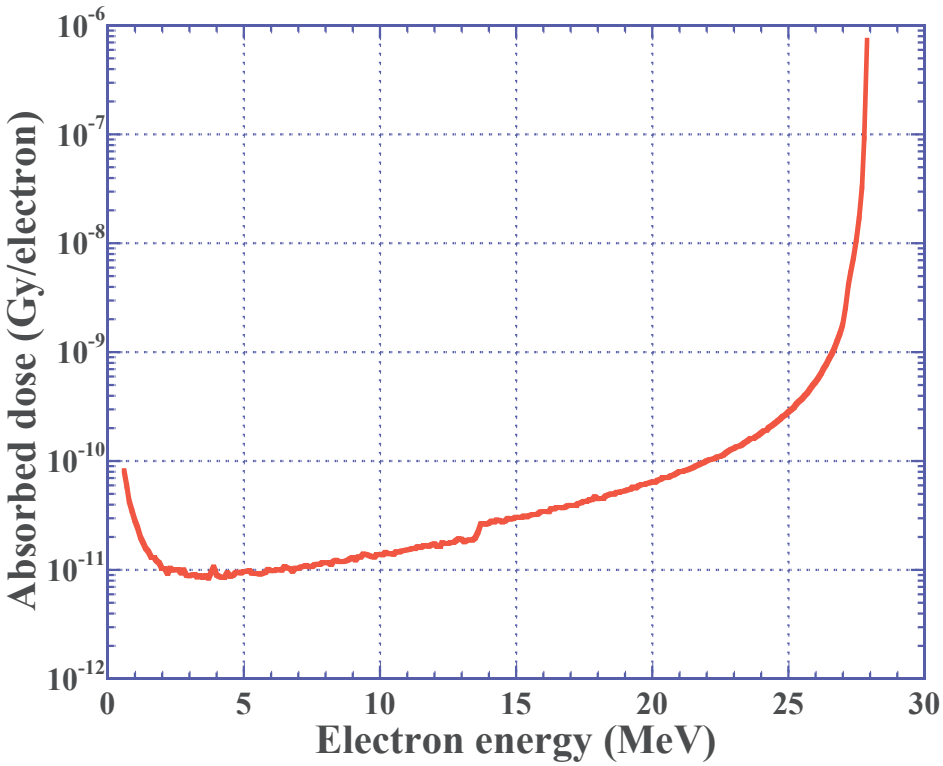

Fig. 2.6.2. Absorbed doses of electrons per each event produced by Bremsstrahlung photons.

2.7. UV irradiation

The UV photon irradiations were carried out using an excimer lamp of UER20H-222c (USHIO Inc., Japan) with a wavelength of 222 nm. The fluence rate of the lamp was monitored by an accumulated UV meter, UIT-250 (USHIO INC., Japan). The author measured the UV-Visible absorption spectrum of the PADC film with a thickness of 3.3 μm in order to evaluate the absorption rate of incident photon at 222 nm (Figure 2.7.1). At the wavelength of 222 nm, the absorbance is about 0.1. This means 80% of incident photons pass through the PADC film. The individual photon emission spectrum was observed at the wavelength of 222 nm (inset of Figure 2.7.1) using Fastevert S-2400 (Soma Optics. Ltd., Japan).

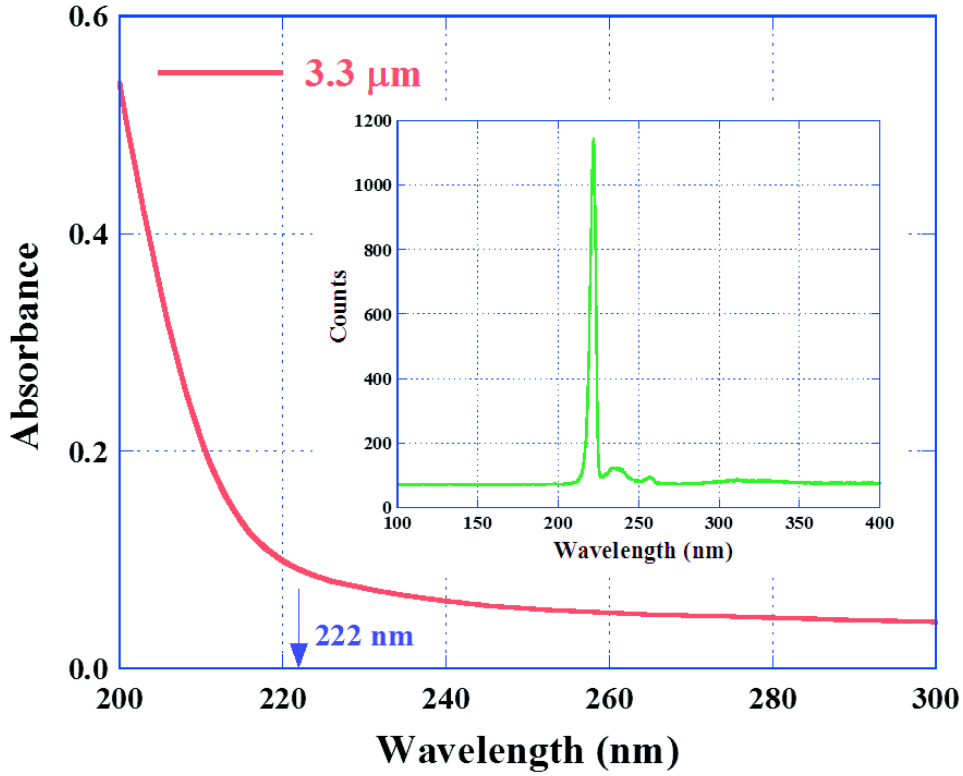

Fig. 2.7.1. UV-Visible spectrum of the pristine PADC film with a thickness of 3.3 μm. The inset is the monochromatic photon emission spectrum with a photon energy of 5.59 eV.

2.8. High energy protons and other ions irradiation

High energy proton exposures with energies of 20, 30 and 70 MeV were performed in ambient air using the NIRS-930 cyclotron equipped at the National Institute of Radiological Sciences, NIRS, Japan (Kanazawa et al., 2010). The flux was calibrated by ionizing chamber during all irradiation. The uniform beam profile was guaranteed at within 4 cm in the center which was measured by Gafchromic EBT3 films (Ashland Inc. USA).

Proton and heavy ion irradiations with energies of less than 6 MeV/u were also carried out in air at Medium Energy Irradiation room, MEXP, of Heavy Ion Medical Accelerator in Chiba, HIMAC, of NIRS. The electronic stopping powers were calculated using SRIM code (Ziegler et al., 2004). The experimental points in cyclotron are plotted as the square symbols, as well as those in MEXP as the circle symbols as a function of the β, velocity of the ion speed normalized to the light speed in vacuum (Figure 2.8.1). The examined stopping powers are ranging from 1.2 to 1,2000 eV/nm. The irradiation conditions in MEXP and Cyclotron are listed in Table 2.4.1. The experimental conditions in cyclotron are written in bold characters.

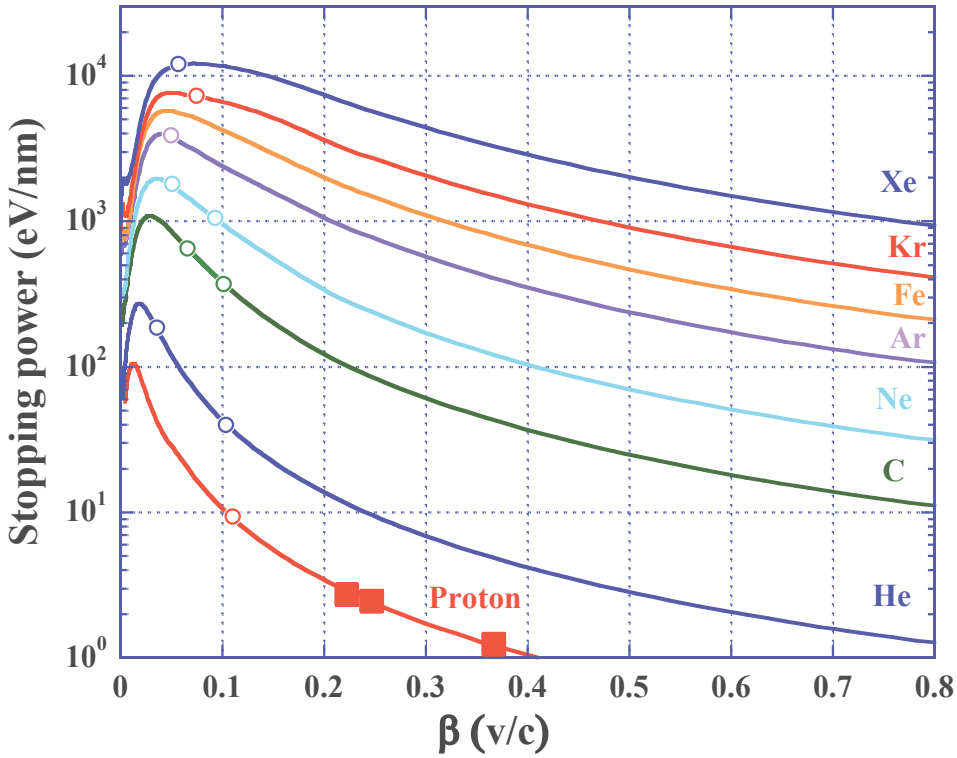

Fig. 2.8.1. Experimental conditions for the incident energy plotted on the graph of the stopping power against the normalized ion speed β. The experimental points in cyclotron are plotted as the square symbols, as well as those in MEXP as the circle symbols.

Commercially obtained BARYOTRAK sheets with thickness of 0.9 mm were stacked to examine etch pits formation in wide stopping power range. The PADC stacks were exposed to He and C ions with energies of 180 and 135 MeV/u, respectively in ambient air at biological irradiation room of HIMAC. After the irradiations, the PADC sheets were etched for 4 hours in 6 M KOH kept at 70℃. The size of open mouth of etch pits was evaluated using optical microscope (BX60-F3, OLYMPUS, Japan), which was operated by WinROOF ver. 5.04 imaging processor (MITANI Corporation, Japan).

Table 2.8.1. Irradiation conditions in NIRS.

Ion	Incident energy (MeV/u)	Electronic stopping power (eV/nm)
Proton	**70**	**1.2**
	30	**2.5**
	20	**3.6**
	5.7	9.3
He	5.0	40
	0.6	210
C	4.8	370
	2.1	650
Ne	4.1	1100
	1.2	1800
Ar	1.5	3700
Fe	2.6	5200
Kr	2.6	7300
Xe	2.3	12000

2.9. Track overlapping model

The track overlapping model can describe the accumulation process of cylindrical tracks in homogeneous medium (Yamauchi, 2003). The tracks are assumed to be identical cylinder and to be distributed randomly, but parallel to each other. In the case of normal incidence on a plane surface, the tracks are treated as the assembly of small circles. The track overlapping model was applied to evaluate the cross sections on biomolecules and to understand the cross linking process in polymer (Salehpour et al., 1984; Seki et al., 2004). This model was also utilized to investigate the distribution of etch pits in μm order (Zylstra et al., 2012). In previous studies, the track core size in PADC exposed to proton and heavy ions was estimated using the track overlapping model and the fluence dependence of UV spectra (Yamauchi, 2003; Yamauchi et al., 2003a&2005a). The obtained results were in great agreement with the effective track core radius for loss of ether, which was estimated by FT-IR spectroscopy within the

experimental error (Mori et al., 2011).

Figure 2.9.1. illustrates the simple simulation result using the random number at a fluence region between 1×10^{11} and 1×10^{13} ions/cm^2, where track core radius is assumed as 3.5 nm as an example (Yamauchi et al., 2000). The lengths of each side of the map are 100 nm. The occupied area by tracks increases monotonically with fluence. It is essential

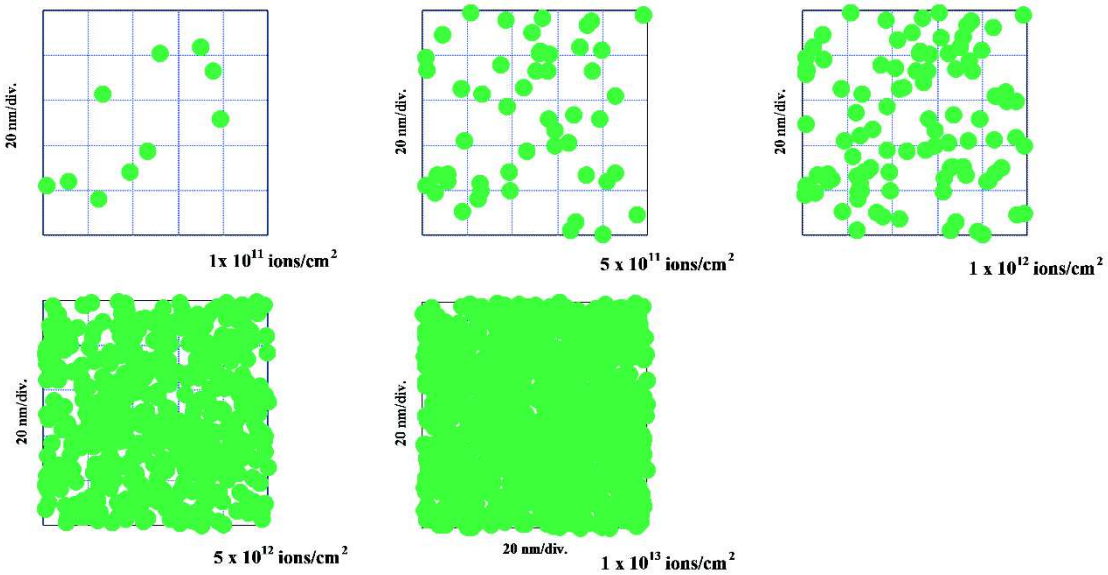

Fig. 2.9.1. Track accumulation process with a radius of 3.5 nm (Yamauchi et al., 2000). The length of one side is set as 100 nm.

to emphasize that the track overlapping is confirmed even at 5×10^{11} ions/cm^2. In previous studies, the critical fluence where track overlapping becomes significant has been determined by the fluence dependence of UV spectra of PADC. The critical fluence has been defined as the arithmetic mean of the critical fluence band (Yamauchi et al., 2000).

In general, tracks are described as circles with an area of σ (in cm^2). In the case of normal incidence, the area is given by $\sigma=\pi r^2$, where r is the track core radius. The track accumulation process is similar to the wetting process of the ground by raindrops. The occupied area at a certain fluence ϕ is expressed by following equation (Salehpour et al., 1984; Yamauchi, 2003; Seki et al., 2004),

$$A(\phi)=1-\exp(-\sigma\phi). \quad (2.9.1)$$

An example with a track core radius of 3.5 nm, corresponding track area, σ, is 3.9×10^{-13} cm^2, is shown by a solid curve (Figure 2.9.2). The two and three fold areas are indicated as $A_2(\phi)$ (Chain line) and $A_3(\phi)$ (Dotted line), as well as the occupied area without overlapping $A_1(\phi)$ (Broken line). Equation (2.9.1) can be easily expanded as (Yamauchi, 2003),

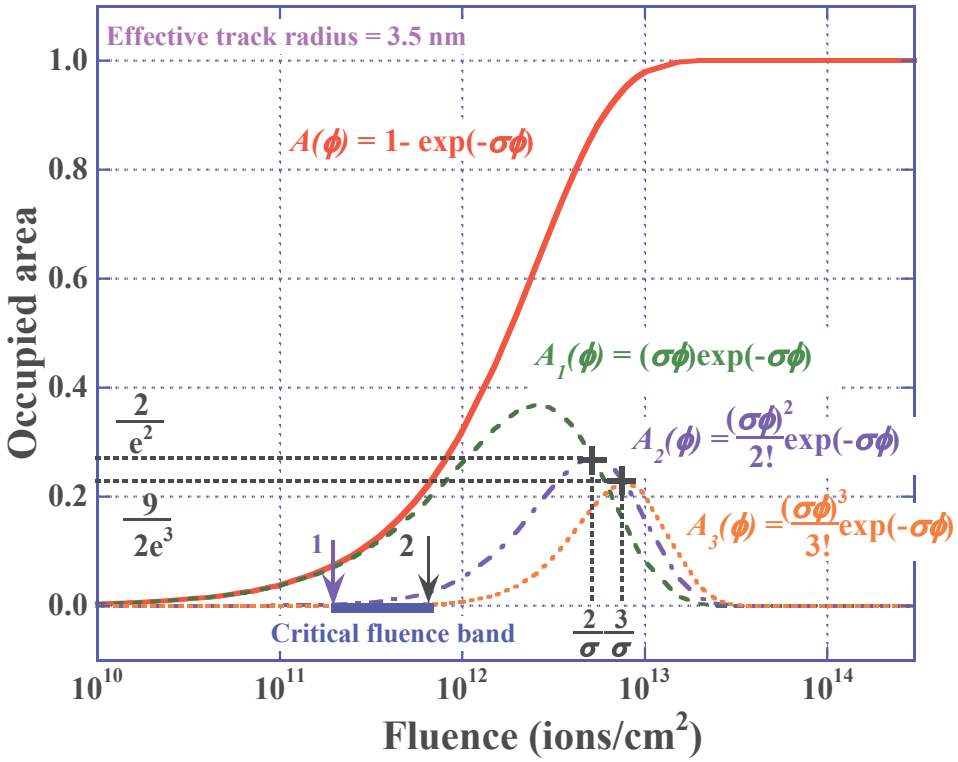

Fig. 2.9.2. Fraction of area occupied by tracks with different folds.

$$A(\phi)=(\sigma\phi)\exp(-\sigma\phi)+\frac{(\sigma\phi)^2}{2}\exp(-\sigma\phi)+\frac{(\sigma\phi)^3}{6}\exp(-\sigma\phi)+\cdots. \quad (2.9.2)$$

The first term of the right in Eq. (2.9.2) indicates the occupied area without the overlapping. The second and third terms of the right express occupied area with doubled and re-doubled overlapping, respectively. Thus, the occupied area of N-folds is simply described as,

$$A_N(\phi)=\frac{(\sigma\phi)^N}{N!}\exp(-\sigma\phi). \quad (2.9.3)$$

This equation is quite similar to the form of Poisson distribution with mean value of $\sigma\phi$. However, the variable is ϕ, not N in this case. The maximum value of $A_2(\phi)$ is $2/e^2$ at a fluence of $\phi=2/\sigma$ and that of $A_3(\phi)$ is $9/2e^3$ at a fluence of $\phi=3/\sigma$. The peaks of the present case are at fluences of 5.2×10^{12} and 7.8×10^{12} ions/cm^2, respectively.

The critical fluence band has been determined as follows: on one hand, the lower end is determined as the fluence where 1% of the maximum of $A_2(\phi)$; on the other hand, the fluence of 1% of maximum of $A_3(\phi)$ is applied to the higher end. Their arithmetic mean is defined as the critical fluence where track overlapping becomes significant. In the present case, the band begins from 2.0×10^{11} ions/cm^2 (Arrow 1 in Fig. 2.9.2) and ends at 6.7×10^{11} ions/cm^2 (Arrow 2 in Fig. 2.9.2). Then, the critical fluence can be derived as 4.4×10^{11} ions/cm^2. By repeating similar calculations, the relation between the critical

fluence and the track size can be evaluated (Figure 2.9.3). The square symbols are previously obtained results of proton and He, C and O ions using track overlapping model (Yamauchi et al., 2000).

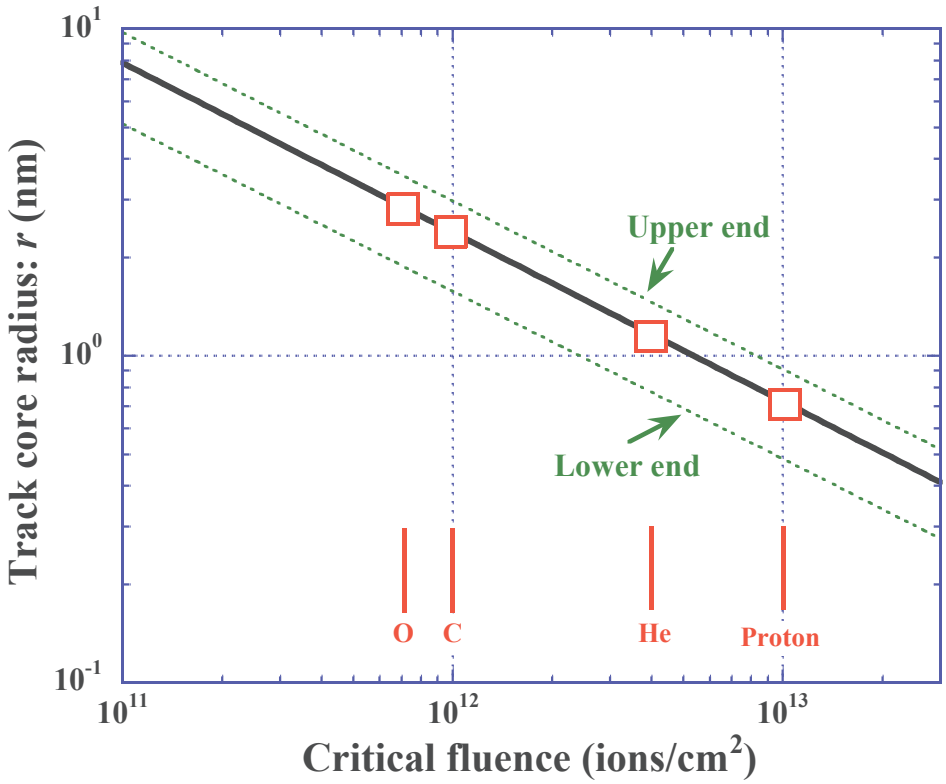

Fig. 2.9.3. Relation between track size and critical fluence. Plotted points are the results derived by track overlapping model (Yamauchi et al., 2000).

2.10. Monte Carlo simulation using Geatnt4-DNA toolkit

The contribution of secondary electrons to the creation of the permanent damages in PADC was examined using a Monte Carlo simulation in the Geant4-DNA toolkit (Bernal et al., 2015; Incerti et al., 2010). One of the aims of Geant4-DNA is the evaluation of radiation damages at the cell level. Nowadays, the electromagnetic interactions and the diffusion process of the radicals in a liquid water can be calculated (Allison et al., 2003&2016; Agostinelli et al., 2003). Figure 2.10.1. shows a single proton track with an energy of 5.7 MeV in water sphere as represented in the blue line. A lot of secondary electrons are generated surrounding the proton track as shown in the red lines. The yellow points indicate the reaction points. The author can simulate the discrete processes of ionization, excitation, elastic scattering and molecular attachment for electrons with the energy down to 7.4 eV. In addition to this, the ionization process for

heavy ions up to Fe can be considered (Incerti et al., 2014). In this study, the author utilized the "G4EmDNAPhysics" physics constructer installed in Geant4-DNA version 10.3.p01. In the present study, virtual stopping media, named "Modified water", is set as a target instead of PADC. The virtual stopping media has a same chemical composition as water but a density is 1.31 g/cm^3, which is equivalent to that of PADC.

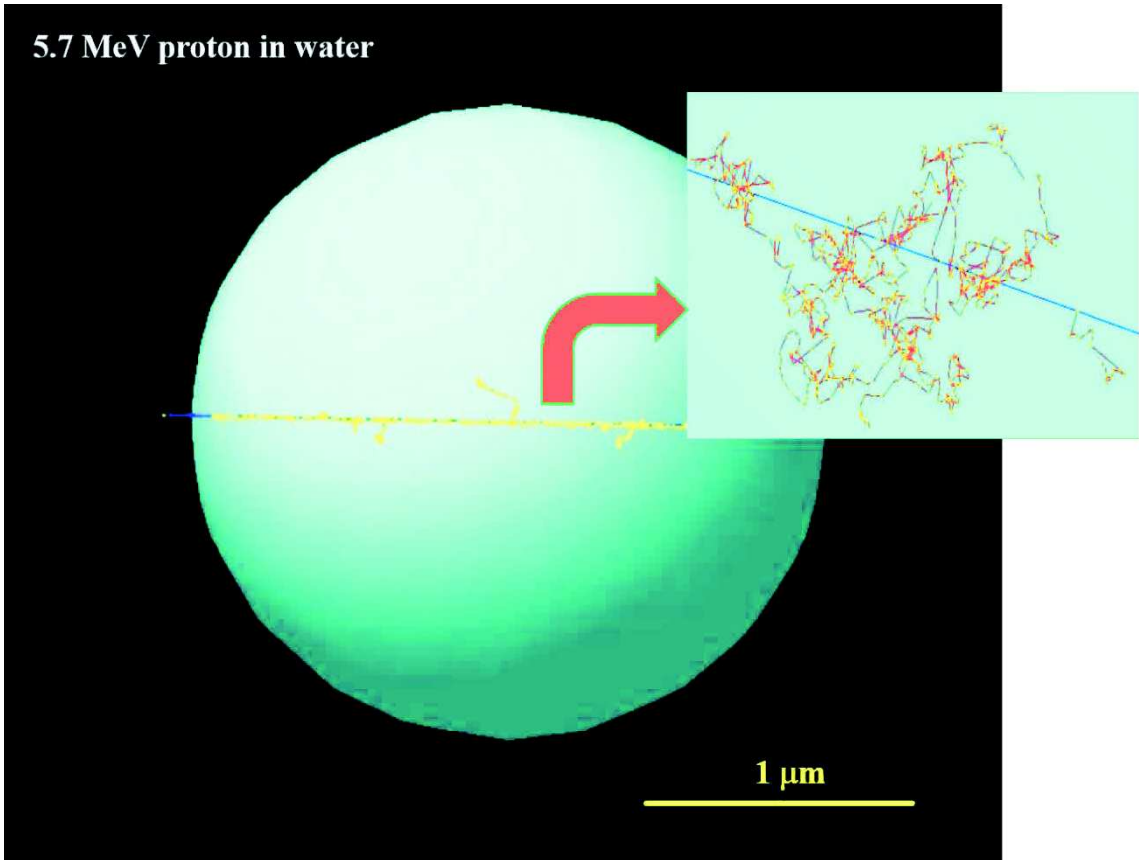

Fig. 2.10.1. The track structure of single proton track with an energy of 5.7 MeV in liquid water.

Chapter 3
Generation of OH groups after the irradiation

In this chapter, the molar absorption coefficient of OH groups in PADC is determined. IR spectra are measured in ambient air to follow the drying process of water absorbed in PADC. The author then estimates the amount of OH groups which decorate the new end-points in PADC after the irradiations with proton and heavy ions. In the present estimation, the author assumes that the molar absorption coefficient of OH groups in water is equivalent to that of OH groups decorating new end-points formed after the irradiation. To avoid the effects of CO_2 and water in ambient air and absorbed in PADC, IR spectra are measured under vacuum before and after the irradiations. The obtained results are compared to damage density of ether.

Dans ce chapitre, le coefficient d'absorption molaire des groupes OH dans le PADC est déterminé. Les spectres IR sont mesurés dans l'air ambiant pour suivre le processus de séchage de l'eau absorbée par le PADC. L'auteur estime ensuite la quantité de groupes OH formés dans le PADC après les irradiations avec des protons et des ions lourds. L'auteur suppose que le coefficient d'absorption molaire des groupes OH dans l'eau est équivalent à celui des groupes OH formés après irradiation. Pour éviter les effets du CO2 et de la vapeur d'eau, les spectres IR sont mesurés sous vide avant et après irradiation. Les résultats obtenus sont comparés à la quantité d'endommagement des fonctions éther.

3.1. Molar absorption coefficient of OH groups in PADC

The schematic views of latent tracks formed in PADC are illustrated in Fig. 3.1.1. Molecular chains of PADC are bombarded during the irradiation. In such a case, CO_2 gas and ethylene like molecules are released away resulted from the segmentation of the radio-sensitive sections (Yamauchi et al., 2005). Some new radicals become new end-points decorated by OH groups, others may recombine each other. The generation of OH groups and recombination are competitive processes. Significant fractions of recombination are resulted from altered configuration which is distinguished from the simple recombination. To elucidate the modified structure in PADC irradiated with proton and heavy ions, the author quantitatively evaluates the generation amount of OH groups. The generation amount of OH groups which are the hydrophilic groups is strongly related to the track etching velocity in aqueous solution.

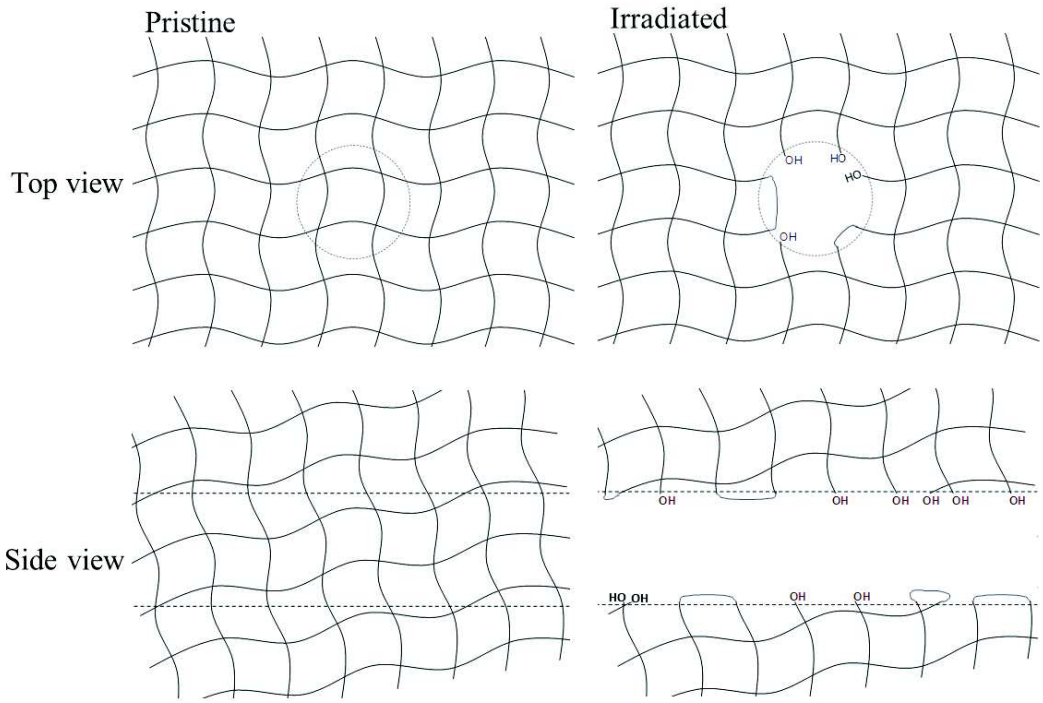

Fig. 3.1.1. Schematic view of the latent tracks formed in PADC.

To assess the amount of OH groups forming new end-points after irradiations, the author has to determine the molar absorption coefficient of OH groups in PADC in advance. Figure 3.1.2. shows the drying process of water absorbed in the pristine PADC film with a thickness of 100 μm from 10 to 90 min in ambient air. On IR spectra around 3500 cm^{-1}, three peaks can be clearly observed. The first peak is the anti-symmetric vibration of water at 3635 cm^{-1}, the second is symmetric vibration of water or OH groups at 3550 cm^{-1} and the last one is the first overtone of the carbonyl at 3470 cm^{-1} (Malek and Chong, 2000). Since water has two peaks, it is not adequate to express absorbance by

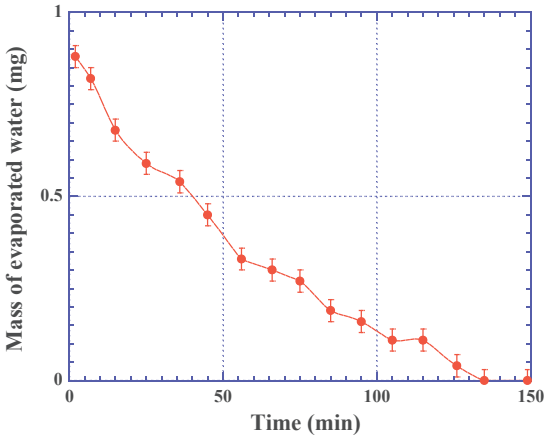

Fig. 3.1.2. Drying process of water absorbed in PADC with a thickness of 100 μm measured in ambient air (Kusumoto et al., 2015).

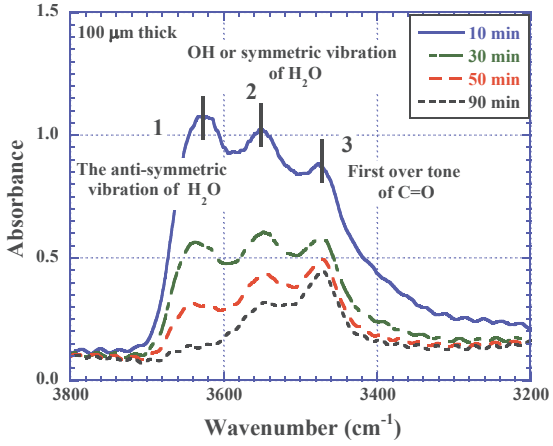

Fig. 3.1.3. Evaporation behavior of water absorbed in PADC as a function of time. The mass of water is measured by electronic balance.

their height. The absorbance evaluated using the areas under the each peak is also effective to avoid the influence of shifts and broadenings of peaks and to follow the drying process quantitatively. The reduction of IR spectra is concordant with evaporated water from PADC, in which the saturation level is set as the base. Figure 3.1.3. indicates changes in mass of water with time after the PADC film is picked up from water. The mass of water is evaluated using electronic balance between IR measurements and decreases with increasing the time. In a short time between IR measurements, the author assumes that the water is released from the PADC film in proportion to the time. Thus, one can estimate the mass of water when IR spectra are measured. The molar concentration of OH groups is then determined with paying an attention that a water molecule has two OH groups.

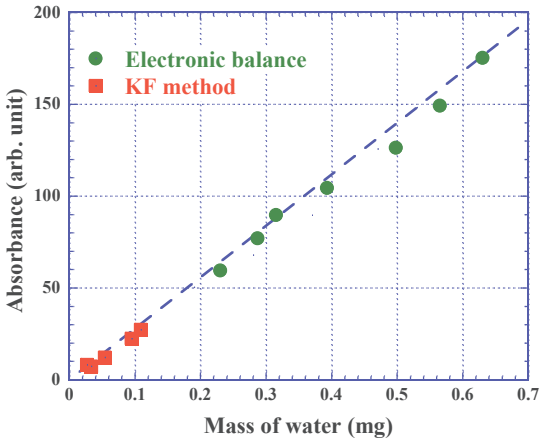

Fig. 3.1.4. Proportional relation between the absorbance on IR spectra and mass of water absorbed in PADC (Kusumoto et al., 2015). The line is guide for eye.

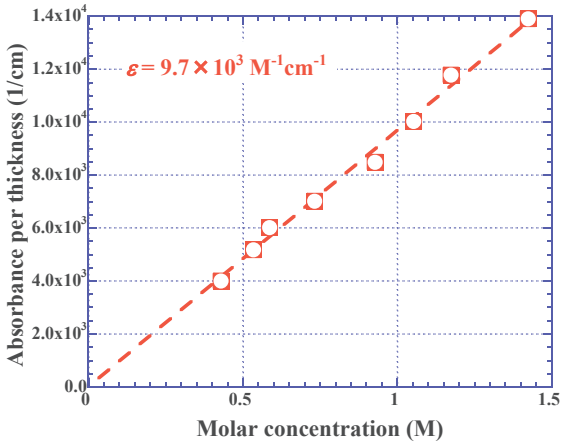

Fig. 3.1.5. Proportional relation between the absorbance per thickness and molar concentration of OH groups in PADC.

The KF method is also applied to evaluate only the mass of water absorbed in PADC with thicknesses of 15, 20, 30, 40 and 50 μm. This makes it possible to get the pure correlation between the mass of water and the absorbance. To obtain IR spectra of water absorbed in the PADC films, the author adapts the difference between spectra measured under vacuum and in ambient air. Repeating these measurements, the author can obtain the proportional relation between the absorbance and mass of water measured by two methods, such as gravimetric method and KF method (Figure 3.1.4). Therefore, the molar absorption coefficient can be estimated using the calibration curve as shown in Fig. 3.1.5. In accordance with the Beer-Lambert law (Eq. 2.2.1), the slope of the calibration curve corresponds to the molar absorption coefficient of OH groups of water absorbed in PADC as $\varepsilon = 9.7\times10^{3}$ $M^{-1}cm^{-1}$. The present value is determined using the absorbance treated as the area under the peaks. Therefore, this value cannot be compared

to the molar absorption coefficient which is obtained from the peak height. In the present study, the author assumes that the molar absorption coefficient of OH groups of water absorbed in PADC is equivalent to that of OH groups of new end-points after the irradiation.

3.2. Quantitative estimation of OH groups in PADC after the irradiation

Figure 3.2.1. represents the IR spectra between 3200 and 3800 cm^{-1} of PADC with a thickness of 15 μm measured in ambient air and under vacuum. The spectrum in green in Fig. 3.2.1 is measured in ambient air and that in red is measured under vacuum. Significant decrease of absorbance is confirmed in the case of the spectrum measured under vacuum. The difference between the two corresponds to the amount of water absorbed in the PADC film. However, the second peak at 3550 cm^{-1} is both observed in in ambient air and under vacuum. Since the first peak at 3635 cm^{-1} disappears under vacuum, the second peak should be assigned to originally existed OH groups in the PADC network. Judging from this, one can ignore the influence of water in the PADC film when the spectrum is measured under vacuum.

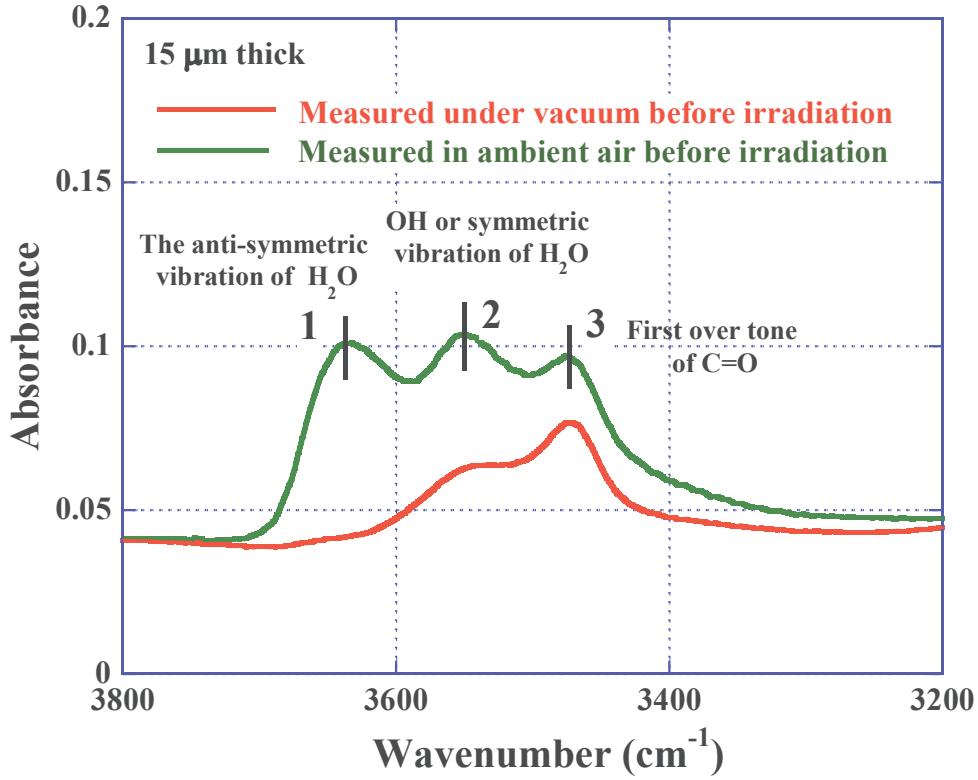

Fig. 3.2.1. IR spectra of pristine PADC film with a thickness of 15 μm measured in ambient air (green) and under vacuum (red).

The amount of OH groups generated as new ending groups after the irradiation has been derived using the following formula,

$$\Delta C = (A - A_0)/\varepsilon l, \tag{3.2.1}$$

where ΔC is the change of molar concentration (in M), A_0 the absorbance after exposure, A the absorbance before exposure and l the thickness of the PADC film (in cm). The amount of OH groups increases with the fluence of 4.8 MeV/u C, 4.1 MeV/u Ne and 1.5 MeV/u Ar ions (Figure 3.2.2). The inset describes the evolution of IR spectra of PADC

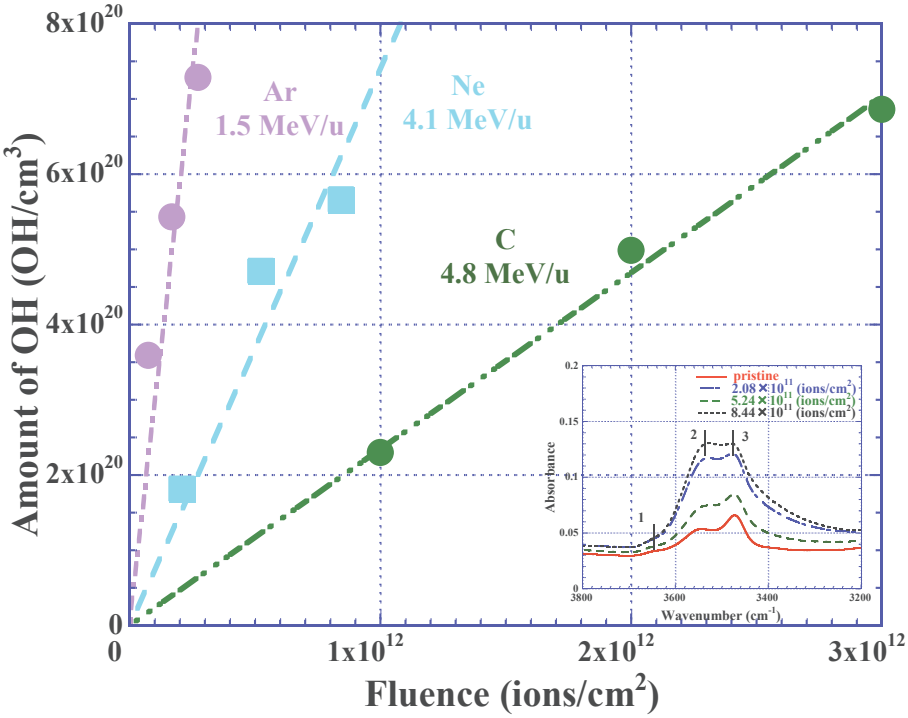

Fig. 3.2.2. Increase of OH groups in PADC exposed to C, Ne and Ar ions with fluence. Inset shows the evolution of IR spectra of PADC around 3500 cm^{-1} measured under vacuum after the irradiation with Ne ion with an energy of 4.1 MeV/u (Kusumoto et al., 2015).

around 3500 cm^{-1} exposed to 4.1 MeV/u Ne ions (Kusumoto et al., 2015). The monotonic increase of the amount of OH groups is observed with fluence. The slope of each fitting line, m, corresponds to the amount of OH groups per unit distance along the ion track (in OH/nm) as,

$$\Delta C = m\phi, \tag{3.2.2}$$

where ϕ is the fluence (in ions/cm^2). The original spectra is utilized in order to assess the amount of OH groups because the maximum reduction rate of carbonyl that is concordant with the reduction of the relative absorbance, A/A_0, is less than 10% in the examined fluence region for each ion (Figure 3.2.3). This implies that the effect by the reduction of carbonyl should be negligible.

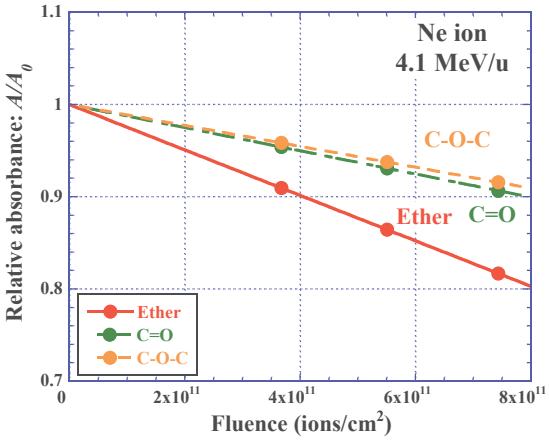

Fig. 3.2.3. Reduction of the relative absorbance, A/A_0, of ether, carbonyl and C-O-C in PADC against the fluence of Ne ions.

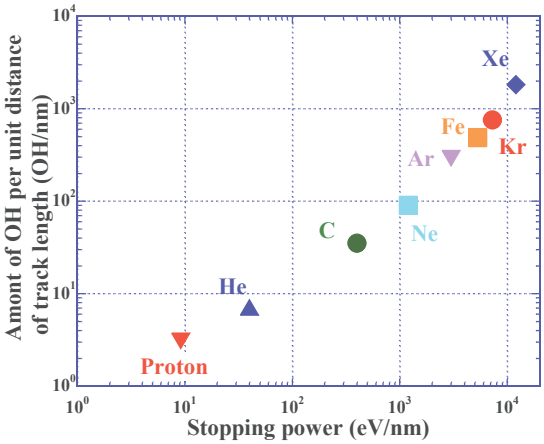

Fig. 3.2.4. Amount of OH groups per unit distance of track length as a function of the stopping power (Kusumoto et al., 2015).

Figure 3.2.4. represents the amount of OH groups per unit distance along the ion track against the stopping power. Since the absorbance is evaluated using the areas under each peak, the large value of the molar absorption coefficient does not affect the amount of OH groups in the present case. The amount of OH groups per unit distance increases monotonically with increasing the stopping power. The error bars are shorter than the plots. Therefore, the error cannot be seen on the plots. Figure 3.2.5. indicates correlation

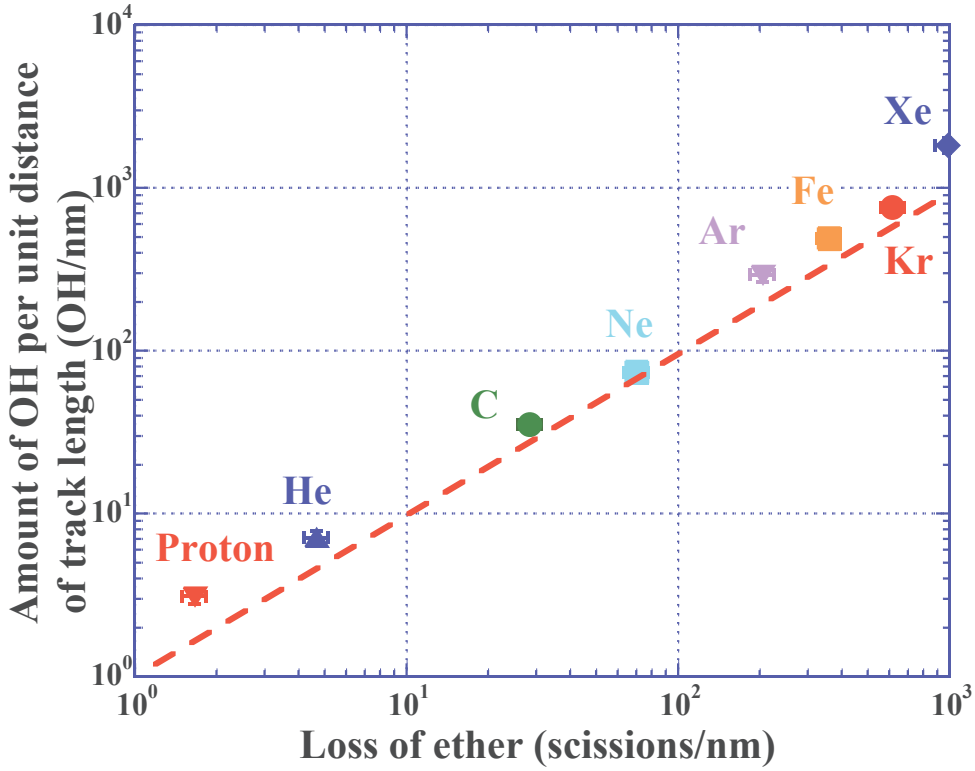

Fig. 3.2.5. Correlation between the generation density of OH groups and damage density of ether. The line is guide for eye (Mori et al., 2011; Kusumoto et al., 2015).

between the generation of OH groups per unit distance and the amount of ether which is amount of breaking ether per unit distance of ion tracks. The generation amount of OH groups per unit distance for proton and Xe, is about twice than the loss of ether. However, the one to one relationship is obtained in the cases of He, C, Ne, Ar, Fe and Kr ions (Kusumoto et al., 2015). This implies that at least one OH group are formed when one ether is lost. The present results confirm the validity of molar absorption coefficient of OH groups in PADC.

The formation of OH groups and the recombination resulted in altered or original configuration are competitive process as reported in the previous work (Mori et al., 2013). Furthermore, the role of ambient oxygen to decoration of OH groups after the irradiation has been discussed (Mori et al., 2013; Barillon et al., 2015). The author must clarify these future issues as a next step.

3.3. Summary for the quantitative analysis of OH groups

Following the drying process of water absorbed in PADC, the molar absorption coefficient of OH groups was determined as $\varepsilon = 9.7\times10^3$ $M^{-1}cm^{-1}$. Using this value, the amount of OH groups decorating the new end-points was assessed. The generation amount of OH groups for He, C, Ne, Ar, Fe and Kr ions was almost equivalent to the damage density for loss of ether. The generation amount of OH groups for proton and Xe ions was about twice than the damage density for loss of ether. This suggested that at least one OH group was generated when one ether was broken. The present results show the validity of the present value of molar absorption coefficient of OH groups in PADC.

Après le processus de séchage de l'eau absorbée par le PADC, le coefficient d'absorption molaire des groupes OH a été déterminé comme étant égal à $9,7\times10^3$ M^{-1} cm^{-1}. La quantité de groupes OH formés pour les ions He, C, Ne, Ar, Fe et Kr est équivalente à la densité d'endommagement des fonctions éther. La quantité générée de groupes OH pour les protons et les ions Xe est environ deux fois supérieure à la densité d'endommagement pour la perte d'éther. Ceci suggère qu'au moins un groupe OH est généré quand un groupement éther disparait.

Chapter 4
Effects of low *LET* radiations and 222 nm UV photons

As reference experiments of ion irradiation, the effects of low *LET* radiations (gamma ray, soft X-ray, electron) and UV photons are examined using FT-IR spectrometry. The damage registration property of low *LET* radiations and UV photons are elucidated using the conventionally developed track overlapping model.

4.1. Gamma ray and Ultra Soft X-ray exposures

In comparison to the ion tracks, low *LET* radiations, such as gamma ray or electrons, give relatively uniform damages to materials. PADC films are exposed to low *LET* radiations with absorbed doses up to 200 kGy which is equivalent to that at proton track core. In this chapter, the previously obtained results are indicated as open symbols. The results from the present study are plotted as solid symbols. In the present study, the traditional unit of scissions/100 eV is used for the radiation chemical yield, G value, not international system unit. The relation between the two units is as in the followings,

$$G\,[\mathrm{mol/J}] = 1.0 \times 10^{-7}\, G\,[\mathrm{scissions/100\ eV}] \qquad (4.1.1)$$

4.1.1. Reduction of the relative absorbance

Figure 4.1.1. (a) and (b) show IR spectra before and after the exposures to gamma ray with absorbed doses of 60 kGy and 150 kGy, respectively. After the 60 kGy exposure, the absorbance of ether at 1026 cm^{-1} decreases but that of carbonate ester (C-O-C at 1250 $cm^{-1}$and carbonyl at 1750 cm^{-1}) and CH groups at 789 cm^{-1} does not decrease.

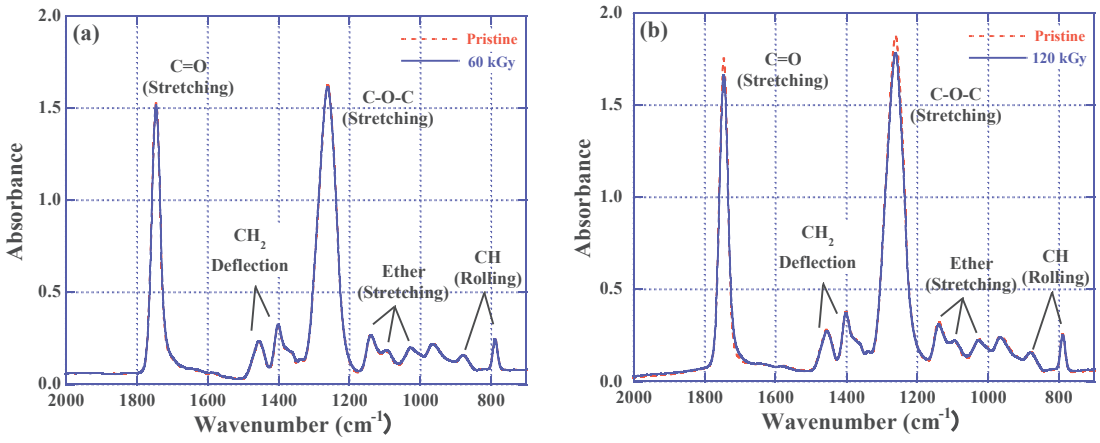

Fig. 4.1.1. IR spectra of PADC films before and after exposures to gamma ray with absorbed doses of 60 kGy (a) and 120 kGy (b).

In comparison to this, the absorbance of typical functional groups in PADC decreases after the 150 kGy exposure. The reduction behaviors of the relative absorbance (the ratio of the net absorbance of the considered bond, A, after the irradiation to the original one, A_0) of typical functional groups in PADC exposed to gamma ray from Co-60 source are shown in Fig. 4.1.2 (Kusumoto et al., 2017). The relative absorbance of ether decreases monotonically with absorbed dose. Based on the Beer-Lambert law (Eq. 2.2.1), the relative absorbance corresponds to the survival fraction, N/N_0, which is the number density of the considered bond N to the original one, N_0. The reduction rate of the relative absorbance of ether is changed above the absorbed dose of 110 kGy. At higher absorbed doses, the reduction rate becomes lower. In comparison to this, the relative absorbance of carbonyl decreases only above the critical dose of 50 kGy. The decreasing behavior of C-O-C composing the carbonate ester is identical to that of carbonyl. In addition, the relative absorbance of CH groups turns out to decrease above the 120 kGy, where is higher than that of carbonyl and C-O-C.

A similar trend is confirmed in the case of Ultra Soft X-ray, USX, (Figure 4.1.3).

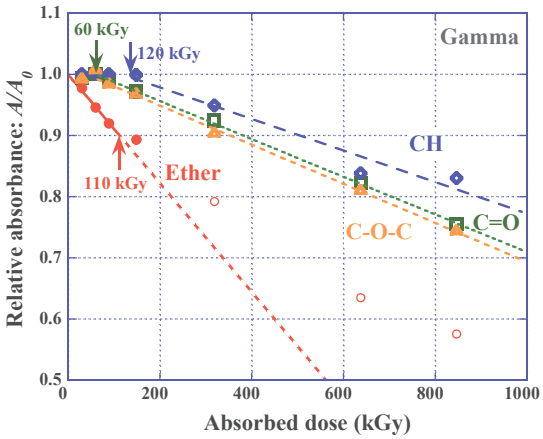

Fig. 4.1.2. Reduction of the relative absorbance of ether, carbonyl, C-O-C and CH groups in PADC exposed to gamma ray. Solid symbols indicate the present results and open symbols indicate previous results (Mori et al., 2009).

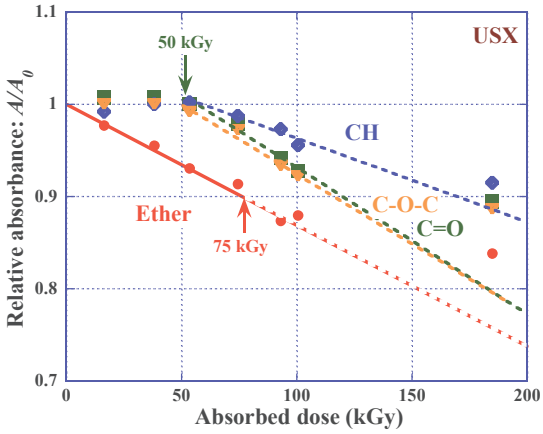

Fig. 4.1.3. Reduction of the relative absorbance of ether, carbonyl, C-O-C and CH groups in PADC irradiated with USX.

The relative absorbance for ether decreases linearly with the absorbed dose up to the 75 kGy. The relative absorbance of carbonyl turns out to decrease above the critical dose of 50 kGy. The critical doses of C-O-C and CH groups are concordant with that of carbonyl. The critical doses of carbonate esters for gamma ray and USX are almost equivalent within the experimental error. In comparison to this, the critical dose of CH groups for gamma ray is twice than that for USX.

Judging from the observed two steps damage formation processes that the

absorbance of carbonyl, C-O-C and CH groups decrease only above the critical doses, the carbonyl can be lost only after the loss of ether with a certain percentage. One possible interpretation of the sudden decrease of the number density carbonyl is the overlapping of electron tracks which are produced by gamma ray and USX exposures. Unfortunately, the previously developed track overlapping model cannot be simply applied to the present cases because the random motions of low energy electrons are far from the linear movements of high energy electrons, protons and heavy ions. The details concerning the track overlapping model are discussed in the following section. However, the author can say that the radio-sensitivity of carbonyl become substantially higher when the closest ether is lost.

4.1.2. Radiation chemical yields for losses of typical functional groups

In order to evaluate the G value, the number of loss of considered bonds per unit energy desorption of 100 eV, for losses of ether in PADC, avoiding the overlapping of secondary electrons, the author adopts the first three and four data sets of gamma ray and USX, respectively (Figures 4.1.2&4.1.3). Equation 4.2.1. has been applied to evaluate the G value in the linear reduction mode,

$$A/A_0 = 1 - kD, \qquad (4.1.2)$$

where D is the absorbed dose (in Gy) and k experimentally obtained constant (in Gy^{-1}). The value of k corresponds to the slope of fitting lines for ethers (in Figs. 4.1.2&4.1.3)

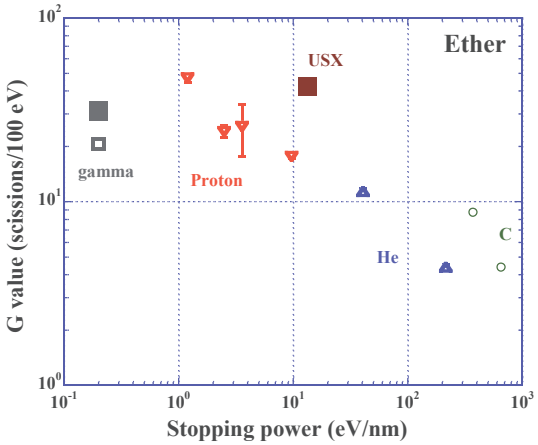

Fig. 4.1.4. G values for loss of ether against the stopping power. The horizontal axis is applied to average *LET* in water as 0.2 eV/nm for gamma ray. The present results are plotted as solid symbols and the previous ones are indicated as open symbols (Mori et al., 2009&2011; Kusumoto et al., 2016a&b).

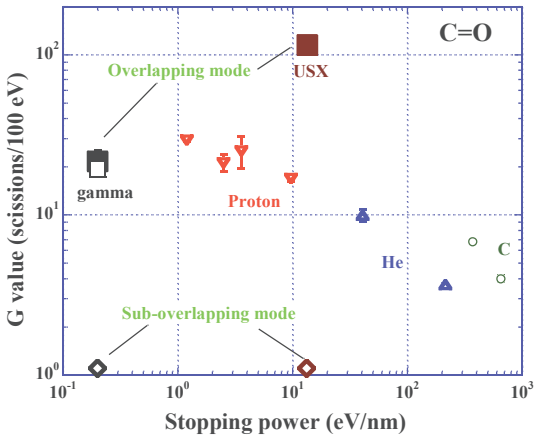

Fig. 4.1.5. G values for loss of carbonyl against the stopping power for protons and heavy ions. The horizontal axis is applied to average *LET* in water as 0.2 eV/nm for gamma ray. The present results are plotted as solid symbols and the previous ones are indicated as open symbols (Mori et al., 2009&2011; Kusumoto et al., 2016a&b).

and is easily converted to G value as,

$$G = 9.64 \times 10^6 N_0 k, \quad (4.1.3)$$

where N_0 is number density of the considered chemical bond (in cm^{-3}).

Figure 4.1.4. shows G values for loss of ether against the stopping power for protons and heavy ions. The horizontal axis of the present cases are applied to the average *LET* in water of 0.2 eV/nm and the stopping power of 13.3 eV/nm for gamma ray and USX, respectively (Kusumoto et al., 2017a). It is true that the stopping power and *LET* are totally different values from the definitions. The author, however, dares to make this comparison to clarify the effects of discrete damage along electron tracks from low *LET* radiations and dense damage along ion tracks. The obtained G value of gamma ray, plotted as solid square, is greater than the previously obtained one, plotted as open square, (Mori et al., 2009). Since the data sets above the 100 kGy were used in the previous study, the G value of gamma ray was underestimated there. The G value of USX is greater than that of gamma ray. This suggests that impacts of low energy electrons may be effective to create irreversible damages in PADC. At odds with this, the G value of 70 MeV proton is greater than that of gamma and USX. Relatively dense damages along the proton tracks play an important role to produce permanent damages compared to the discrete damages produced by gamma ray and USX.

The G values for loss of carbonyl in PADC exposed to gamma ray and USX are also evaluated in both modes of sub-overlapping and overlapping (Figure 4.1.5). The region below the critical dose may be called as sub-overlapping mode because the influence of overlapping of secondary electrons is not observed. The G values in the sub-overlapping mode are extremely small, plotted as open diamonds. In the overlapping mode where is above the critical dose, the G values distinctly enhance, indicated as solid circles (Figure 4.1.4). The present G value of gamma ray in the overlapping mode is almost equivalent to the previous one (Mori et al., 2009). The sudden increase of the G values of gamma ray and USX in the overlapping mode implies that the radio-sensitivity of carbonyl becomes significantly higher beyond the critical doses. In other words, the carbonate ester in PADC is easily broken when neighboring ether is lost. The two steps damage formation process helps us to elucidate the layered structure in PADC, namely the core radius of ether is always greater than that of carbonate ester and other functional sections. Since the overlapping of secondary electrons is popular around the all ion tracks of proton and heavy ions, all functional groups are broken. However, only ether, which is the most radio-sensitive sections in PADC is lost at the distant position from the track center because the amount of secondary electrons is low compared to around the track

center. One must focus on the number of electrons surrounding region of ion tracks at the sub-nano-scale in order to clarify the creation mechanism of latent tracks in PADC. It is important to determine the amount of OH groups after exposures to low *LET* radiations as those of proton and heavy ion tracks. In this thesis, the generation behavior of OH groups is examined using high energy electron beams.

4.2. Effects of 28 MeV electron irradiation

In the present study, the author investigates the effects of not only low energy electrons but also high energy ones. Passes of high energy electrons are recorded as countable straight faults in PADC. This is the reason why the author has conducted the study using 28 MeV electron beams.

4.2.1. Changes in the absorbance of ether, carbonate ester, CH groups and OH groups

Figure 4.2.1 shows the reduction of the relative absorbance, A/A_0, of ether, carbonyl, C-O-C and CH groups in PADC against the fluence (Kusumoto et al., 2016b).

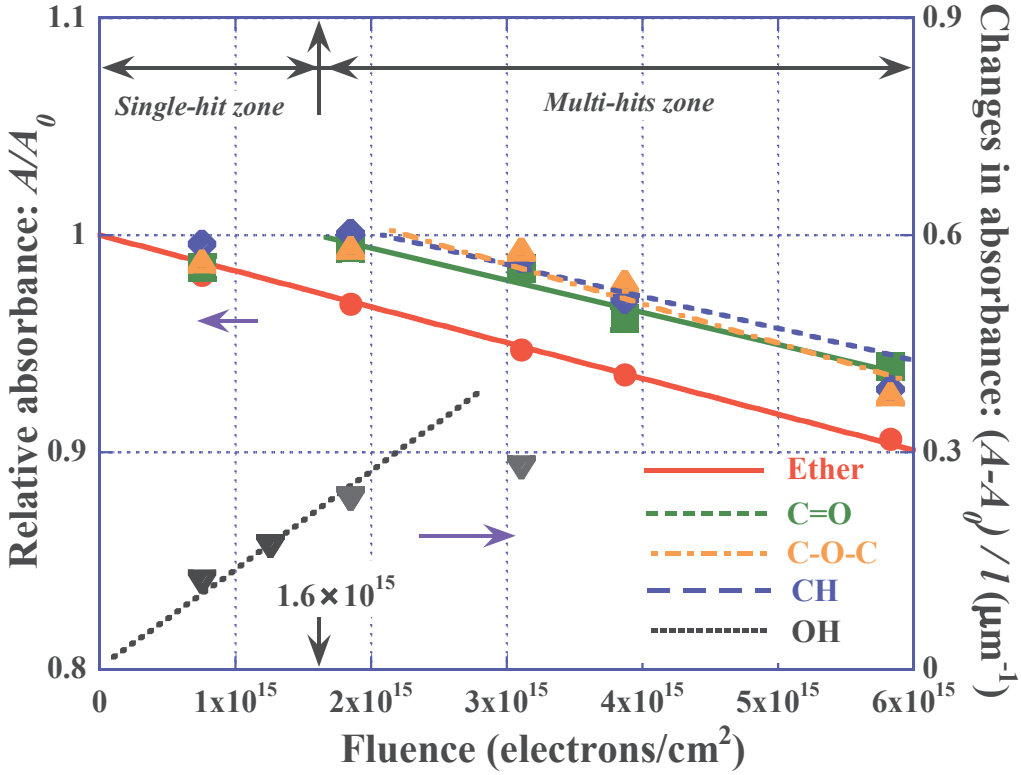

Fig. 4.2.1. Reduction of the relative absorbance of ether, carbonyl, C-O-C and CH groups (left axis) and increase of the absorbance around OH groups (right axis) against the fluence (Kusumoto et al., 2016b).

Changes in absorbance normalized by sample thickness, $(A-A_0)/l$, of OH groups are also represented in Fig. 4.2.1. From the technical limitation that one cannot operate the Micro IR system under the vacuum condition, it was difficult to obtain the uniformly irradiated samples over the measured spots. In using the conventional FT-IR system under vacuum condition, the beam spot is fairly smaller than the measured spot. Therefore, the author simply discusses the changes in absorbance. The relative absorbance of ether decreases linearly with the increasing fluence. The relative absorbance of carbonyl does not decrease up to the critical fluence of 1.6×10^{15} electrons/cm^2. The critical fluence is equivalent to the critical dose of 50 kGy. The value of the critical dose is almost same as those of gamma ray and USX within experimental error. The relative absorbance of carbonyl begins decreasing only above the critical fluence. The trends of C-O-C, which composes the carbonate ester and CH groups are slightly different from that of carbonyl. Above the critical fluence, the generation rate of the changes in absorbance of OH groups clearly decreases (Figure 4.2.1). The possible explanation of the two steps damage formation process on PADC is overlapping of the electron tracks. It suggests that the carbonate ester and CH groups are hardly affected by the single electron. The carbonate ester can be lost when more than two electrons pass through a certain repeat unit. In this study, the fluence region below the critical fluence may be called as the "Single-hit zone". The region above the critical fluence may also be called as the "Multi-hits zone".

4.2.2. Breaking of ether

Since the relative absorbance for ether decreases linearly with the fluence in both zones, the relative absorbance is expressed as,

$$A/A_0 = 1-\sigma\phi, \tag{4.2.1}$$

where ϕ is the electron fluence (in electrons/cm^2), σ the removal cross section for each electron track (in cm^2), which is concordant with the slope of the fitted line. The removal cross sections for ether at both zones are summarized in Table 4.2.1. The effective track radius (in nm), which is a distance from the trajectory where considering bonds should be lost within the radial size, is obtained using σ as,

$$r = \sqrt{\sigma/\pi}. \tag{4.2.2}$$

The effective track radius for loss of ether irradiated with 28 MeV electrons is about 0.02

Table 4.2.1. List of the removal cross sections for typical functional groups in PADC exposed to 28 MeV electrons (Kusumoto et al., 2016b).

	Single-hit zone	Multi-hits zone
σ_{Ether}	$(1.7\pm0.1)\times10^{-17}$	$(1.7\pm0.1)\times10^{-17}$
$\sigma_{C=O}$	-	$(1.4\pm0.1)\times10^{-17}$
$\sigma_{C\text{-}O\text{-}C}$	-	$(1.7\pm0.1)\times10^{-17}$
σ_{CH}	-	$(1.5\pm0.1)\times10^{-17}$

nm. In addition, the damage density, L, (in scissions/nm), that is number of loss of considering bonds per unit distance along the track is easily derived from σ as,

$$L = \sigma N_0. \tag{4.2.3}$$

Figure 4.2.2 shows the damage density defined by the loss of ether in PADC (Kusumoto et al., 2016b). The deposited energy per unit distance is applied to the horizontal axis of 28 MeV electron. The damage density of 28 MeV electron is about 0.005 scissions/nm, which is slightly lower than the extrapolated trend of the previous results of protons and

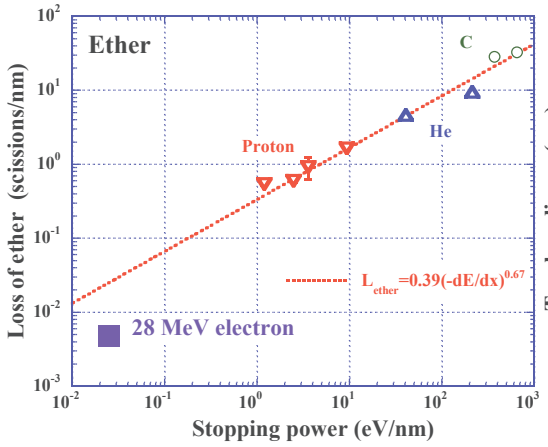

Fig. 4.2.2. Damage density for loss of ether against the sopping power (Kusumoto et al., 2016b). The deposited energy per unit distance is applied to 28 MeV electron.

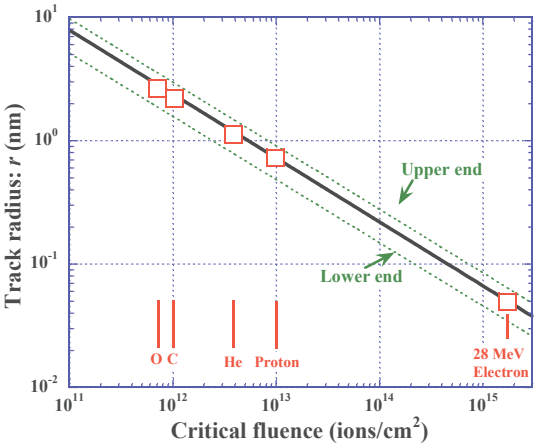

Fig. 4.2.3. Relation between track size and critical fluence. Plotted points are the results derived by track overlapping model (Yamauchi et al., 2000; Kusumoto et al., 2016b).

heavy ions of He and C. Since the length of a repeat unit of PADC is about 2 nm, the scissions due to the 28 MeV electrons are well isolated along the electron trajectory. At odds with this, the damage density of 70 MeV proton is about 0.5 scissions/nm. Therefore, successive damages of ether can be expected along the proton track. This implies that the recombination of radicals returns to the original configuration may be suppressed.

4.2.3. Losses of carbonate ester and CH groups

Equation (4.2.1) can not be simply applied to evaluate the chemical damage parameters for losses of carbonate ester and CH groups in PADC in the Single-hit zone because reduction of the relative absorbance is not observed. Equation (4.2.1) is adapted to evaluate the chemical damage parameters only above the critical fluence. The removal cross sections for carbonyl, C-O-C and CH groups in the Multi-hits zone are summarized in Table 4.2.1. The effective track radius for loss of carbonyl, C-O-C and CH groups in the Multi-hit zone is 0.02 nm which is equivalent to that for ether.

In the previous studies, the track core radius for proton and heavy ions has been estimated based on the track overlapping model and the fluence dependence of UV spectra (Yamauchi, 2003). In the present case of 28 MeV electrons, the track overlapping model is applied regarding the critical fluence of 1.6×10^{15} electrons/cm^2 (Figure 4.2.3). The effective track radius of 28 MeV electron is 0.05 nm, which is in the same order with those of considered functional sections estimated by FT-IR spectrometric studies. This supports the interpretation which the carbonate ester was lost only when more than two electrons passed through a certain repeat unit.

4.2.4. Generation rate of OH groups

The OH groups which decorate new end-points after the irradiation increase linearly with fluence in the Single-hit zone (Figure 4.2.4). The generation rate of OH groups decreases suddenly in the Multi-hits zone. It is difficult to estimate quantitatively the amount of OH groups because the spot size of the FT-IR measurement is larger than that of electron beam in which the uniform intensity is guaranteed. However, the discussion about the generation rate of OH groups is possible. The ether which is the most radio-sensitive sections in PADC is lost in the Single-hit zone as illustrated in Fig. 4.2.4 (a). The new end-points are decorated by OH groups. In the Multi-hits zone, the generated OH groups are released away as a result of the bombardment of carbonate ester as shown in Fig. 4.2.4 (b). Thus, the generation rate of OH groups decreases suddenly in the Multi-hits zone. The new OH groups, of course, decorate the radicals resulted from the cleavage of carbonate ester. This view is concordant with the interpretation that says the carbonate ester is lost when neighboring ether is lost.

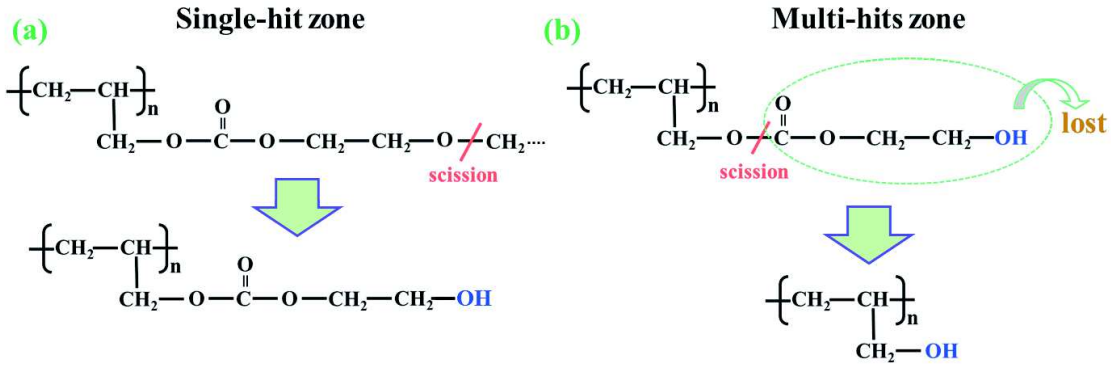

Fig. 4.2.4. Two steps damage formation process in PADC. The ether is broken in Single-hit zone (a) and carbonate ester is lost with the OH groups in Multi-hits zone (b).

4.2.5. G values for typical functional groups in PADC

The G value was attained as the ratio of the damage density to the deposited energy per unit length as,

$$Gvalue = \frac{L}{\left(-dE/dx\right)}. \tag{4.2.4}$$

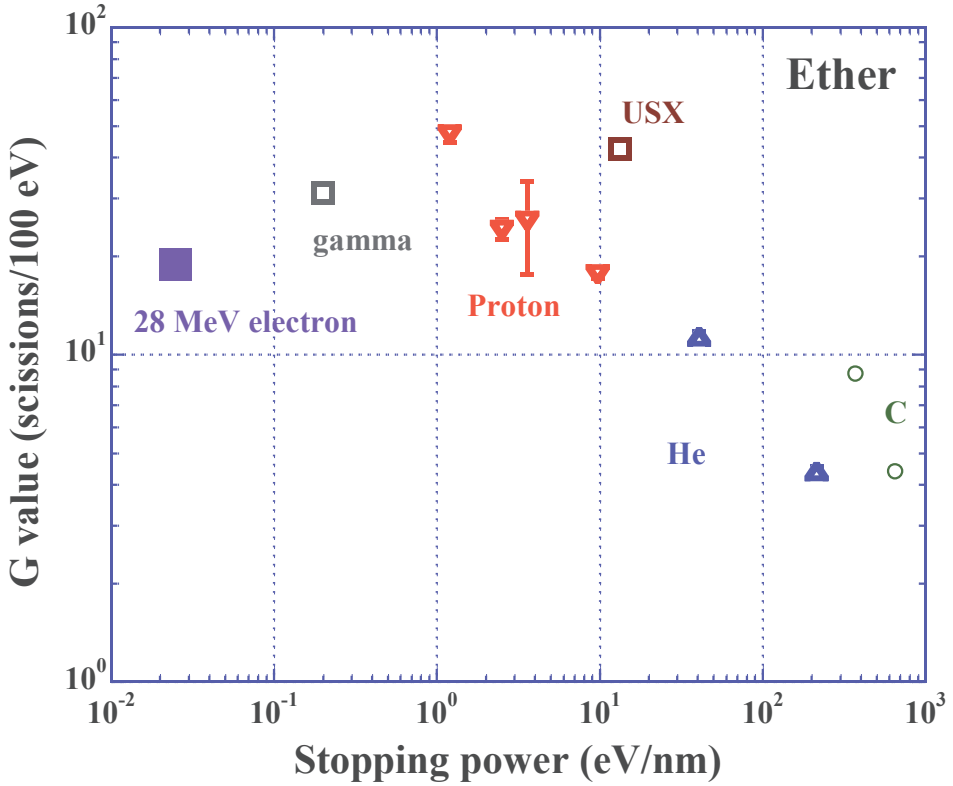

Fig. 4.2.5. G values for loss of ether against the stopping power (Kusumoto et al., 2016b). The horizontal axis of 28 MeV electron and gamma ray are applied to deposited energy per unit distance and average *LET* in water, respectively.

Figure 4.2.5. shows G value for loss of ether against the stopping power (Kusumoto et al., 2016b). The G value of 28 MeV electron is slightly lower than that of gamma ray, of

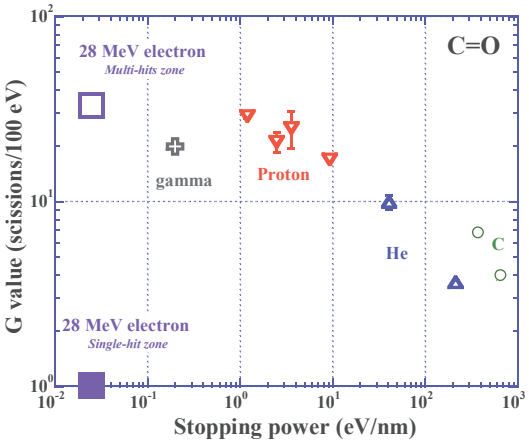

Fig. 4.2.6. G values for loss of carbonyl against the stopping power (Kusumoto et al., 2016b). The deposited energy per unit distance and average *LET* in water are adopted in the cases of 28 MeV electron and gamma ray, respectively.

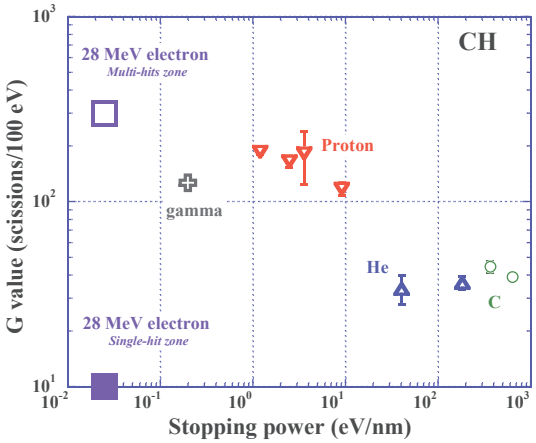

Fig. 4.2.7. G values for loss of CH groups against the stopping power (Kusumoto et al., 2016b). The deposited energy per unit distance and average *LET* in water are adopted in the cases of 28 MeV electron and gamma ray, respectively.

which average *LET* in water is 0.2 eV/nm. In addition, that of 70 MeV proton is clearly greater than that of 28 MeV electron. Lower G value of 28 MeV electron should indicate the recombination resulted in the original configuration along the trajectory was effectively occurred. Figure 4.2.6. and 4.2.7. indicate G values for losses of carbonyl and CH groups in PADC against the stopping power (Kusumoto et al., 2016b). The G values are extremely small in the Single-hit zone because the absorbance is not changed. In the Multi-hits zone, the G values are greater than the other radiations. The G values of 28 MeV electrons in the Multi-hits zone can not be simply compared to the others because the overlapping of electron tracks becomes significant.

4.3. Elucidation of the layered structure of latent track

The distinctly enhanced G values for losses of carbonyl and CH groups in PADC exposed to low *LET* radiations lead us to the elucidation of the layered structure of ion tracks in PADC. As an example, layered structure of C ion with an energy of 4.8 MeV/u is illustrated in Fig. 4.3.1. Three different regions can be observed. Around the ion trajectory, all functional sections are lost because the number density of secondary electrons is the highest among three. This implies the multi-hits of secondary electrons on a certain single repeat unit is easily occurred around the ion track. Since the number density of secondary electrons is lower than the other regions, only ether is broken at a

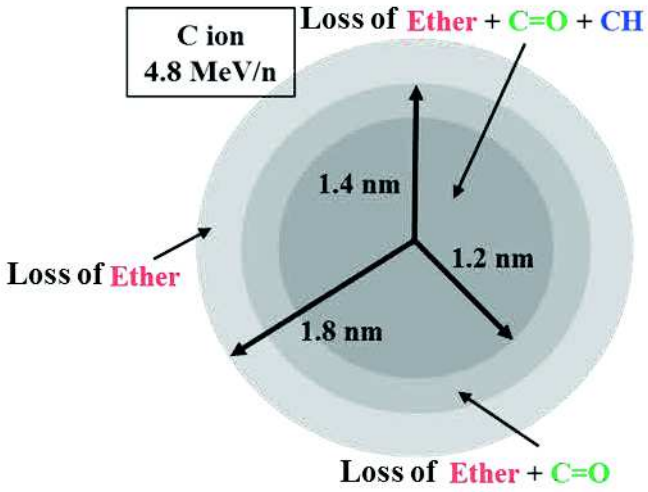

Fig. 4.3.1. Layered structure of C ion with an energy of 4.8 MeV/u.

distant position from the ion path. The author may call the region where more than two electrons passed through a single repeat unit as track core. Namely, the local dose must be greater than the critical dose inside the track core. Multi-hits of secondary electrons on a certain single repeat unit hardly occur at a distance position from the particle trajectory because the number density of secondary electrons is the lowest. The region where the local dose is lower than the critical dose may be called the track hallo. The combination of the deposited energy with the number of secondary electrons is important to elucidate the creation mechanism and the structure of latent tracks in PADC.

4.4. Estimation of the defect size of 222 nm UV photons

In this section, the author cites some important results from the research by Sakamoto et al., (2010), in which the effects of UV light with a wavelength of 222 nm on PADC were investigated. Because the photon energy of the UV light is 5.6 eV, it is impossible to produce any successive defects in PADC films, different from the previously described low *LET* radiations.

4.4.1. Quantum yields for typical functional groups in PADC

The quantum yields, the number of events caused by absorbed photons, of not only PADC but also bisphenol A carbonate, PC, and poly ethylene terephthalate, PET, under the 222 nm photon exposures were evaluated in the previous study (Sakamoto et al., 2010). The results relating to PADC is reproduced in order to estimate the size of the point-like defects after the 222 nm UV exposures.

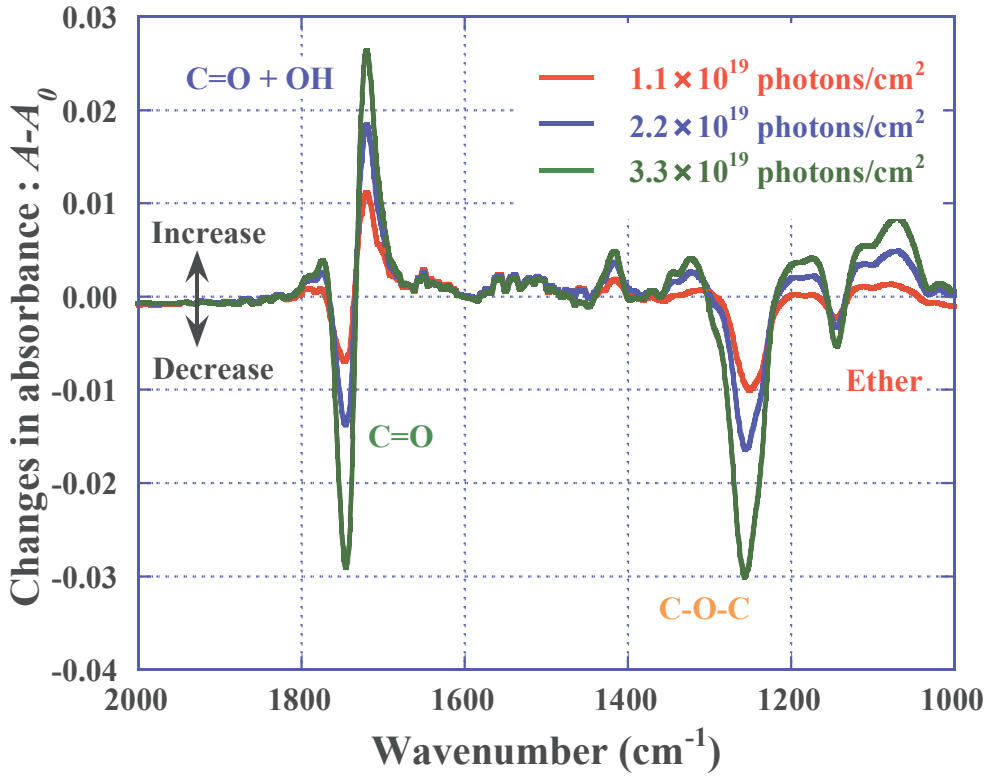

Fig. 4.4.1. Subtracted IR spectra of PADC exposed to UV photons (Sakamoto et al., 2010).

Figure 4.4.1 shows subtracted IR spectra of PADC at the indicating UV photon fluence. The ether in PADC at 1150 cm^{-1} and C-O-C, composing the carbonate ester, at 1260 cm^{-1} decrease monotonically with photon fluence absorbed in PADC. At odds with this, the peak shifts of carbonyl are observed from 1720 to 1750 cm^{-1}, which indicate the formation of hydrogen bond with generated OH groups. Fig. 4.4.2. represents the changes in absorbance of typical functional groups up to the fluence of 5.4×10^{18} photons/cm^2. In this figure, the absorbance is evaluated using the peak area, not the height in order to discuss quantitatively. Tse et al., reported the Norrish I reaction dominates the UV defects in PADC (Tse et al., 2006&2008). Their estimation is available to the present study of 222 nm UV photons. The changes in absorbance of ether, C-O-C and carbonyl decrease tonelessly with the fluence. The peak of shifted carbonyl (C=O+OH) increases with the fluence. Based on the Beer-Lambert law, the changes in absorbance is concordant with the changes in number densities of typical functional groups in PADC. This suggests that the quantum yield can be evaluated from the slope of each fitting line in Fig. 4.4.2. The obtained quantum yields are listed in Table 4.4.1. If it is assumed that an energy of 5.59 eV was deposited in PADC when one UV photon was absorbed, one can calculate the number of molecular changes when a total energy of 100 eV was absorbed from UV lights in it. The quantum yields are four orders magnitude lower than the G values of 28 MeV electron, gamma ray, protons and heavy ions (Mori et al., 2009&2010; Kusumoto et al.,

2016a&b). Since the quantum yield of shifted carbonyl (C=O+OH) is equivalent to that of original carbonyl, the carbonyl composing carbonate ester is not cleaved below the fluence of 5.4×10^{18} photons/cm^2. At odds with this, the number density of C-O-C which also composes carbonate ester decreases with increasing the photon fluence. This implies that the C-O-C is independently cleaved during the photon exposures.

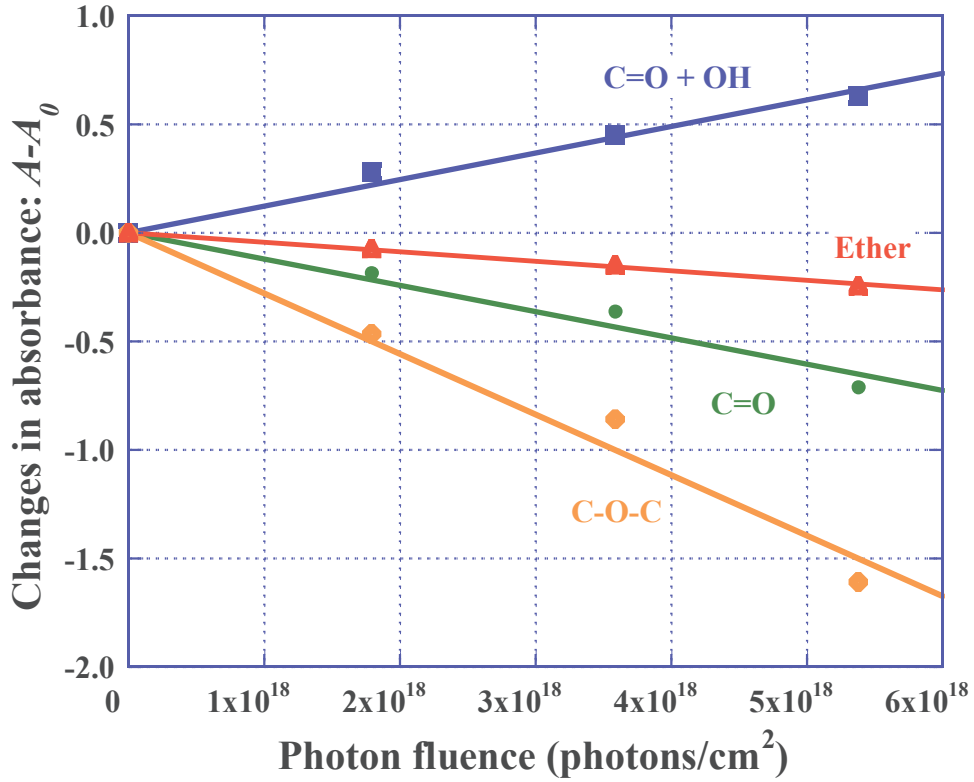

Fig. 4.4.2. Changes in absorbance under the UV irradiations up to 5.4×10^{18} photons/cm^2 (Sakamoto et al., 2010). The absorbance is evaluated using the area under each peak in subtracted spectra.

Table 4.4.1 Quantum yields for typical functional groups in PADC

Functional groups	Quantum yields
C=O + OH	2.1×10^{-3}
Ether	-8.2×10^{-3}
C-O-C	-2.5×10^{-3}
C=O original	-2.1×10^{-3}

4.4.2 Size estimation of the defect of 222 nm UV photons

Figure 4.4.3. shows the changes in absorbance of heights up to the fluence of 8.8×10^{19} photons/cm^2. The absorbance of ether and C-O-C in PADC decreases monotonically and that for shifted carbonyl increases with increasing the photon fluence.

The reduction behavior of carbonyl is slightly changed at the critical fluence. The difference between the loss of carbonyl and shifted carbonyl is regarded as the decarboxylation with releasing of CO or CO_2 gas (Figure 4.4.3). The decarboxylation is observed only above the critical fluence of 3.0×10^{19} photons/cm^2. Similar two-steps damage formation processes were observed in the cases of low *LET* radiations, such as gamma ray, USX and 28 MeV electron as described in the previous sections of 4.1. and 4.2. The losses of carbonyl in PADC irradiated with the low *LET* radiations were related to the overlapping of electron tracks. Since the defects of UV photons are isolated from each other, it can be regarded as spherical defects, rather than a cylinder. The inset sketch in Fig. 4.4.4. is a result of simulation using random number for the accumulation of the defects due to UV exposures at the critical condition in a block with a volume of $2\times2\times10$ nm^3. The author can find 38 spherical defects in the block and some overlapping. In the block, 342 radio-sensitive sections of ether and carbonate ester exist. This implies that the breaking of carbonyl begins when 10% of radio-sensitive sections are broken.

To estimate the size of defects due to UV photon exposures, the conventional track overlapping model as represented in Eq. 2.9.1 is extended as in the same form using the $v=(4/3)\pi r^3$ (in cm^3) instead of the σ (in cm^2). In the case of UV photon, the fluence ϕ

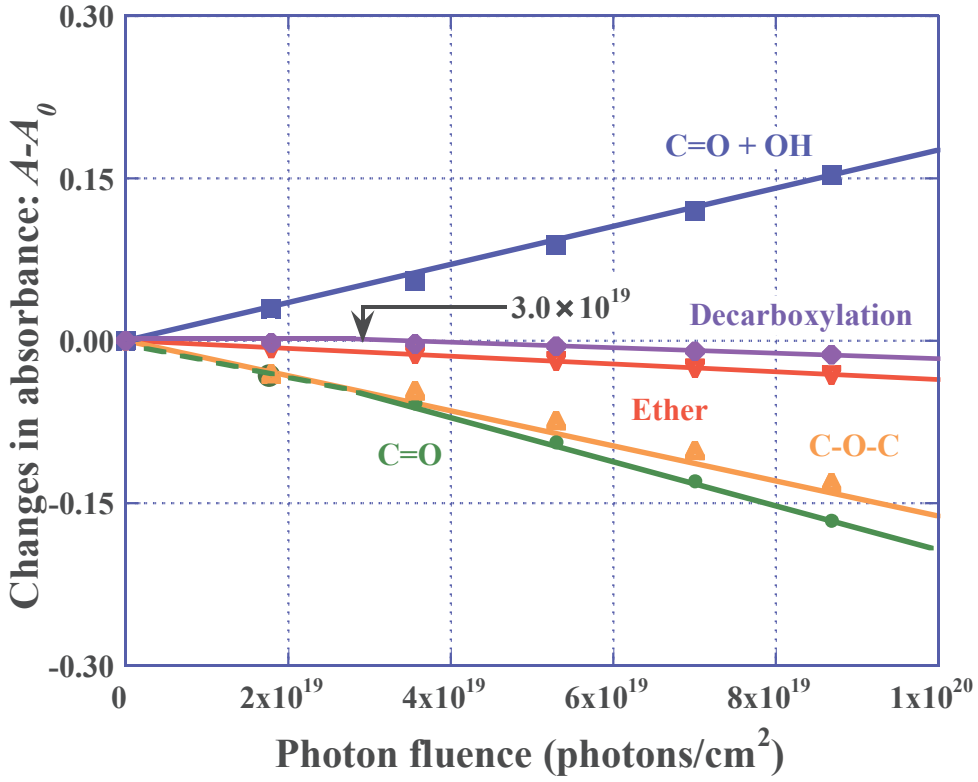

Fig. 4.4.3. Changes in absorbance under the UV irradiations up to 2.3×10^{20} photons/cm^2 (Sakamoto et al., 2010). The absorbance is the height of each peak in subtracted spectra.

must be replaced by the amount of UV defects. The amount of UV defects is 3.2×10^{17} cleavages/cm^2 at the critical condition. Based on the extended overlapping model, the size of the UV defects is estimated as 0.02 nm (Figure 4.4.4). The size of the UV defects is comparable or smaller than the Bohr radius of 0.0529 nm. This indicates that the carbonyl in PADC starts to decrease after the formation of high density damage of ether and/or C-O-C in carbonate ester. This feature has never been observed for low *LET* radiations.

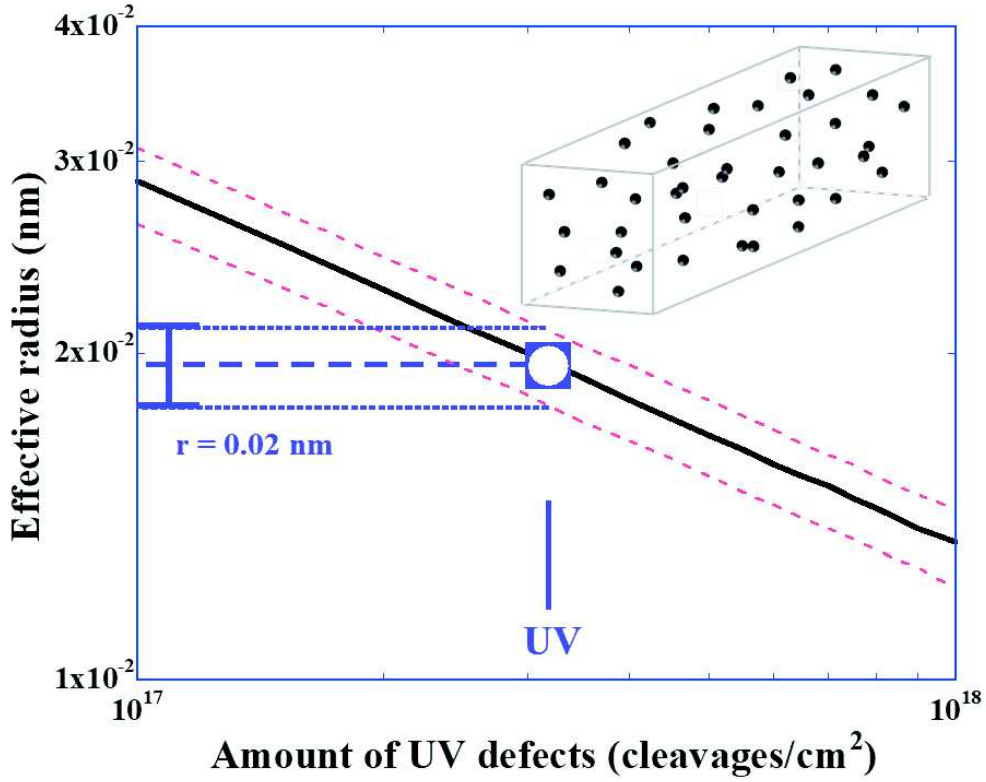

Fig. 4.4.4. The relation between the critical fluence of the photon and the effective radius of the UV damage. Inset is an example of the accumulated UV defects in the volume of $2\times2\times10$ nm^3 at the critical condition.

4.5. Summary for the low LET radiations and 222 nm UV photon irradiations

The chemical damage structures in PADC irradiated with the low *LET* radiations and UV photons with a wavelength of 222 nm were investigated using FT-IR spectrometry. The relative absorbance of ether in PADC exposed to gamma ray decreased linearly with the absorbed dose. At odds with this, that of carbonyl decreased above the critical dose of 60 kGy. Similar results were also obtained in the cases of USX and 28 MeV electron exposures. These critical doses were concordant with that of gamma ray, judging from the experimental error. It was apparent that the loss of carbonyl was caused by two-steps damage formation process, which is related to the overlapping of electron

tracks.

In order to verify the two steps damage formation process due to 28 MeV electron irradiations, the previously developed track overlapping model was used. Unfortunately, the track overlapping model could not be applied to the gamma ray and USX because of the random motion of low energy electrons. Based on the track overlapping model, the effective radius of 28 MeV electron was estimated as 0.05 nm, that is so close to that for loss of ether obtained by FT-IR spectroscopy. This implies the carbonyl was broken when adjacent ether was lost. The present view was supported by the sudden decrease of generation rate of OH groups at the critical fluence.

The quantum yields of typical functional groups in PADC exposed to 222 nm UV photons were evaluated. The values were four order magnitude lower than the G values of ionizing radiations. The changes in absorbance of ether and C-O-C composing the carbonate ester decreased monotonically with the fluence. Above the critical fluence of 3.0×10^{19} photons/cm^2, the carbonyl turned out to decrease. The decarboxylation process releasing CO or CO_2 gas was also observed above the critical fluence. The track overlapping model was extended to estimate the size of point-like defects due to UV exposures regarding the critical fluence of 3.0×10^{19} photons/cm^2. The defects were regarded as the sphere with a certain radius. The size of UV defects was assessed as 0.02 nm. The small defects implied that continues damages are never produced during the photon exposures.

Les structures de dommages chimiques dans le PADC irradié avec des radiations à faible *TLE* et des photons UV de longueur d'onde de 222 nm ont été étudiées par spectroscopie FTIR. L'absorbance relative des fonctions éther exposés aux rayons gamma diminue linéairement avec la dose absorbée. En contradiction avec ce point, celle des fonctions carbonyle diminue au-dessus d'une dose critique de 60 kGy. Des résultats similaires ont également été obtenus dans les cas d'exposition aux électrons. Il est ainsi démontré que la perte des fonctions carbonyle est provoquée par un processus de formation en deux étapes, lié au chevauchement des traces d'électrons.

Afin de vérifier ce processus de formation des dommages en deux étapes, le modèle de chevauchement de traces précédemment développé a été utilisé. Sur la base de ce modèle un rayon effectif pour un électron de 28 MeV a été estimé à 0,05 nm, valeur très proche de celle obtenue expérimentalement pour la perte des fonctions éther. Ceci implique que le carbonyle disparait lorsque l'éther adjacent a été également perdu.

Les rendements quantiques de groupes fonctionnels du PADC exposés à des photons UV de 222 nm ont été mesurés. Les valeurs sont inférieures de quatre ordres de

grandeurs aux valeurs G des rayonnements ionisants. Les changements d'absorbance de l'éther et du C-O-C de l'ester de carbonate diminuent de façon monotone avec la fluence. L'absorbance des carbonyle diminue seulement au-dessus de la fluence critique de $3{,}0\times10^{19}$ photons/cm^2. Le processus de décarboxylation libérant du CO et/ou du CO_2 a également été observé au-dessus de la fluence critique. Le modèle de chevauchement des traces a été étendu pour estimer la taille des défauts ponctuels dus aux expositions aux UV. La forme des défauts est considérée sphérique. La taille des défauts UV a été évaluée à 0,02 nm.

Chapter 5
Radiation chemical yields for high energy protons below the detection threshold

The latent track structure produced by high energy protons whose deposited energies are clearly lower than the detection threshold is now investigated to understand the difference in the modified structure between etchable tracks and un-etchable tracks. Obtained results are compared to the previously obtained ones of a lower energy proton and heavy ions. In this chapter, the solid square symbols in the graphs indicate the present results for high energy protons (Kusumoto et al., 2016a) and the open symbols show those from the previous ones (Mori et al., 2011&2009; Kusumoto et al., 2015).

La structure de la trace latente produite par des protons pour des énergies déposés nettement inférieurs au seuil de détection du PADC est maintenant étudiée pour comprendre la différence de structure entre des traces révélables et des traces non-révélables. Les résultats obtenus sont comparés à ceux obtenus précédemment pour des protons d'énergie inférieure et des ions lourds. Dans ce chapitre, les symboles en carrés pleins dans les graphiques indiquent les résultats actuels pour les protons de haute énergie (Kusumoto et al., 2016a) et les symboles ouverts montrent ceux de précédentes études (Mori et al., 2011 & 2009; Kusumoto et al. 2015)

5.1. Scissions of ether and carbonyl

Figure 5.1.1 shows IR spectra before and after irradiation with 70 MeV protons with a fluence of 7.1×10^{13} ions/cm^2. After the irradiation, the heights of the absorbance of typical functional groups in PADC decrease. Figure 5.1.2 shows the reduction trends of the relative absorbance (A/A_0) of ether, carbonyl, C-O-C and CH groups against the fluence of 70 MeV protons (Kusumoto et al., 2016a). Monotonic decrease of the relative absorbance for ether, carbonyl and CH groups in PADC has been observed. It is concordant with the trends of 5.7, 20 and 30 MeV protons and heavy ions (Mori et al., 2009; Kusumoto et al., 2016a). From the dependence of absorbance to the fluence, removal cross sections for each track, σ, (in cm^2) can be assessed using Eq. (4.2.1). The linearity of the relative absorbance is kept up to 7.5×10^{13} ions/cm^2. This means the overlapping of proton tracks are negligible. Above the examined fluence, the linearity may be lost by the overlapping of proton tracks. The derived removal cross sections of ether, carbonyl and CH groups for high energy protons are listed in Table 5.1.1 with

statistical deviation.

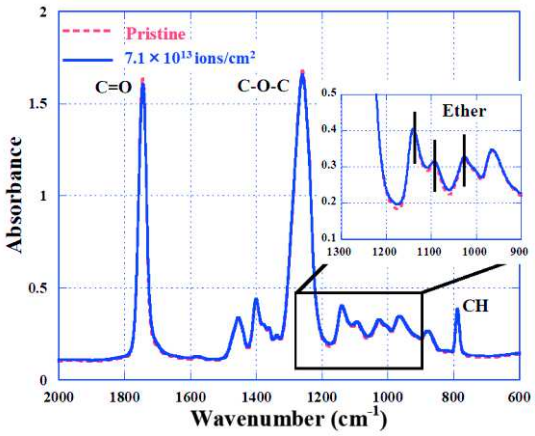

Figure 5.1.1. IR spectra before and after the exposure to 70 MeV proton with a fluence of 7.1×10^{13} ions/cm^2.

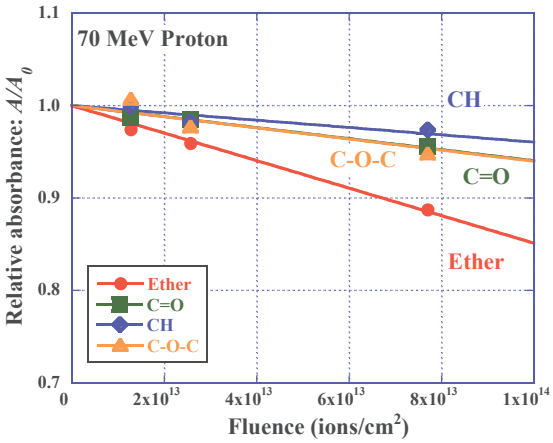

Figure 5.1.2. Relative absorbance of ether, carbonyl and CH groups in PADC irradiated with 70 MeV proton as a function of the fluence (Kusumoto et al., 2016a). The slope of each fitted line corresponds to the removal cross sections.

Table 5.1.1. Removal cross sections of ether, carbonyl and CH groups for high energy protons.

Energy (MeV)	20	30	70
σ_{Ether} (cm^2)	$(3.2\pm1.0)\times10^{-15}$	$(2.1\pm0.2)\times10^{-15}$	$(1.9\pm0.1)\times10^{-15}$
$\sigma_{C=O}$ (cm^2)	$(1.6\pm0.4)\times10^{-15}$	$(0.9\pm0.3)\times10^{-15}$	$(0.6\pm0.1)\times10^{-15}$
σ_{CH} (cm^2)	$(1.5\pm0.9)\times10^{-15}$	$(0.8\pm0.3)\times10^{-15}$	$(0.4\pm0.1)\times10^{-15}$

Figures 5.1.3 and 5.1.4 represent the damage densities defined by losses of ether and carbonyl per unit distance along proton tracks in PADC as a function of the stopping power, respectively (Kusumoto et al., 2016b). Overall, the damage densities increase monotonically with the stopping power. In details, there is a bending point at the stopping power of 800 eV/nm. The author defines the region below the 800 eV/nm as the "first region". It contains protons, He and C ions and the result displays an identical trend to the 5.7 MeV proton, He and C ions. The trends of the damage densities in the first region can be then expressed as a function of the stopping power (in eV/nm) using the least square fitting as,

$L_{ether}=0.39(-dE/dx)^{0.67}$ and (5.1.1)

$L_{C=O}=0.32(-dE/dx)^{0.68}$ (5.1.2)

For the "second region" located beyond the bending point at the stopping power of 800 eV/nm, the trends of the damage density are written as,

$L_{ether}=0.01(-dE/dx)^{1.22}$ and (5.1.3)

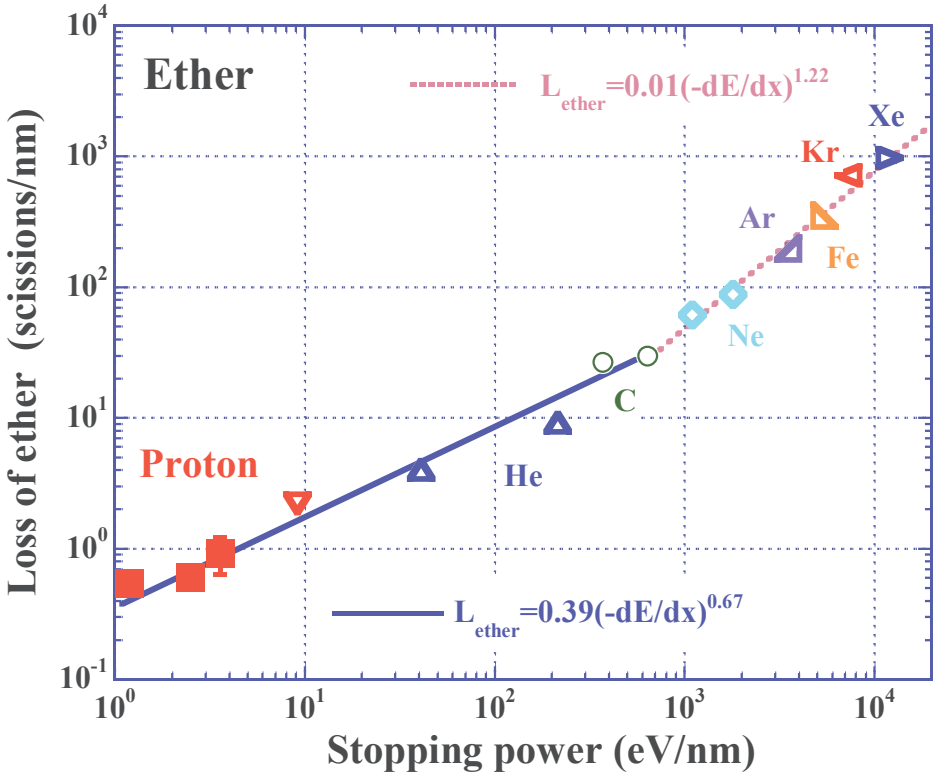

Fig. 5.1.3. Damage density for loss of ether in PADC as a function of the stopping power. Solid symbols indicate the present results (Kusumoto et al., 2016a) and open symbols indicate previous ones (Mori et al., 2011&2012).

$$L_{C=O}=0.01(-dE/dx)^{1.25} \quad (5.1.4)$$

The trend of damage density for loss of C-O-C which composes the carbonate ester is identical to that of carbonyl in both regions.

Figures 5.1.5. and 5.1.6. show the effective track core radius for loss of ether and carbonyl as a function of the stopping power, respectively. To summarize, the effective track core radius increases monotonically with the stopping power. There is also an inflection points at the stopping power of 800 eV/nm, that is observed in the damage density (Figs. 5.1.2. and 5.1.3.). The effective track core radius for high energy protons is also located on the extrapolated lines of the trends of 5.7 MeV proton and He and C ions. The size of the effective track core radius shows that the scissions induced by the high energy protons occur within a single repeat unit consequently. The author has focused on the effective track core radius of ether at the bending point where the effective track core radius is about 2 nm, which is equivalent to the length of repeat unit of PADC. It implies that the core size expands easily when the damages cover more than two repeat units. This may be related to the changes of the trends in the second region.

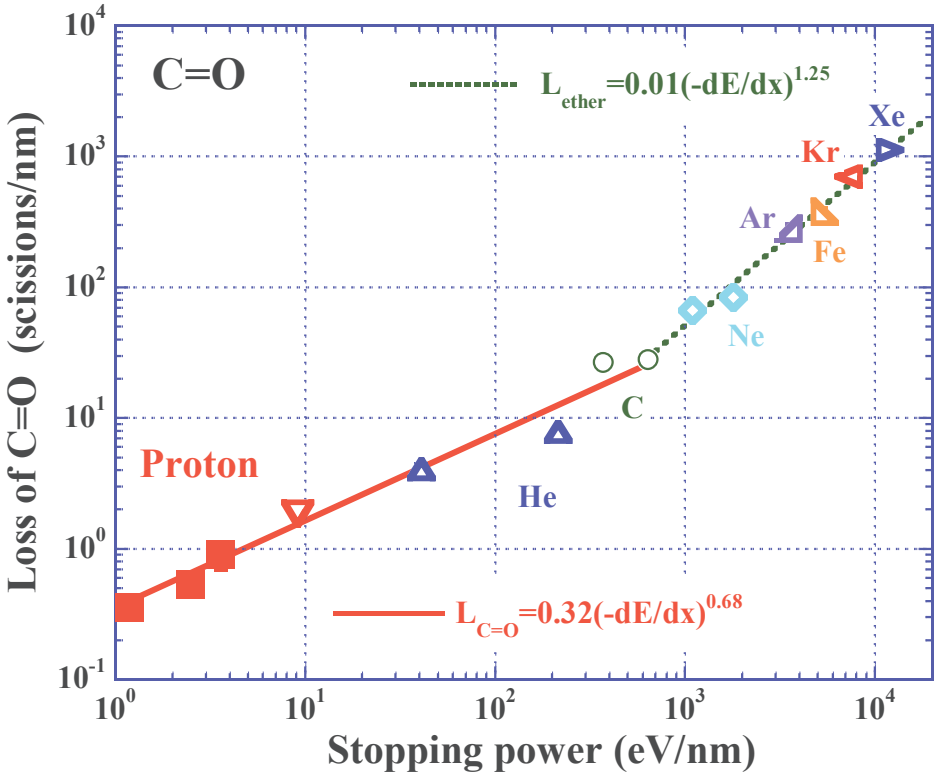

Fig. 5.1.4. Damage density for loss of carbonyl in PADC as a function of the stopping power. Solid symbols indicate the present results (Kusumoto et al., 2016a) and open symbols indicate previous ones (Mori et al., 2011&2012).

The fitted lines for the effective track core radius are also attained as,

$r_{ether}=0.19(-dE/dx)^{0.35}$ and (5.1.5)

$r_{C=O}=0.14(-dE/dx)^{0.35}$ (5.1.6)

for the first region and as,

$r_{ether}=0.04(-dE/dx)^{0.59}$ and (5.1.7)

$r_{C=O}=0.03(-dE/dx)^{0.60}$ (5.1.8)

for the second region. These formulas have been improved from those found in a previous study (Mori et al., 2011) by adding the experimental data of 0.6 MeV/u He ion and 4.1 MeV/u Ne ion.

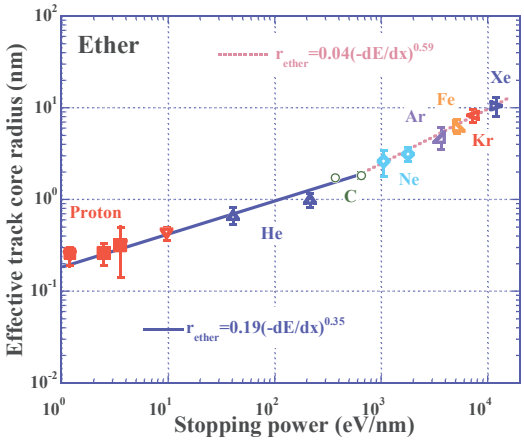

Fig. 5.1.5. Effective track core radius for loss of ether in PADC as a function of the stopping power. Solid symbols indicate the present results (Kusumoto et al., 2016a) and open symbols indicate previous ones (Mori et al., 2011&2012).

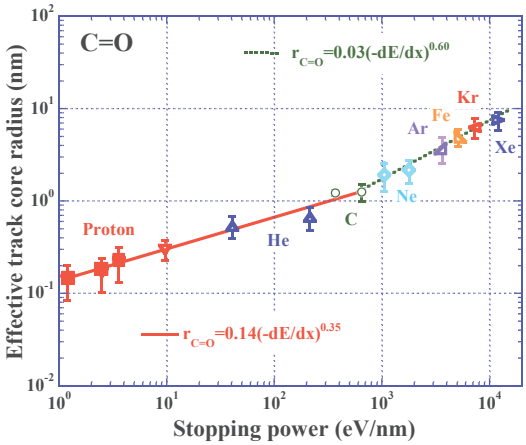

Fig. 5.1.6. Effective track core radius for loss of carbonyl in PADC as a function of the stopping power. Solid symbols indicate the present results (Kusumoto et al., 2016a) and open symbols indicate previous ones (Mori et al., 2011&2012).

5.2. Scissions of CH groups

The effective track core radius and damage density for CH groups are shown in Figs. 5.2.1 and 5.2.2 (Kusumoto et al., 2016a). In the case of CH groups, the trends of the damage density and the effective track core radius are completely different from those of ether and carbonyl. The trends are not changed at the stopping power of 800 eV/nm. However, the plateau region is found including 5.5 MeV/u He ion (37 eV/nm) and 5.7 MeV proton (9.3 eV/nm). The detection thresholds for proton and He ion of PADC as an ETD, which are the stopping powers of 17 and 37 eV/nm, respectively are shown as arrows in Fig. 5.2.1&5.2.2 (Hassan et al., 2013; Kusumoto et al., 2017b). The detection threshold of C ion of 55 eV/nm is almost upper end of the plateau. Additional experiments are necessary to determine the chemical damage parameters at the detection threshold of C ions including the detection threshold. The effective track core radius at plateau region is 0.3 nm. This suggests that the damages of high energy protons have occurred within a single repeat unit. Only the CH groups which belong to the radio-sensitive part are lost due to the proton irradiations below the detection threshold (See Fig. 2.1.1). In other words, etch pits are formed when at least two radio-sensitive parts are lost.

The trends of the damage density and the core radius for high energy protons, above the 5.7 MeV proton are derived using least square fitting as,

$L_{CH}=1.78(-dE/dx)^{1.08}$ and (5.2.1)

$r_{CH}=0.11(-dE/dx)^{0.47}$ (5.2.2)

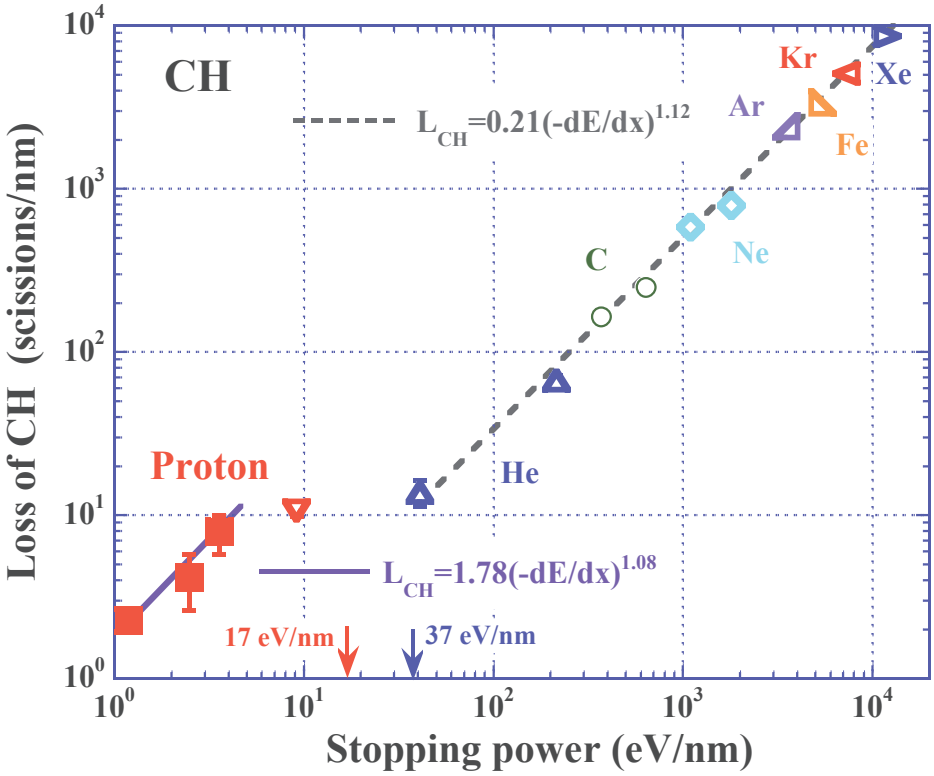

Fig. 5.2.1. Damage density for loss of CH groups in PADC as a function of the stopping power. Solid symbols indicate the present results (Kusumoto et al., 2016a) and open symbols indicate previous ones (Kusumoto et al., 2015).

The trends of the damage density and the effective track core radius for heavy ions are attained respectively as,

$L_{CH}=0.21(-dE/dx)^{1.12}$ and (5.2.3)

$r_{CH}=0.03(-dE/dx)^{0.59}$ (5.2.4)

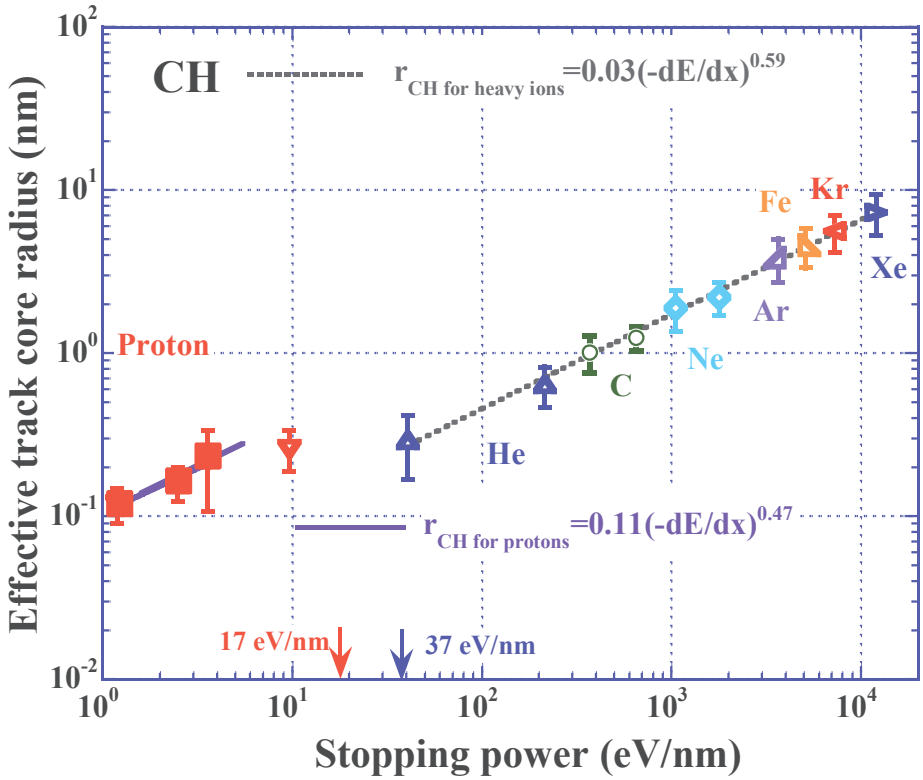

Fig. 5.2.2. Effective track core radius for loss of CH groups in PADC as a function of the stopping power. Solid symbols indicate the present results (Kusumoto et al., 2016a) and open symbols indicate previous ones (Kusumoto et al., 2015).

5.3. Radiation chemical yields for losses of typical functional groups in PADC

The G values for losses of ether and carbonyl in PADC exposed to high energy protons are indicated in Fig. 5.3.1 and 5.3.2 (Kusumoto et al., 2016a&2017a). The inverse relation of G values for losses of ether and carbonyl in PADC to the stopping power is confirmed in the first region. The G values of previous results of 5.7 MeV proton and He ions are located on the extrapolated line that has been derived from the present results of high energy protons, showing agreement between the experiments. In the second region, the G values increase with the increase of the stopping power. The trends are related to that of damage densities and/or effective track core radius in the second region, where the size of the effective track core radius expand easily when track size covers more than two repeat unit. Paying attention to the high energy protons, the G values decrease with increasing the stopping power. Furthermore, the G value for 70 MeV proton is greater than those for gamma ray from the Co-60, which are plotted on 0.2 eV/nm as the lateral axis adopting the average linear transfer, *LET*, in water. This confirms that the relatively dense damages along the proton tracks suppress the recombination resulting in original

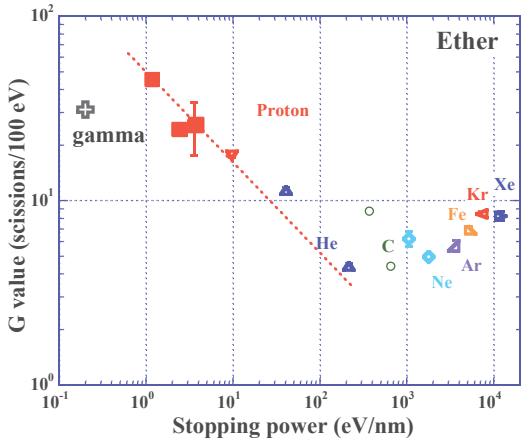

Fig. 5.3.1. G value for loss of ether in PADC against the stopping power. Solid symbols indicate the present results of high energy protons (Kusumoto et al., 2016a) and open symbols indicate the previous ones of low energy proton and heavy ions (Mori et al., 2011&2012) and of gamma ray in chapter 4 (Kusumoto et al., 2017a).

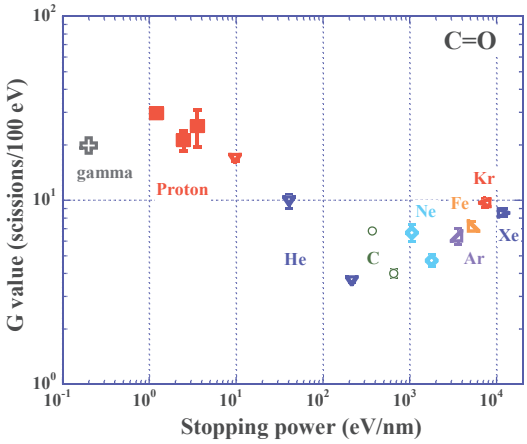

Fig. 5.3.2. G value for loss of carbonyl in PADC against the stopping power. Solid symbols indicate the present results of high energy protons (Kusumoto et al., 2016a) and open symbols indicate the previous results of low energy proton and heavy ions (Mori et al., 2011&2012) and of gamma ray in chapter 4 (Kusumoto et al., 2017a).

configuration. The G values for C, Fe and Xe ions with energies of higher than 100 MeV/u were also higher than that for gamma ray (Mori et al., 2012&2014). This also supports the previous interpretation.

Figure 5.3.3 shows the G value for loss of CH groups against the stopping power (Kusumoto et al., 2016a). The G values for loss of CH groups for high energy protons in PADC do not depend on the stopping power. In addition to this, the distinct step of the G value is observed between protons and heavy ions. Below the detection threshold, chemical damages are formed within a single repeat unit of PADC. In such cases, methylene groups between radio-sensitive sections are released away resulted from the scission of ether and carbonate esters. Therefore, the higher G values are observed below the detection threshold. In other word, at least two radio-sensitive sections must be lost to generate the etch pits. The changes in the latent track structure around the detection threshold can be clearly elucidated by focusing on the reduction behavior of the number density of CH groups after the irradiation.

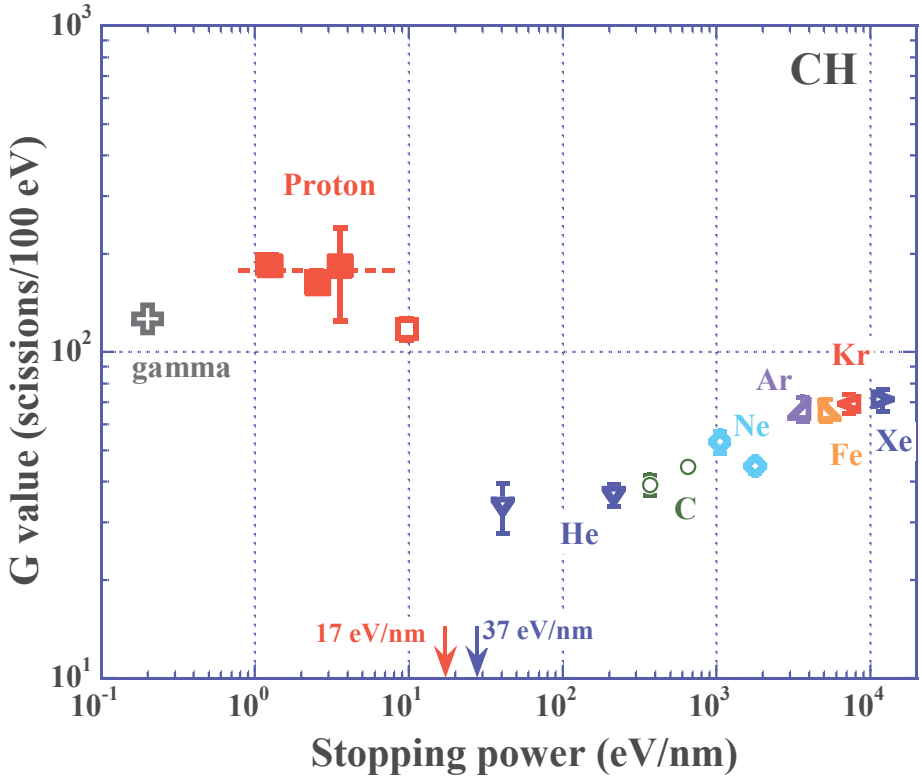

Fig. 5.3.3.G value for loss of CH groups in PADC against the stopping power. Solid symbols indicate the present results (Kusumoto et al., 2016a) and open symbols indicate the previous results (Kusumoto et al., 2015).

5.4. Radial dose distributions around the detection threshold.

Based on the radial dose distribution model, the local dose around the proton tracks with energies of 2.6, 5.7, 20, 30 and 70 MeV in PADC is calculated as shown in Fig. 5.4.1 (Waligórski et al., 1986). The averaged ionization potential is treated as a valuable in order to keep the total energy deposition per unit distance along proton tracks to reproduce concordant results with the stopping powers calculated by the SRIM code. The parameters are determined between 65 and 120 eV depending on the proton energy. The plotted points on each curve are the effective track core radius for loss of ether which are experimentally derived. The secondary electrons produced by 2.6 MeV proton spreads up to 1 μm from the ion trajectory. In comparison to this, the effect of the secondary electrons produced by 70 MeV protons reaches 100 μm from the ion trajectory. The other energy curves distributes in between (Figure 5.4.1). The fractions of deposited energy within the effective track core radius are 7.0, 5.4, 5.0, 3.5 and 4.0% for 2.7, 5.7, 20, 30 and 70 MeV protons, respectively. The scissions of polymeric chains of PADC should occur effectively not only in the track core but also in the track hallo or penumbra region

from the result of the higher G value for gamma ray. Since the structure of PADC is never uniform on a scale of less than 1 nm, the concept of the radial dose distribution model cannot be simply applied to such a small volume. A new physical concept is mandatory for explaining the latent track structure in polymers because it is difficult to have more detail discussions based on the radial dose distribution model, as well as other physical parameters.

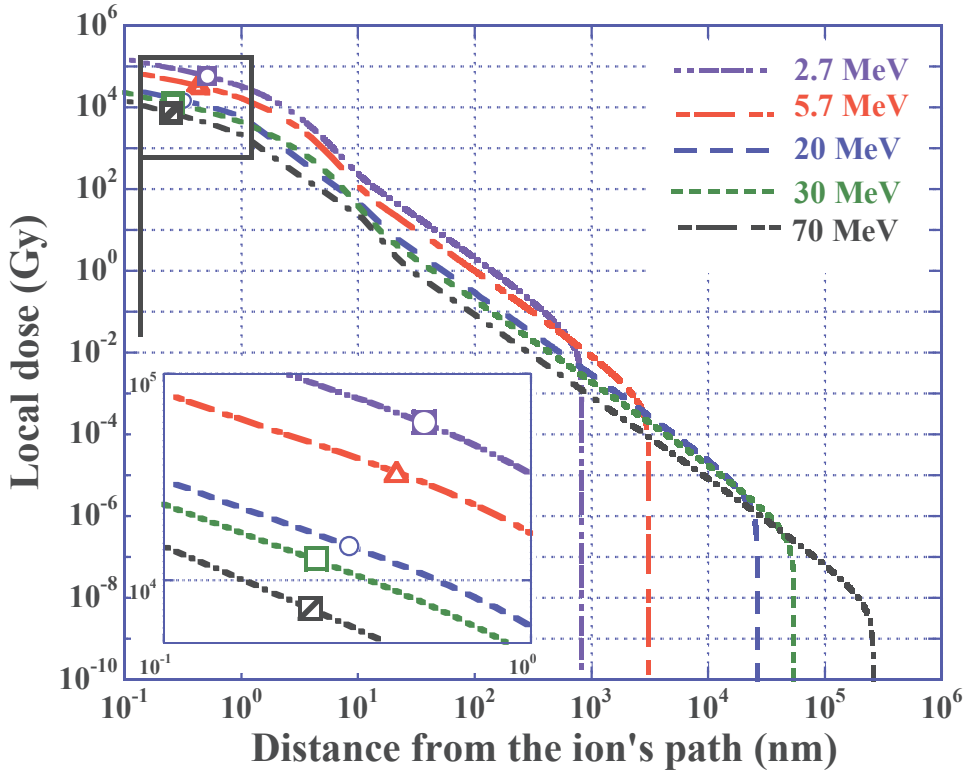

Fig. 5.4.1. Radial dose distribution around the proton tracks in PADC with energies of 2.7, 5.7, 20, 30 and 70 MeV. The plots show the experimentally obtained effective track core radius for ether.

5.5. Summary for the latent track structure of high energy protons

FT-IR spectrometric studies have been conducted to investigate the latent track structures in PADC exposed to protons with energies of 20, 30 and 70 MeV, of which deposited energies are lower than the detection threshold. The obtained results were compared to the previously obtained results of 5.7 MeV proton and heavy ions. The dependence of the effective track core radius on the stopping power is summarized in Fig. 5.5.1 (Kusumoto et al., 2016a) using the experimentally obtained formulas in previous chapters. The core radius for loss of ether has always been the biggest among the three. This confirms that the ether is the most radio sensitive sections of PADC. There were

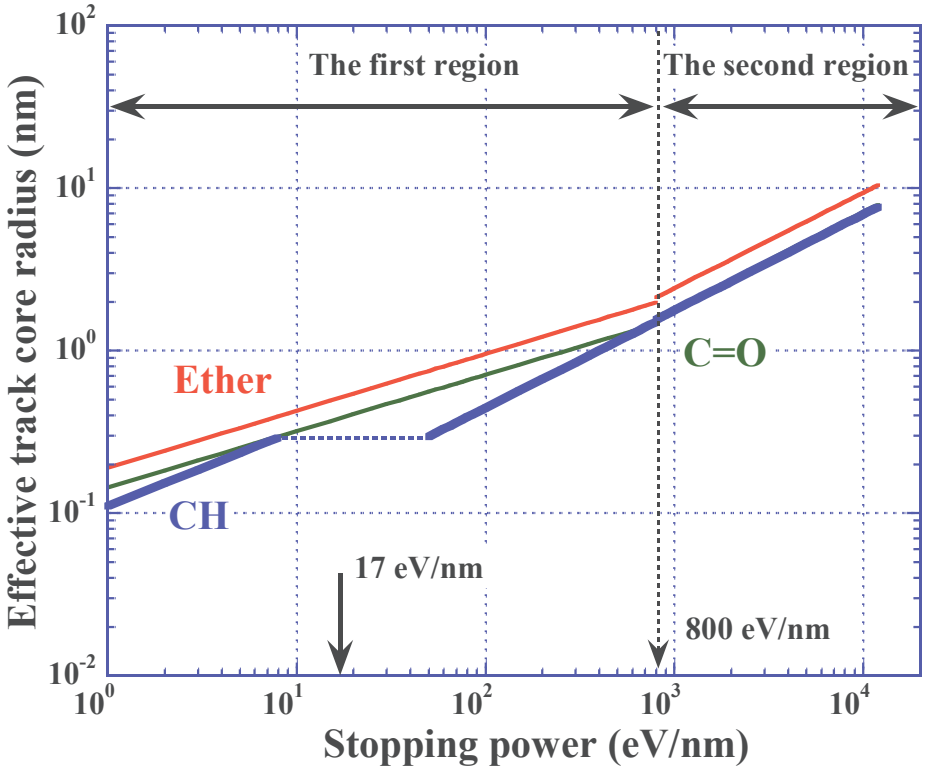

Fig. 5.5.1. Effective track core radius for losses of ether, carbonyl and CH groups in PADC against the stopping power (Kusumoto et al., 2016a). There are three regions for the modified track structure in PADC irradiated with protons and heavy ions.

bending points for both fitted lines of ether and carbonyl at the stopping power of 800 eV/nm. The corresponding track core radius for ether was about 2 nm, which was equivalent to the length of repeat unit of PADC. This implies that the track size easily expands when the damage covers more than two repeat unit. The plateau region was observed on the core radius for CH groups around the detection threshold of proton where the stopping power was 17 eV/nm. The core radius at 17 eV/nm was 0.8, 0.4 and 0.3 nm for ether, carbonyl and CH groups, respectively. This implies that the bond breakings were limited within single repeat unit below the detection threshold. In other word, etch pits are formed when track size reaches neighboring repeat unit.

The destruction of the ether is observed under the exposures of gamma ray. However, judging from the high G values for loss of ether and carbonyl in PADC irradiated with 70 MeV proton, relatively dense damages along proton tracks were effective to break chemical bonds in PADC compared to uniform damages produced by gamma ray. It is difficult to have a detail discussion based on radial dose distribution model but polymeric chains of PADC were effectively destroyed not only at inside the track core but also at a distance position from a track center.

Des études spectrométriques FTIR ont permis d'étudier les structures des traces latentes dans le PADC de protons d'énergies de 20, 30 et 70 MeV, avec des énergies déposées inférieures au seuil de détection. La dépendance du rayon effectif du coeur de la trace en fonction du *TLE* est résumée figure 5.5.1 (Kusumoto et al., 2016a). Le rayon pour la perte de l'éther est toujours le plus grand. Ceci confirme que l'éther est la partie la plus sensible aux radiations du PADC. Des points de flexion pour les deux fonctions éther et carbonyle sont observés pour un *TLE* de 800 eV / nm. Le rayon correspondant à l'éther est d'environ 2 nm, ce qui est équivalent à la longueur de l'unité répétée du PADC. Un plateau a été observée pour le rayon correspondant aux groupes CH autour du seuil de détection du proton de 17 eV / nm. Le rayon à 17 eV / nm est respectivement de 0,8, 0,4 et 0,3 nm pour les groupes éther, carbonyle et CH. Ceci implique que les ruptures de liaison sont limitées à une seule unité de répétition en dessous du seuil de détection. En d'autres termes, la révélation chimique d'une trace devient possible lorsque la dimension du cœur atteint l'unité de répétition voisine.

Chapter 6
Physical criterions for the detection threshold

In this chapter, a new physical concept of Radial Electron Fluence around Ion Tracks, *REFIT*, is proposed to describe the detection threshold of PADC and the first calculations are made using Geant4-DNA Monte Carlo simulation toolkit. Future issues of the new physical concept are discussed to make it acceptable for a universal parameter. In addition, the track core size is estimated using the conventional radial dose distribution theory. The obtained results are compared to the experimental results.

Dans ce chapitre, un nouveau concept physique de fluence électronique radiale autour d'une trace d'ion, *REFIT*, est proposé pour définir le seuil de détection du PADC. Les calculs sont effectués à l'aide du code de simulation Monte-Carlo Geant4-DNA. De plus, les dimensions du cœur de la trace sont estimées à l'aide de la théorie de la dose radiale. Les résultats obtenus sont comparés aux résultats expérimentaux.

6.1. Radial Electron Fluence around Ion Tracks for the detection threshold

Based on the experimental results, a new physical parameter for the detection threshold of PADC is proposed. In the field of radiation measurements, the definition of fluence is given as the number of particles incident on a sphere divided by the cross-sectional area of the sphere. From the general view, the secondary electron tracks are symmetrically spread in the radial direction. It is natural that the Radial Electron Fluence around Ion Tracks is defined as the number of electrons which pass through the surface of a cylinder of certain radius that is co-axial with the ion trajectory.

6.1.1. Detection thresholds of PADC

Figure 6.1.1. shows track response data for protons, He and C ions as a function of the stopping power (Hassan et al., 2013; Kusumoto et a., 2017). The author defines the detection threshold for etch pit formation of PADC as the original point where the evolution of etch pits begin along the latent track, when the chemical etching is progressing from the front surface each ion entered. The three arrows in Fig. 6.1.1. indicate the detection thresholds for proton, He and C ions. The detection thresholds are also listed in Table 6.1.1 (Hassan et al., 2013; Kusumoto et al., 2017). At the same stopping power, the sensitivity of He ions is greater than that of C ions. Furthermore, the

detection thresholds increase with the nuclear charge of ions. These imply that the stopping power is not the suitable parameter to express the sensitivity and the detection threshold. As mentioned in chapter 1, a lot of discussions have been held in 1960s. However, the universal parameter which can express the sensitivity and the detection threshold of ETDs has not been found. In the following section, the author proposes a new physical parameter for the detection threshold of PADC.

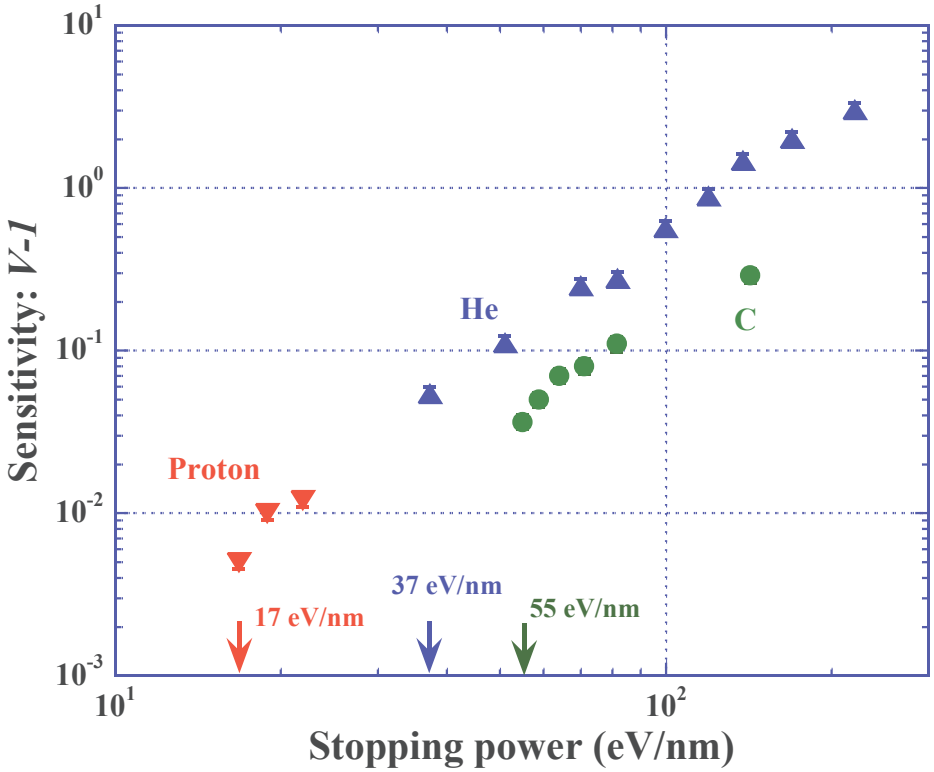

Fig. 6.1.1. Track response data for protons, He and C ions irradiated in ambient air as a function of the stopping power.

Table 6.1.1. The detection thresholds of PADC for each ion.

Ion	Energy (MeV/u)	Normalized speed: β	Detection threshold (eV/nm)
Proton	2.6	0.074	17
He	5.6	0.11	37
C	51	0.31	55

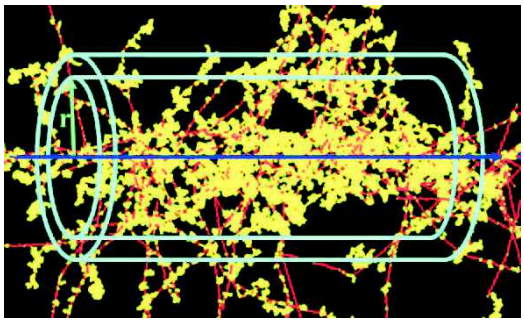

Fig. 6.1.2. A single C ion track with an energy of 46 MeV/u in the virtual stopping media: the blue arrow is the C ion track, the red lines are secondary electrons and yellows are interaction points.

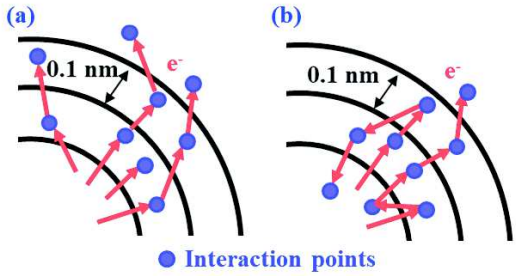

Fig. 6.1.3. Schematic views of electrons crossing borders without back scattering (a) and with back scattering (b). The purple points are interaction points and the red arrows are trajectory of secondary ions.

6.1.2. Radial Electron Fluence around Ion Tracks at the detection thresholds

Based on the experimental results using the low *LET* radiations, number of electrons which passes through a single repeat unit of PADC plays an important role to create irreversible damages on the carbonate ester (see chapter 4). In addition to this, it was also confirmed that at least two radio-sensitive sections must be lost in the radial direction to form etchable tracks (see chapter 5). Figure 6.1.2. shows the track structure of a single C ion trajectory with an energy of 46 MeV/u in the virtual stopping media. The path of C ion is illustrated by the arrow in blue. The secondary electron trajectories are indicated as the lines in red. Also, the yellow points show the interaction points. Each secondary electron starts from each original point on the ion trajectory and reaches to the terminal after its travel with a certain distance, producing the other multi electrons. As a result, the number density of secondary electrons will decrease with increasing the distance from the ion trajectory. From the general view, the secondary electron tracks are cylindrically symmetric along the ion trajectory. In the field of radiation measurement, fluence, Φ, is defined as the quotient of the number of particles, dN, incident on a sphere by it's a cross-sectional area of da ($\Phi=dN/da$). Using a sphere, the area which is perpendicular to the direction of each particle is accounted for so that all particles passing through this volume of space are included. Return to the present case of ion tracks, it is natural to count the number of electrons that pass through the surface of cylinder of certain radius. In the followings, a definition will be given on the Radial Electron Fluence around Ion Tracks, *REFIT*,.

As a first attempt, *REFIT* is proposed to universally express the detection thresholds of PADC for each ion. The *REFIT* is defined as number density of secondary

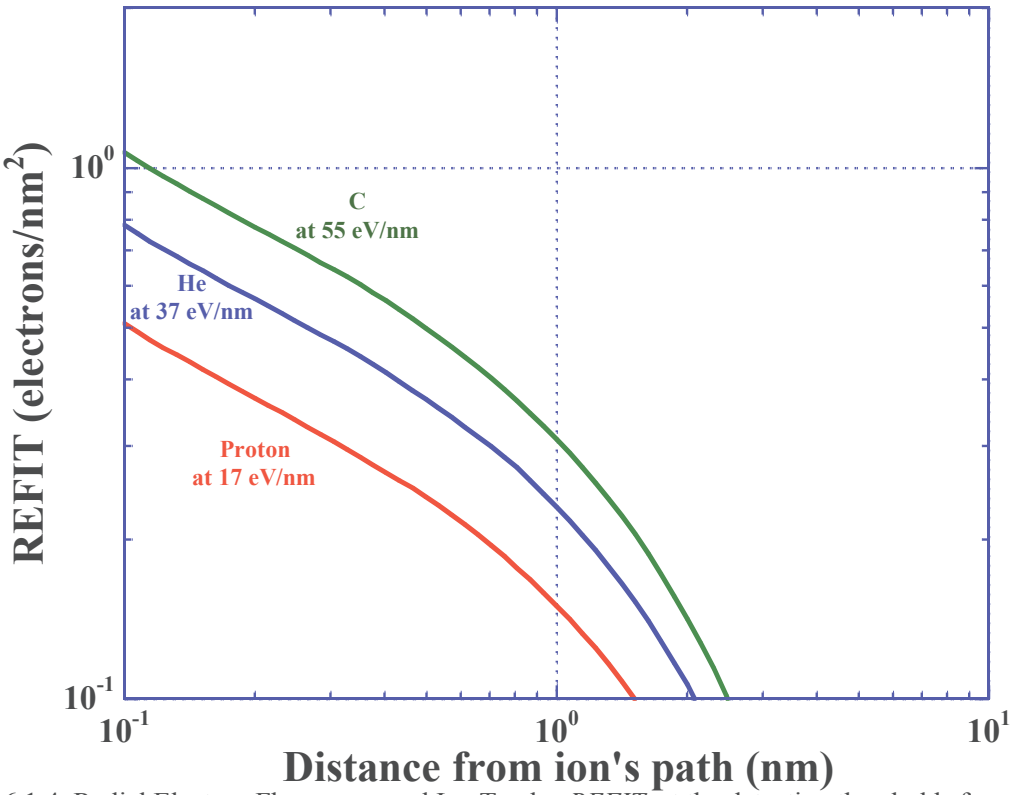

Fig. 6.1.4. Radial Electron Fluence around Ion Tracks, *REFIT*, at the detection thresholds for each ion.

electrons that pass through the surface of cylinder of certain radius that is co-axial with the ion trajectory. In calculations, the secondary electrons produce many further electrons before terminating their trajectory at some radius and individual history which depend on the initial energy of electrons. These further electrons are also calculated. The author counts the electrons which cross the sides of cylinders, with radius increasing in steps of 0.1 nm, and evaluated the number of electrons that cross the sides of each cylinder in the both directions of backs and forwards (Figure 6.1.3. (a)&(b)). Figure 6.1.4. indicates the *REFIT*s at the detection thresholds for proton, He and C ions against the distance form ion's path. At a certain radius, the values of *REFIT*s increases with increasing the nuclear charge of ions. The author could not find the common value of *REFIT*s among three ions at any radius. This implies that the *REFIT*s is not acceptable as a universal parameter to describe the threshold of PADC in the present manner. However, the values of *REFIT* at a radius of 1 nm, which is the half of the length of a repeat unit of PADC, are in agreement with two steps damage formation process obtained by experiments using low *LET* radiations, which at least two electrons are mandatory to break the carbonate ester in PADC. In addition, the values of *REFIT* at the detection threshold are so closer than the local doses (Fig. 6.1.5). This implies that the *REFIT* is improved parameter compared to the local dose distribution theory (Waligorski et al., 1986). Figure 6.1.6. shows track

response data as a function of the *REFIT* at a radius of 1 nm. The three arrows indicate the detection thresholds for each ion expressed by the *REFIT*. The values of *REFIT* at the detection thresholds for each ion are also listed in Table 6.1.2. At a radius of 1nm, the value of *REFIT* for C ion is about twice of that for proton. However, it is certain that these are in the same order. In comparison to the response curves in Fig. 6.1.1., those in Fig 6.1.6. are so closer together. This implies that the author can judge the *REFIT* is an improved physical parameter relative to the stopping power. In order to improve the accuracy of the simulation of the *REFIT*, future issues are discussed in the following section.

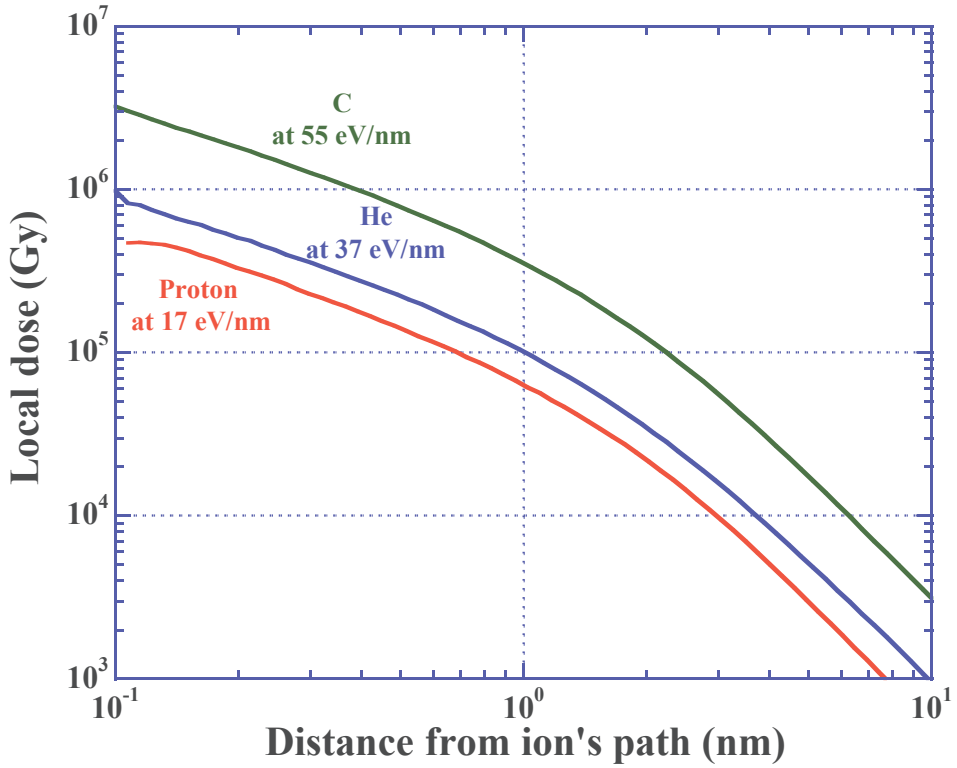

Fig. 6.1.5. Local dose distributions calculated using Geant4-DNA for proton, He and C ions at each detection threshold.

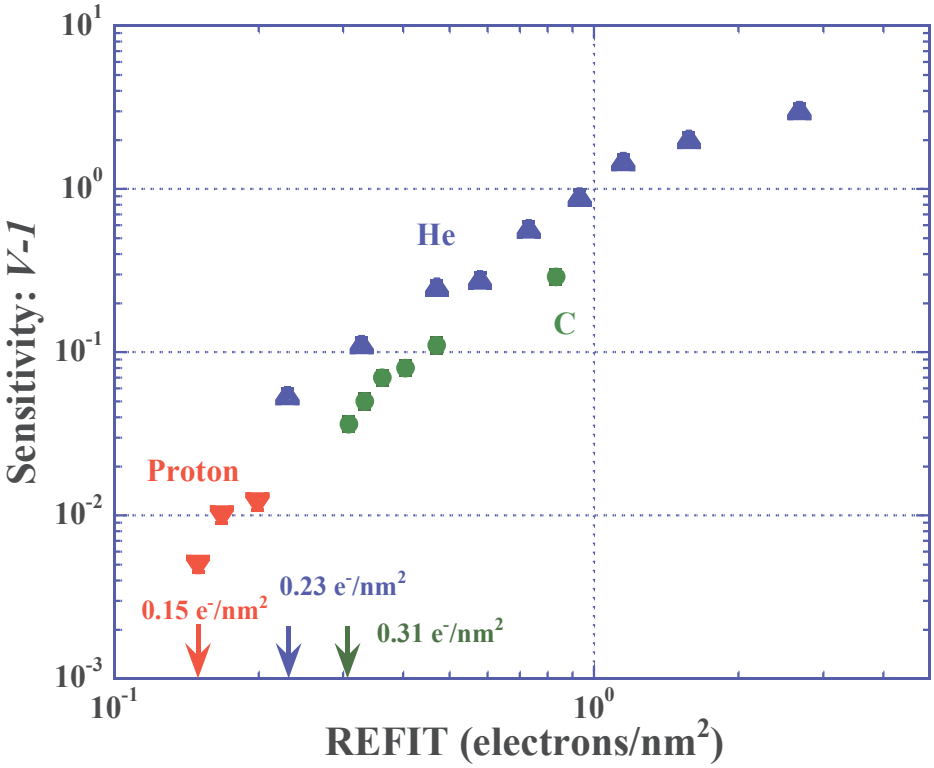

Fig. 6.1.6. Track response data as a function of *REFIT* at a radius of 1nm.

Table 6.1.2. List of the *REFIT* at the detection threshold.

Ion	*REFIT*
Proton	0.15
He	0.23
C	0.31

6.1.3. Future issues of the new physical concept

The author should address the following issues for the accurate calculation of *REFIT*:

(a) In the present simulation, all secondary electrons are ejected from the trajectories of electron, proton and heavy ions. In reality, the ionization could occur at atoms distant from the trajectories. The impact parameter, b ($b_{min} \leqq b \leqq b_{max}$), for ionization, in which is the perpendicular distance at which the Coulomb force is likely to act to excite/ionize an atom is represented in Fig. 6.1.7 (Durrani&Bull, 1987). The impact parameters at the detection thresholds for each ion are also plotted in Fig. 6.1.7 and listed in Table 6.1.3. In the case of C ion, even electrons at 5.4 nm from the track center are affected by the primary path. This implies that the values of *REFIT* around track center will be lower

than the present case when the impact parameter is included in the simulation.

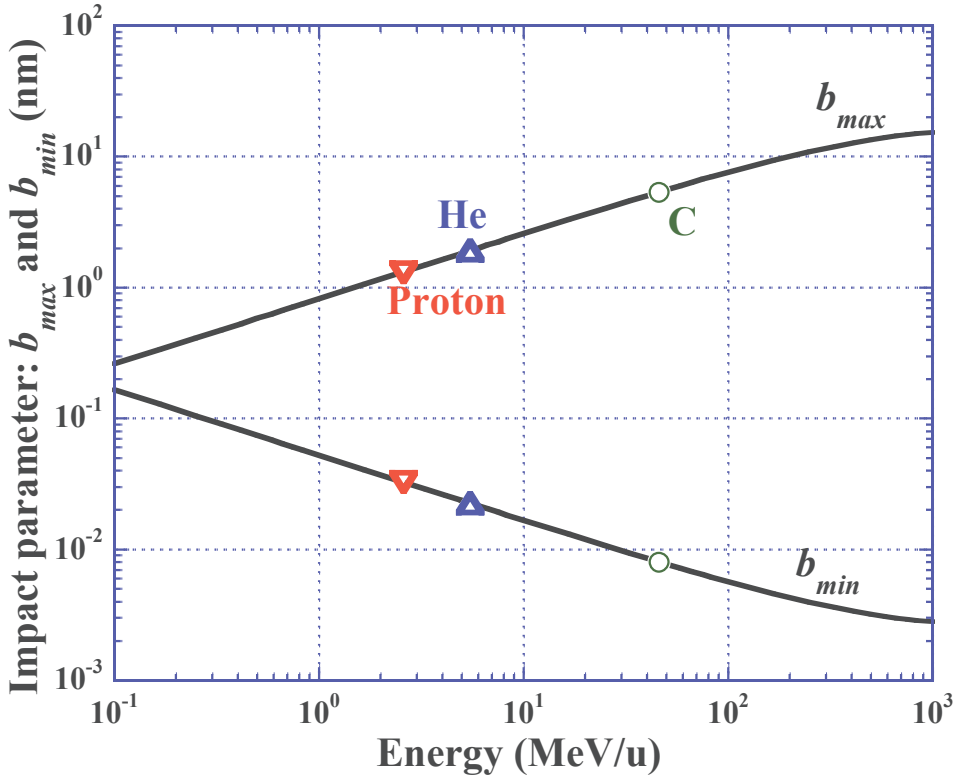

Fig. 6.1.7. Impact parameter, *b*, against the energy of ions. The plotted points are impact parameters at the detection thresholds for each ion.

(b) The electrons with energies less than cut off energy of Geant4-DNA of 7.4 eV play important role to cleave chemical bonds by processes such as dissociative electron attachment (Bazin et al., 2009; Yildirim et al., 2010; Böhler et al., 2013; Alizadeh et al., 2016). Therefore, the interactions of such low energy electrons should be taken into account to accurately determine the secondary electron histories and the density of such electrons around the ion's path. The author has just started to investigate the low energy electron impacts on condensed monomers using Time of Flight mass spectrometry at Université de Sherbrooke, Canada (Rowntree et al., 1991a&b, Sanche, 2000). The contribution to more accurate simulation is expected using the results in Canada.

(c) To build a more physically realistic model, PADC must be used as the target instead of the virtual stopping media. The calculation in the materials that contain carbon atoms is mandatory as a next step. The application of the Geant4-DNA for the DNA bases has been began (Francis et al., 2017). The author expects that this application will be extended to the polymers, including PADC near the future.

6.2. Estimation of the removal cross section for each track

In this section, the removal cross sections for protons and heavy ions are evaluated based on the radial distribution theory. The obtained results are compared to the experimental ones and previous ones. The experimental derivation process was given in chapter 5. Such an approach is important to define the best physical parameters which are able to describe the chemical structure of a latent track.

6.2.1. Radial dose distributions around the ion tracks

The radial dose distributions in the virtual stopping media for proton, He, C and Fe ions with incident energies of 5.7, 5.5, 4.8 and 2.3 MeV/u, respectively, are calculated using the Geant4-DNA as shown in the solid curves of Fig. 6.2.1. The radial dose distributions in PADC are also evaluated from the conventional theory as indicated in broken curves of Fig. 6.2.1 (Waligorski et al., 1986). The radial dose distributions calculated using the Geant4-DNA are well concordant with that from conventional radial dose distribution theory.

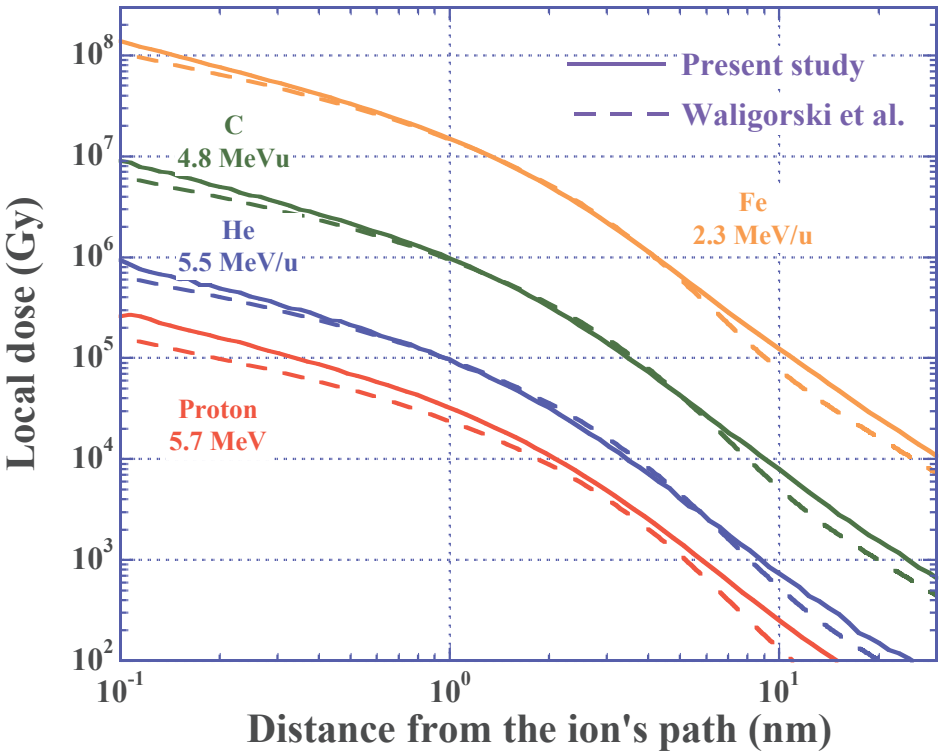

Fig. 6.2.1. Radial dose distributions around the paths of proton, He, C and Fe ions calculated by Geant4-DNA (solid lines) and by radial distribution model (broken lines).

6.2.2. Estimation of the removal cross sections for protons and heavy ions

Radial dose distribution model was developed in order to express the response of the Nuclear Emulsion (Katz and Pinkerton, 1975). This model was also applied to describe the chemical damage structure of latent tracks in ETDs (Barillon et al., 2013&2015). In the present study, the values of removal cross sections is estimated using Geant4-DNA based on the radial dose distribution theory.

The probability, *P(r)*, of breaking given functional groups is defined as,

$$P(r) = \{1 - exp(-D(r)/D_0)\}^x, \quad (6.2.1)$$

where *r* is distance from the ion trajectory in the radial direction, *D(r)* radial dose at a certain distance, D_0 the dose at which there is one hit per target and *x* the number of hits needed to break a bond (Barillon et al., 2002). The dose quantity concept was proposed by Miterev in order to describe the relationship between V_t and the ion parameters (Miterev, 1995). In the case of PADC, the inverse correlation between G values and the stopping power leads us to adopt one as *m*. The probabilities of the breaking of carbonate ester for proton, He, C and Fe ions with incident energies of 5.7, 5.5, 4.8 and 2.3 MeV/u,

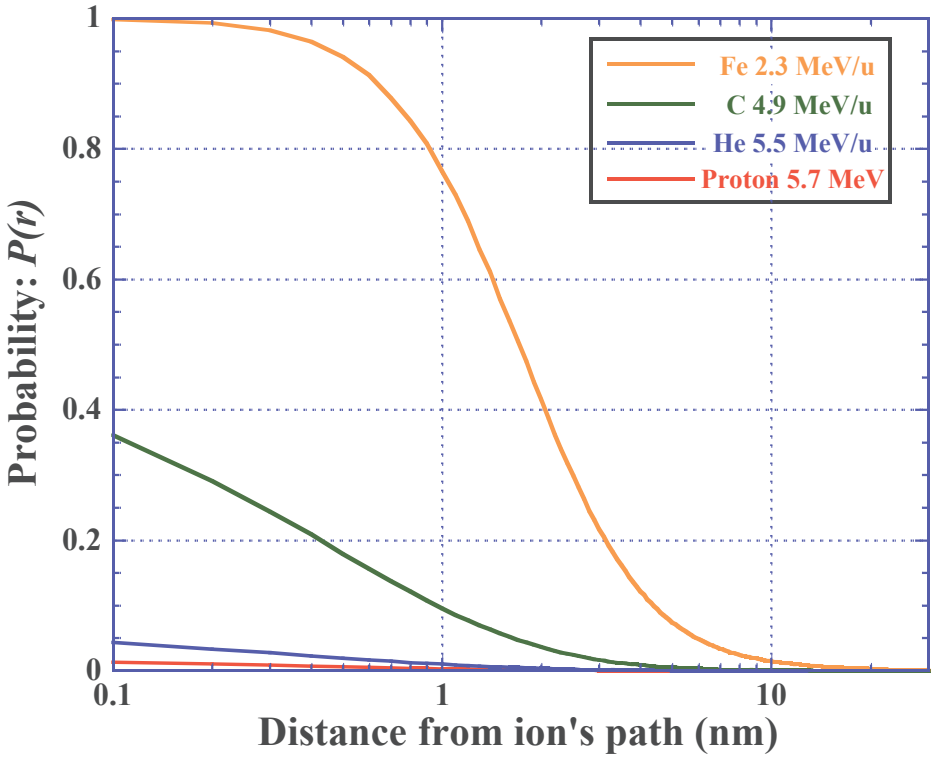

Fig. 6.2.2. Probability of carbonate ester breaking at radial distance from ion's path. The simulations are made using Eq. 6.2.1 for a D_0 value of 5 MGy.

respectively, are calculated from Eq. 6.2.1. as represented in Fig. 6.2.2. In the present

study, 5 MGy is adopted as D_0 to fit the experimentally obtained results. For proton and He ion, the probability of the carbonate ester breaking is less than 10% at the track center. It means the original structure of PADC is conserved even around the track center of proton and He ion. In comparison to this, the probability of Fe ion is almost 100% around the track center. This implies that the original network of PADC is completely disappeared around the trajectory of Fe ion. The probability gives us fruitful information for ion track structure in PADC.

Using the probability, the removal cross section for each track can be determined as,

$$\sigma = 2\pi \int_0^{r_{max}} P(r) \cdot r dr, \tag{6.2.2}$$

where r_{max} is the maximum range of most energetic secondary electron produced by ion irradiations. Figure 6.2.3. shows removal cross sections for proton, He, C and Fe ions as

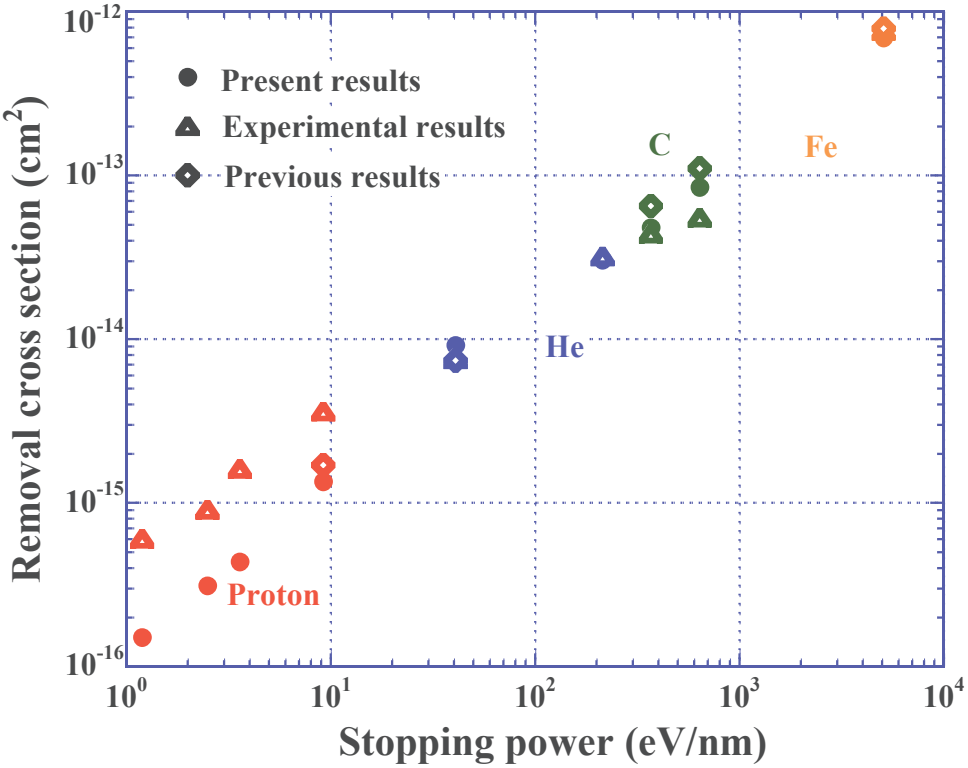

Fig. 6.2.3. Removal cross sections for each track of proton, He, C and Fe ions. The present results, experimental results (Mori et al., 2011&Kusumoto et al., 2016a) and previous results (Barillon et al., 2013) are plotted as solid circles, open triangles and open diamonds, respectively.

a function of the stopping power. The simulation results are listed in Table 6.2.1. with previous ones and experimental ones. The present results are indicated as solid circles. The experimental results of carbonate ester (Mori et al., 2011&Kusumoto et al., 2016a) and the previous calculation results (Barillon et al., 2013) are plotted as open triangles

Table. 6.2.1. Comparison of the removal cross section for carbonyl in PADC simulated by Geant4-DNA to previous ones and experimental ones.

Ion	Stopping power (eV/nm)	Present results (cm^2)	Barillon et al., (cm^2)	Experimental (cm^2)
Proton	1.2	1.5×10^{-16}	-	6.0×10^{-16}
	2.5	3.1×10^{-16}	-	9.0×10^{-16}
	3.6	4.4×10^{-16}	-	1.5×10^{-15}
He	9.3	1.3×10^{-15}	1.7×10^{-15}	3.6×10^{-15}
	40	9.2×10^{-15}	7.4×10^{-15}	7.5×10^{-15}
	210	3.1×10^{-14}	-	3.2×10^{-14}
C	370	4.7×10^{-14}	6.5×10^{-14}	4.4×10^{-14}
	650	8.5×10^{-14}	1.1×10^{-13}	1.1×10^{-13}
Fe	5200	6.9×10^{-13}	7.9×10^{-13}	7.6×10^{-13}

and open diamonds, respectively. The present results are in agreement with the experimental results and previous results of He, C and Fe ions. However, the author confirms huge discrepancies in proton of which stopping power is less than 10 eV/nm. One interpretation could be the radio-oxidation induced by ion irradiations. Significantly decrease of the G value for loss of carbonate ester in PADC exposed to gamma in vacuum were observed (Mori et al., 2013). At odds with this, the G values for loss of carbonate ester in PADC irradiated with He and C ions are hardly affected in vacuum. The previous experimental results indicate in chemical damages in PADC produced by low *LET* radiations are susceptible to surrounding environment compared to the higher ones. The simple chemical kinetics of oxidation effect was simulated in 2015 (Barillon et al., 2015). However, some discrepancy has still been remained. As a next step, the competitive process between the recombination resulting in original or altered structure and the formation of OH groups must be considered to improve the estimation of the core size.

6.3. Summary for the new physical criterion

Using Geant4-DNA, the *REFIT* was proposed to express the detection thresholds of PADC. The values of *REFIT*s for proton, He and C ions were in same order at the detection threshold. However, the *REFIT* was not acceptable parameter to describe the detection threshold of PADC. In order to improve the value of *REFIT*, future issues, including the impact parameter and the effects of electron attachment below the cut off energy were indicated. Furthermore, virtual stopping media must be replaced to the PADC

to calculate the *REFIT* precisely.

The removal cross sections for proton and heavy ions were estimated based on the conventional radial dose distribution model. The present results of heavy ions were in agreement with the experimental and previous ones. However, the model using the radial dose distribution theory was not sufficient to describe the removal cross sections below the 10 eV/nm. The competitive process between formation of OH groups and the recombination must be included in the present formula to improve the estimation.

En utilisant le code Geant4-DNA, le *REFIT* a été proposé pour exprimer les seuils de détection du PADC. Les valeurs de *REFIT* pour les protons, les ions He et C sont du même ordre de grandeur autour du seuil de détection. Cependant, ce paramètre ne décrit pas parfaitement, dans les conditions actuelles, le seuil de détection du PADC. Afin d'améliorer ce concept, l'auteur propose d'étudier l'influence du paramètre d'impact et les effets des électrons de basse énergie en dessous de l'énergie de coupure du code utilisé (7,4 eV). Le code de calcul doit aussi âtre amélioré en tenant compte de la réelle composition du PADC.

Dans un autre temps, les sections efficaces de rupture de liaisons pour les protons et les ions lourds ont été simulées sur la base du modèle de la dose radiale. Les simulations pour les ions lourds sont en accord avec les données expérimentales. Cependant, le modèle de la dose radiale ne permet pas de décrire les sections efficaces au-dessous d'un seuil de 10 eV/nm. Les processus compétitifs entre la formation de groupes OH et la recombinaison radicalaire devront être inclus dans ce modèle pour améliorer la simulation.

Chapter 7
Conclusions

In this thesis, the modified structure and formation mechanism of latent tracks of protons and heavy ions in poly(allyl diglycol carbonate), PADC, as the most sensitive etched track detector have been examined using FT-IR spectrometry and a Monte Carlo simulation for the secondary electrons. The author intended to find the reason behind the excellent performance of PADC from the view of the molecular arrangement and to drive a novel appropriate physical parameter to describe track registration property.

The amount of OH groups that formed along the ion tracks as new end-points of the polymeric network has been determined. The amount of OH groups was almost equivalent to the loss amount of ether, which is the most radio-sensitive section in PADC. This is concordant with the previously proposed ion track model that the etch rate ratio should be proportional, linear to the density of hydrophilic groups along latent tracks.

Through comprehensive studies on the irradiation effects due to low Linear Energy Transfer, *LET*, radiations, including gamma rays from a Co-60 source, 1.5 keV Ultra-Soft X rays, USX, 28 MeV electron beams, and UV lights with a wave length of 222 nm, the second hit of electrons in a single repeat unit was confirmed to play an important role in the production of irreversible damages on carbonate ester. Each repeat unit of PADC has one ether in the center and two carbonate esters in symmetric positions, and these are connected by the ethylene groups. A single electron can cleave the ether but it is hardly able to break the carbonate ester. It can be broken only after the cleavage of the adjacent ether in the same repeat unit. In other words, the radiation chemical yield for the loss of carbonate ester suddenly increases when the overlapping of electron tracks becomes significant. Such overlapping of electrons is quite popular around the ion tracks. This funding makes it possible to explain the layered structure of ion tracks in PADC, namely, the effective track radius for the loss of ether is always larger than that of carbonate ester and others.

Quantitative analysis has been carried out on the structure of high-energy proton tracks (20, 30, 70 MeV) that were never registered as etchable tracks. Comparing to the results of analyses with that of etchable tracks of lower energy protons and heavy ions, the specific structure for un-etchable tracks was found that the radial extent of damage was limited within the single repeat unit of PADC. Stated differently, the ion tracks in PADC will be etchable when at least two radio-sensitive sections were lost in the radial direction. The present conclusion was based on experimental results that the radiation chemical yield for the loss of CH groups composing the ethylene between the ether and carbonate ester is significantly higher than that of CH groups in the radio-tolerant section

of PADC formed as a result of polymerization. On the basis of the experimental results obtained for this thesis, it is possible to state that the number of electrons is more suitable parameter to describe the step-like damage formation process than the local dose, Restricted Energy Loss, *REL*, and Primary Ionization, *PI*, and Z_{eff}/β which is ratio of the effective charge of heavy ions to the velocity of the ion speed normalized to the light speed in vacuum and the other related parameters.

As a new physical concept of Radial Electron Fluence around Ion Tracks, *REFIT*, has been proposed to express the detection threshold of PADC using experimentally obtained criterion. The *REFIT* is the number density of secondary electrons that pass through the cylindrical surface with a certain radius, that is co-axial with ion trajectory. The Geant4-DNA Monte Carlo Simulation toolkit has been applied to follow the electron tracks down to 7.4 eV. As a whole, the present study opened a new stage of studies on the latent tracks using molecule level measurements and simulations for the low energy electrons below 10 eV around tracks, pointing the important role of multi-electron hits on the radio-sensitive parts in PADC. The obtained fundamental knowledge is helpful to find appropriate molecule arrangements for new polymeric track detector with desired sensitivities.

The detailed results of the present study are follows:

1. The modified structure of latent tracks in PADC has been examined by a series of FT-IR measurements for high energy protons (20, 30 and 70 MeV). A fundamental data base for chemical damage parameters of ion tracks, namely, damage density, which is the amount of losses of considered functional groups per unit distance of track length, effective track core radius, in which the considered chemical groups are lost in the original atomic distribution, and the radiation chemical yield, G value, has been completed, covering the stopping powers ranging from 1.2 to 12,000 eV/nm. The amount of OH groups was also determined, as well as those of ether and carbonate ester. As reference experiments, irradiation effects of PADC by gamma rays from Co-60 source, 1.5 keV Ultra Soft X-ray, 28 MeV electron beams and UV light with a wavelength of 222 nm have been also examined.

2. The quantitative analyses by FT-IR measurements were based on the Beer-Lambert law that told us that the absorbance of the considered chemical bond is given by the product of the molar absorption coefficient, molar density of the chemical bond and the thickness of the sample. The molar absorption coefficient of OH groups was determined as 9.7×10^{3} $M^{-1}cm^{-1}$ on the basis of the correlation between the mass of

water absorbed in PADC and the absorbance around the 3500 cm^{-1}, that is assigned as the vibration mode of OH groups. Karl Fischer titration method was utilized to determine the mass of water in PADC, as well as the gravimetric method. The amount of OH groups decorating new ending points produced by the irradiations is equivalent to the damage density for loss of ether. The present result is well concordant with the previously proposed track model that the track etch rate is governed by the density of the hydrophilic group along latent tracks.

3. The investigation of the chemical damage structure in PADC exposed to gamma rays from Co-60 source was made at the absorbed doses between 30 and 150 kGy. The relative absorbance of ether in PADC decreased linearly with increasing the absorbed dose. In comparison to this, the relative absorbance of carbonyl did not decrease below the critical dose of 60 kGy. A similar result was also obtained in the case of USX exposure, in which the relative absorbance began to decrease at the critical dose of 50 kGy. These critical doses are equivalent to each other, judging from the experimental error. It was apparent that the loss of carbonyl was caused by some kind of dual stage damage formation process, which should be related to the overlapping of the secondary electrons.

4. In order to confirm the role of the overlapping of electron tracks for the damage of carbonyl, irradiation effects of PADC due to 28 MeV electron beams were examined. The relative absorbance of carbonyl turned to decrease above the critical fluence of 1.6×10^{15} electrons/cm^2, which corresponds to the absorbed dose of 50 kGy. The present critical dose is also equivalent to those of the gamma rays and the USX rays within experimental error. Using the conventionally developed track overlapping model, the effective radius for 28 MeV electrons was evaluated as 0.05 nm, that is so close to effective electron track radius for loss of ether. It was found that the carbonyl composing the carbonate ester should be destroyed when the adjacent ether was cleaved. In other words, the radiation chemical yield for the loss of carbonyl in PADC exposed to 28 MeV electrons increased suddenly above the critical fluence of 1.6×10^{15} electrons/cm^2. The generation rate of OH groups decreased at the critical fluence. The sandwiched ethylene between ether and carbonate ester should be released effectively above the critical fluence, keeping the amount of newly produced end points within each repeat unit.

5. The quantum yields of typical functional groups in PADC exposed to UV lights with

a wavelength of 222 nm were also investigated. The number density of ether, C-O-C composing the carbonate ester decreased monotonically with photon fluence. Above the critical photon fluence of 3.0×10^{19} photons/cm^2, the carbonyl turned out to decrease. The decarboxylation process releasing CO or CO_2 gasses was also observed above the critical photon fluence. The conventional track overlapping model was reconstructed to estimate the size of point-like defects due to the exposure to UV lights, assuming a spherical form as the defect with a certain radius. The size of UV defects was assessed as 0.02 nm. Comparing the spatial distribution of the defects on the ether at the critical fluence, it was inferred that scissions of ether along 28 MeV electron has more complicated structure compared to the UV defects.

6. The studies by the predecessors on the latent tracks in PADC have covered wide experimental conditions. However, the present study has dealt firstly with latent tracks which are never etchable, namely, below the detection threshold for etch pit formation. The modified structure has been made for PADC irradiated with high energy protons with energies of 20, 30 and 70 MeV. The damage densities and effective track core radius for losses of ether and carbonate ester for these protons in PADC were identical to the trends of previously reported results of 5.7 MeV proton, He and C ions. Focusing on the CH groups, however, the plateau region was observed on the damage density and the effective track core radius around the stopping power of 17 eV/nm, which corresponds to the detection threshold of proton. The G value for loss of CH groups is higher between the radio-sensitive sections, this implies that the damage for the un-etchable track is limited within a single repeat unit. The present result indicates that etch pits were generated when at least two radio-sensitive sections were lost. Furthermore, the radiation chemical yields of 70 MeV protons were greater than that of gamma ray, which gave the most uniform damage distribution. It confirmed that relatively dense damages along the proton tracks suppressed the recombination resulted in the original molecular arrangements. This is concordant with the previous results of semi-relativistic heavy ions, C, Fe and Xe ions with energies higher than 100 MeV/u.

7. Including the high energy protons, it has been confirmed that the effective track core radius for loss of ether is always larger than that of carbonate ester. The core radius for the loss of CH groups is the smallest among the three in all examined ions. The ion tracks in PADC have their own layered structure. The layered structure is well concordant to the dual stage damage formation process on the carbonyl observed for

the gamma ray, the USX and the 28 MeV electron. The secondary electrons should start their travel from the vicinity of the ion trajectory. Number density of the electron should be reduced with increasing the distance from the track center. Because ether can be cleaved even by a single electron, the core radius should be larger. In the case of carbonate ester, at least two electrons should hit the radio-sensitive section in the repeat unit of PADC. As a result, the corresponding core radius should be suppressed. CH groups between the radio-sensitive parts might be released after the breaking at ether and carbonate ester. The layered structure in PADC was dominated by the amount of secondary electrons around ion tracks. The radio-tolerant part with polyethylene-like structure should be lost when the all connected radio-sensitive parts were damaged. In this context, the amount of secondary electrons should be an appropriate physical value to express the damage registration property in PADC, instead of conventional physical parameters such as Restricted Energy Loss, the local absorbed dose and the others.

8. The Geant4-DNA Monte Carlo Simulation toolkit has been applied to follow the secondary electron tracks down to 7.4 eV. PADC was treated as a virtual stopping media whose chemical composition is identical to water and density is 1.31 g/cm^3. The radial dose distributions for proton, He, C and Fe ions calculated by the Geant4-DNA were consistent with those from the local dose distribution model proposed by Waligorski et al. A new physical concept of Radial Electron Fluence around Ion Tracks, *REFIT*, which is defined as the number density of secondary electrons that passed through the cylindrical surface with a certain radius has been proposed. The axis of the cylindrical surface were identical to each ion trajectory. The values of the *REFIT*s for proton, He and C ions at each detection threshold with a radial distance of 1 nm from the ion path were in agreement with experimentally proposed Muti-hits model, which said at least two radio-sensitive parts must be broken when the latent tracks are etchable. Future problems have been summarized, including the impact parameter relating to the initial locations of the secondary electrons, the effects of electron attachment in PADC and chemical composition of the virtual stopping media to improve the accuracy of the values of *REFIT*s.

Dans cette thèse, la structure et le mécanisme de formation des traces latentes de protons et d'ions lourds dans le poly allyl diglycol carbonate, PADC, ont été étudiés en utilisant la spectroscopie FTIR et une simulation de type Monte Carlo. L'intention de l'auteur est de comprendre l'excellente performance du PADC en tant que détecteur de traces nucléaires et de proposer un nouveau paramètre physique pour décrire le seuil de détection du PADC.

La quantité de groupes OH qui se forment le long des traces latentes d'ions a été pour la première fois déterminée. La quantité de groupes OH formés est équivalente à la perte des fonctions éther, qui sont les fonctions les plus sensibles aux rayonnements. Ceci est en accord avec le fait que la révélation chimique d'une trace latente est directement liée la densité des groupes hydrophiles présents le long des traces.

L'utilisation de rayonnement de faibles transferts d'énergies ; rayons gamma, rayons X, faisceaux d'électrons de 28 MeV, et photons UV de longueur d'onde de 222 nm, a prouvé le rôle crucial du nombre d'électrons nécessaires dans la production de dommages irréversibles sur l'ester de carbonate. Le PADC est composé d'un éther au centre et deux esters de carbonate dans des positions symétriques reliés entre eux par des groupes de type polyéthylène. Un seul électron peut cliver une liaison éther, ce qui n'est pas le cas pour les fonctions ester de carbonate. Ces fonctions ne disparaissent qu'après le clivage de l'éther adjacent dans la même unité de répétition. En d'autres termes, le rendement radiolytique de disparition des esters de carbonate augmente soudainement lorsque le recouvrement des traces d'électrons secondaires produit par le rayonnement incident devient significatif.

Une analyse quantitative a été réalisée sur la structure des traces latentes de protons de haute énergie (20, 30, 70 MeV) qui n'induisent pas de traces révélées. Cette analyse quantitative a prouvé qu'une trace latente peut être révélée lorsqu'au moins deux parties radio-sensibles dans deux unités de répétition adjacente du PADC sont perdues dans la direction radiale de l'ion. Sur la base des résultats expérimentaux obtenus lors de cette thèse, il est possible d'affirmer que le nombre d'électrons est le paramètre le plus approprié pour décrire le processus de formation d'une trace latente, bien mieux que les autres paramètres utilisés jusqu'ici dans la littérature tels que la dose locale, ou la perte d'énergie restreinte (*REL*), ou l'ionisation primaire, ou encore le rapport Z_{eff}/β qui est le rapport de la charge effective d'un ion à sa vitesse normalisée par rapport à la vitesse de la lumière dans le vide.

La fluence électronique radiale autour de la trace d'un ion, *REFIT*, a été proposée comme nouveau concept pour exprimer le seuil de détection du PADC.

REFIT est la densité en électrons secondaires produit par l'ion incident qui traverse une surface cylindrique de rayon donné coaxiale à la trajectoire de l'ion. Le code Geant4-DNA utilisé permet de travailler avec des électrons ayant une énergie minimale de 7.4 eV. Dans son ensemble, la présente étude ouvre une nouvelle voie de réflexion sur la formation d'une trace latente. Les connaissances fondamentales obtenues sont également utiles pour trouver des arrangements moléculaires appropriés pour développer de nouveaux détecteurs de traces polymériques avec des sensibilités contrôlées.

Les résultats détaillés de la présente étude sont les suivants:

1. La structure chimique des traces latentes dans le PADC a été examinée par une série de mesures FTIR pour des protons de haute énergie (20, 30 et 70 MeV). Une base de données fondamentales a donc été créée sur la quantité de pertes (ether, ester de carbonate, liaisons CH) et de formation de groupes fonctionnels (OH) pour des transferts d'énergie allant de 1,2 à 12 000 eV/nm. Des mesures quantitatives avec des rayonnements gamma (Co-60 source), X (1,5 keV), des électrons de 28 MeV et des photons UV de longueur d'onde de 222 nm ont également été réalisées.

2. Les analyses quantitatives par mesures FTIR sont basées sur la loi de Beer-Lambert. Le coefficient d'absorption molaire des groupes OH a été déterminé comme $9,7\times10^3$ $M^{-1}cm^{-1}$ sur la base de la corrélation entre la masse d'eau absorbée dans le PADC et l'absorbance autour du nombre d'onde 3500 cm^{-1}. Les méthodes gravimétrique et le titrage Karl Fischer ont été utilisées pour déterminer la masse d'eau absorbée par le PADC. L'hypothèse est faite que ce coefficient déterminé pour l'eau absorbée dans le PADC puisse être utilisé pour estimer la quantité de groupement OH formés après irradiation. La quantité de groupes OH ainsi estimé après irradiation est équivalente à la perte des fonctions éther. Ce résultat est en parfait accord avec le fait que la vitesse de révélation chimique d'une trace latente est proportionnelle au nombre de groupes hydrophiles créés dans la trace.

3. L'étude de la structure des dommages chimiques dans le PADC exposés aux rayons gamma avec une source de Co-60 a été réalisée à des doses comprises entre 30 et 150 kGy. Si l'absorbance relative de la fonction éther diminue linéairement avec la dose, celle du carbonyle ne diminue qu'au delà d'une dose critique de 60 kGy. Les mêmes tendances ont été observées pour une exposition à des X mous, avec une dose critique quasiment identique (50 kGy). Il semble donc évident que la perte de la fonction

carbonyle est associée à un mécanisme à deux étapes, certainement lié au recouvrement des électrons secondaires produits par les rayonnements primaires.

4. Afin de confirmer le rôle du recouvrement des traces d'électrons pour la disparition de la fonction carbonyle, des irradiations ont été effectuées avec des faisceaux d'électrons de 28 MeV. L'absorbance relative de la fonction carbonyle diminue au-delà d'une fluence critique de $1{,}6\times10^{15}$ électrons/cm^2, ce qui correspond à une dose absorbée de 50 kGy identique à celle observée précédemment avec les photons gamma et X. En utilisant le modèle classique de recouvrement des traces, le rayon effectif pour des électrons de 28 MeV a été évalué à 0,05 nm, très proche du rayon de la trace à l'intérieur duquel la perte de la fonction éther est majoritaire. La conclusion pour l'irradiation avec des électrons est identique à celle de l'irradiation avec des photons, le carbonyle composant l'ester de carbonate n'est détruit que lorsque la liaison éther adjacente est rompue. On observe également que la formation de groupes OH stagne au-delà de la fluence critique. La partie polyéthylène situé entre l'éther et l'ester de carbonate est relâché au-delà de la fluence critique sans modifier la quantité des groupements OH formés.

5. Les rendements quantiques de modification des groupes fonctionnels du PADC exposé à des photons UV de 222 nm ont également été déterminés. La densité en nombre d'éther, C-O-C composant l'ester de carbonate diminue de façon monotone avec la fluence des photons. Au-dessus d'une fluence photonique critique de $3{,}0\times10^{19}$ photons/cm^2, la fonction carbonyle commence à disparaitre. Un processus de décarboxylation libérant du CO et/ou du CO_2 a également été observé au-dessus de cette fluence critique. En supposant une forme sphérique, la taille des défauts UV a été évaluée à 0,02 nm. On retrouve donc un comportement similaire du PADC pour tous les types d'irradiation effectués, même si une analyse plus fine semble montrer que les mécanismes de scission des liaisons éther diffèrent entre une irradiation électronique et une irradiation UV.

6. Ce travail de thèse complète les études expérimentales précédentes réalisées sur le PADC en travaillant, pour la première fois, sur la structure chimique de traces latentes qui ne sont pas chimiquement révélables, pour des protons de haute énergie (20, 30 et 70 MeV). En se concentrant sur la disparition des groupes CH, un plateau est observé

autour d'un transfert d'énergie de l'ordre de 17 eV/nm, ce qui correspond au seuil de détection des protons. Le rayon de la trace correspondant à ce plateau démontre qu'une trace latente n'est révélée que lorsque deux segments radio-sensibles dans deux unités de répétition sont perdus. De plus, les rendements radiolytiques mesurés pour des protons de 70 MeV sont systématiquement supérieurs à ceux observés pour les rayons gamma, confirmant ainsi que la densité du dépôt d'énergie dans les traces de protons suppriment en partie la recombinaison des radicaux initialement formés. Ceci est en accord avec les résultats précédents obtenus avec des ions lourds semi-relativistes (C, Fe et Xe) avec des énergies supérieures à 100 MeV/u.

7. En incluant les protons de haute énergie, il a été confirmé que le rayon effectif de la trace pour la perte d'éther est toujours plus grand que celui de l'ester de carbonate. Le rayon effectif pour la perte des groupes CH est toujours le plus faible. Les traces d'ions dans le PADC présentent donc une structure en couches. Cette structure en couches est corrélée au mécanisme de formation des dommages et au nombre d'électrons secondaires produits par l'ion incident. Parce que la liaison éther peut être coupée par un seul électron, le rayon de la trace associée à cette fonction est le plus grand. Le rayon associé à l'ester de carbonate est plus faible car au moins deux électrons sont nécessaires pour sa disparition, sachant que la densité radiale d'électrons secondaires diminue avec l'éloignement du cœur de la trace. Les groupements CH sont quant à eux libérés seulement après rupture de l'éther et de l'ester carbonate, expliquant que le rayon associé à ces groupements soit le plus faible de tous. La structure en couches semble donc être dominée par la quantité d'électrons secondaires produit par l'ion incident bien plus que par les paramètres physiques classiques comme la perte d'énergie restreinte (*REL*) ou encore la dose absorbée.

8. Le code Monte-Carlo Geant4-DNA a été utilisé pour suivre la production d'électrons secondaires, jusqu'à une énergie de 7.4 eV, induite par le passage d'un ion. Le PADC a été traité comme un milieu d'arrêt virtuel dont la composition chimique est identique à celle de l'eau mais avec une densité de 1,31 g/cm^3. Les distributions de doses radiales calculées pour les protons et les ions He, C et Fe sont cohérentes avec celles du modèle de distribution de dose locale proposé par Waligorski et al. Un nouveau concept physique, la fluence électronique radiale autour d'une trace ionique (*REFIT*), est défini comme la densité d'électrons secondaires traversant une surface cylindrique de rayon donné. L'axe de la surface cylindrique est confondu avec la trajectoire de l'ion. Le rayon est fixé à 1nm, en accord avec le fait que deux unités de répétition adjacentes

du PADC doivent être affectées pour qu'une trace latente puisse être révélée. Les valeurs *REFIT* ainsi obtenues correspondant respectivement aux seuils de détection des protons, et des ions He et C, même si elles sont très proches les unes des autres ne convergent cependant pas vers une valeur unique. Des pistes sont finalement proposées pour améliorer ce concept, comme la prise en compte du paramètre d'impact entre l'ion incident et les électrons de la cible, les effets des électrons de basse énergie (attachement dissociatif), ainsi que la prise en compte de la réelle composition chimique du PADC dans le code Géant4-DNA.

Acknowledgments

指導教官の神戸大学大学院海事科学研究科の山内知也教授は研究の遂行にあたり、丁寧かつ温かな指導と議論に薫陶を受けました。また、筆者の研究成果の発表をする場や国内外の外部研究機関の方々との共同研究を進めるための環境を与えていただきました。ここに深く感謝の意を表します。

The author must express great appreciate to Prof. Rémi Barillon of Institute Pluridisiplinaire Hubert Curien for his guidance and adequate discussions.

神戸大学大学院海事科学研究科の小田啓二教授におかれましては、筆者の研究遂行にあたり、深い知識から多くの貴重な議論と助言を賜りました。心より感謝致します。

My heartfelt appreciation goes to Prof. Nourreddine Abdel-Mijid of Institute Pluridisiplinaire Hubert Curien for his guidance and adequate discussions.

神戸大学先端融合研究環の藏重久弥教授には丁寧な指導と助言を賜りました。また、外部研究機関の方々との共同研究を進めるための環境を与えて頂きました。ここに、深く感謝の意を表します。

The author hopes to thank Dr. Yvette Ngono-Ravache of Centre de Recherche sur les Ions, les Matériaux et la Photonique for her guidance and kind discussions.

量子科学技術研究開発機構 高崎量子応用研究所の田口光正博士には、深い知識と経験より様々な議論及び助言を賜りました。ここに深く感謝いたします。

The author would like to express the heartfelt appreciation to Dr. Christelle Roy of Institute Pluridisiplinaire Hubert Curien for his guidance and adequate discussions.

神戸大学海事科学研究科の蔵岡孝治教授におかれましては、深い経験と知識より様々な議論と助言を賜り、心より感謝致します。

The author had the supports and encouragements of Prof. Michel Fromm of Universite de Bourgogne-Franche-Comte for his guidance and adequate discussions.

神戸大学先端融合研究環の岡田勝吾助教には筆者の研究遂行にあたり深い経験と知識より様々な議論と助言を賜りました事、厚く感謝いたします。

The author is deeply grateful to Dr. Ziad EL Bitar and Dr. Nicolas Arbor of Institute Pluridisiplinaire Hubert Curien for his guidance and adequate discussions.

国立研究開発法人量子技術研究開発機構　放射線医学総合研究所の小平聡博士ならびに北村尚氏におかれましては、筆者の同研究所における実験に際して多大な協力と助言を賜り、深く感謝致します。

放射線医学総合研究所の研究員の皆様、HIMAC のスタッフの皆様には、同研究所でのイオン照射にあたり、多大な支援を賜りました事、厚く御礼申し上げます。

電子線及びガンマ線照射実験の実施にあたり、大阪大学産業科学研究所量子ビーム科学研究施設の誉田義英准教授、藤乗幸子助教及び研究院の皆様に多大なご協力を賜りました事、深く感謝の意を表します。

The author is grateful to Dr. Quentin Raffy of Institute Pluridisiplinaire Hubert Curien for fruitful discussions and suggestions.

The author is deeply grateful to Christopher Gomez of Graduate school of Maritime Sciences, Kobe University for improving the English sentence.

The author expresses much thanks to Mr. Nicolas Ludwig and Dr. Guillaume Fleury for supporting of this study in Strasbourg.

神戸大学大学院海事科学研究科の森豊博士、金崎真聡助教には貴重な多大な協力及び助言を賜りました。心より感謝いたします。

神戸大学大学院海事科学研究科の環境応用計測科学研究室の先輩、後輩の皆様には多大な協力と助言を頂きました。深く感謝いたします。

最後になりましたが、学部、修士、博士と長い学生生活を、様々な面からサポートしてくださった家族に感謝の意を表します。

List of published papers

1. Tamon Kusumoto, Yutaka Mori, Masato Kanasaki, Takuya Ueno, Yuka Kameda, Keiji Oda, Satoshi Kodaira, Hisashi Kitamura, Rémi Barillon, Tomoya Yamauchi, Yields on the formation of OH groups and the loss of CH groups along nuclear tracks in PADC films, *Radiation Measurements*, **83**, 59-62 (2015).

2. Tamon Kusumoto, Yutaka Mori, Masato Kanasaki, Ryunosuke Ikenaga, Keiji Oda, Satoshi Kodaira, Hisashi Kitamura, Rémi Barillon, Tomoya Yamauchi, Radiation chemical yields for the losses of typical functional groups in PADC films exposed to high energy protons above the detection threshold, *Radiation Measurements*, **87**, 35-42 (2016).

3. Tamon Kusumoto, Yutaka Mori, Masato Kanasaki, Keiji Oda, Satoshi Kodaira, Yoshihide Honda, Sachiko Tojo, Rémi Barillon, Tomoya Yamauchi, Sudden Increase of the radiation chemical yield for loss of carbonate ester in PADC detector where the track overlapping of 28 MeV electrons becomes significant, *JPS. Conference Proceedings*, **11**, 010001 (2016).

4. Nabil M. Hassan, Yuri Matai, Tamon Kusumoto, Yutaka Mori, Masato Kanasaki, Keiji Oda, Hisashi Kitamura, Teruaki Konishi, Satoshi Kodaira, Nakahiro Yasuda, Tomoya Yamauchi, On the mechanism of the sensitization of PADC(poly(allyl diglycol carbonate)) track detectors by carbon dioxide treatment, *Radiation Measurements*, **59**, 23-29 (2013).

5. Tomoya Yamauchi, Kenya Matsukawa, Yutaka Mori, Masato Kanasaki, Atsuto Hattori Yuri Matai, Tamon Kusumoto, Akira Tao, Keiji Oda, Satoshi Kodaira, Teruaki Konishi, Hisashi Kitamura, Nakahiro Yasuda, Rémi Barillon, Applicability of Polyimide Films as Etched Track Detectors for Ultra-Heavy Cosmic Ray Components, *Applied Physics Express*, **6**, 046401 (2013).

6. 楠本 多聞, 森 豊, 金崎 真聡, 小田 啓二, 誉田 義英, 藤乗 幸子, フロム ミッシェル, グロエ ジョン-エマニュエル, 小平 聡, 北村 尚, バリオン レミ, 山内 知也, PADC 飛跡検出器の放射線高感受性部に見られる段階的な損傷形成, *放射線化学*, **103**, 41-45 (2017).

7. 楠本 多聞, 寺下 佳孝, 森 豊, 金崎 真聡, 小田 啓二, 山内 知也, 小平 聡, 誉田 義英, 藤乗 幸子, EL バイタ ジアッド, アーバ ニコラ, ラフィ クアンタン, バリオン レミ, グロエ ジョン-エマニュエル, フロム ミッシェル, 高感度飛跡検出器 PADC 中に形成されるイオントラックの特徴, *放射線*, **42**, 73-82 (2017).

8. 楠本 多聞, 森 豊, 金崎 真聡, 上野 琢也, 亀田 結貴, 小田 啓二, 小平 聡, 北村 尚, 山内 知也, PADC 飛跡検出器中重イオントラック内における OH 基生成密度と CH 基損失密度の定量的分析, *神戸大学大学院海事科学研究科紀要*, **12**, 30-38 (2015).

9. 川嶋 元, 小平 聡, 井原 大輔, 安田 仲宏, 楠本 多聞, 森 豊, 山内 知也, 小林 啓一, ベントン エリック, 分子長の異なるモノマーから合成した固体飛跡検出器の開発と重粒子線による損傷解析, 放射線, 42, 83-90 (2017).

10. 松川 兼也, 山内 知也, 森 豊, 金崎 真聡, 又井 悠里, 楠本 多聞, 田尾 陽, 小田 啓二, 小平 聡, 小西 輝昭, 北村 尚, ポリイミド中重イオントラックの特性評価, 放射線, **39**, 135-144 (2014).

11. 森 豊, 楠本 多聞, 松川 兼也, 又井 悠里, 金崎 真聡, 小田 啓二, 小平 聡, 北村 尚, 小西 輝昭, 安田 仲弘, 藤乗 幸子, 誉田 義英, 山内 知也, *神戸大学大学院海事科学研究科紀要*, **10**, 21-32 (2013).

List of lectures

◎ International conference

・Oral presentation

1. Tamon Kusumoto, Yutaka Mori, Masato Kanasaki, Keiji Oda, Tomoya, Yamauchi, Satoshi Kodaira, Hisashi, Kitamura, Rémi Barillon, On the modified structure around the latent tracks in PADC films exposed to protons and heavy ions, 26th International Conference on Nuclear Tracks in Solid, I-1, Kobe (September 2014).

2. Tamon Kusumoto, Yutaka Mori, Masato Kanasaki, Keiji Oda, Yoshihide Honda, Sachiko Tojo, Satoshi Kodaira, Hisashi Kitamura, Rémi Barillon, Tomoya Yamauchi, Radiation chemical yields for loss of carbonyl bonds in poly(allyl dyglicol carbonate) and other polymeric etched track detectors at the LETs ranging from 0.025 to 12,000 keV/μm, International Symposium on Radiation Detectors and Their Uses, O21, Tsukuba (January 2016).

3. Tamon Kusumoto, Ziad EL Bitar, Shogo Okada, Pierre Gillet, Nicolas Arbor, Masato Kanasaki, Keiji Oda, Abdel-Mjid Nourredine, Hisaya Kurashige, Michel Fromm, Pierre Cloutier, Andrew D Bass, Léon Sanche, Rémi Barillon, Tomoya Yamauchi, Radial electron fluence around ion tracks as a new physical parameter for the detection threshold of PADC using Geant4-DNA toolkit, 27th International Conference on Nuclear Tracks and Radiation Measurements, Talk 12.1.4, Strasbourg (August 2017).

4. Tamon Kusumoto, Atsushi Yoshida, Tadashi Kambara, Yoshiyuki Yanagisawa, Satoshi Kodaira, Keiji Oda, Rémi Barillon, Tomoya Yamauchi, Applicability of polyimide films for identification of ultra-heavy components, including uranium ions in galactic cosmic ray, International Symposium on Radiation Detectors and Their Uses, O2, Tsukuba (January 2018).

・Poster presentation

1. Tamon Kusumoto, Koji Kuraoka, Yutaka Mori, Masato Kanasaki, Keiji Oda, Satoshi Kodaira, Yoshihide Honda, Sachiko Tojo, Rémi Barillon, Tomoya Yamauchi, Anomalous increase of the contact angle of water droplets on the surface of PADC detector exposed to proton, 27th International Conference on Nuclear Tracks and Radiation Measurements, P 1.4, Strasbourg (August 2017).

◎ **Domestic conference**

・**Oral presentation**

1. 楠本 多聞, EL バイタ ジアッド, 岡田 勝吾, ジレット ピエール, アーバ ニコラ, 森 豊, 金崎 真聡, 小田 啓二, ヌレディン アブデル-ミジッド, 藏重 久弥, フロム ミッシェル, D バス アンドリュ, 小平 聡, サンチェ レオン, バリオン レミ, 山内 知也, 第 65 回応用物理学会春季学術講演会, PADC 検出器の閾値を記述する新しい物理概念としてのイオントラック内径方向電子フルエンス, 東京 (2018 年 3 月).

2. 楠本 多聞, EL バイタ ジアッド, 岡田 勝吾, ジレット ピエール, アーバ ニコラ, 森 豊, 金崎 真聡, 小田 啓二, ヌレディン アブデル-ミジッド, 藏重 久弥, フロム ミッシェル, D バス アンドリュ, 小平 聡, サンチェ レオン, バリオン レミ, 山内 知也, 高感度飛跡検出器 PADC の閾値に対する新しい物理概念としてのイオントラック内径方向電子フルエンス, 第 32 回固体飛跡検出器研究会, 京都 (2017 年 3 月).

3. 楠本 多聞, 森 豊, 金崎 真聡, 小田 啓二, バリオン レミ, 山内 知也, 紫外線（222 nm）照射下で PADC 検出器中に形成される損傷サイズ評価, 第 64 回応用物理学会春季学術講演会, 14p-E204-2, 横浜 (2017 年 3 月).

4. 楠本 多聞, EL バイタ ジアッド, アーバ ニコラ, 小田 啓二, バリオン レミ, 山内 知也, PADC 検出器中に形成されるイオントラックと二次電子フルエンスの関係, 第 31 回固体飛跡検出器研究会, 30, 京都 (2017 年 3 月).

5. 楠本 多聞, 森 豊, 金崎 真聡, 小田 啓二, バリオン レミ, 山内 知也, 紫外線照射下で PADC 検出器に形成される損傷特性評価, 第 31 回固体飛跡検出器研究会, 29, 京都 (2017 年 3 月).

6. 楠本 多聞, 森 豊, 金崎 真聡, 小田 啓二, 誉田 義英, 藤乗 幸子, フロム ミッシェル, グロエ ジョン-エマニュエル, 小平 聡, 北村 尚, バリオン レミ, 山内 知也, PADC 検出器の放射線高感受性部に見られる段階的な損傷形成, 第 59 回放射線化学討論会, 1O11, 高崎 (2016 年 9 月).

7. 楠本 多聞, 森 豊, 金崎 真聡, 小田 啓二, 小平 聡, 北村 尚, 山内 知也, PADC 検出器中高エネルギープロトントラックの赤外線分光分析, 第 30 回固

体飛跡検出器研究会, 7, 敦賀 (2016 年 3 月).

8. 楠本 多聞, 森 豊, 金崎 真聡, 小田 啓二, 誉田 義英, 藤乗 幸子, 山内 知也, PADC 検出器中に形成される 28 MeV 電子線飛跡の構造分析, 第 30 回固体飛跡検出器研究会, 8, 敦賀 (2016 年 3 月)

9. 楠本 多聞, 森 豊, 金崎 真聡, 小田 啓二, 誉田 義英, 藤乗 幸子, PADC 検出器中に形成される 28 MeV 電子線飛跡の構造分析, 第 63 回応用物理学会春季学術講演会, 19p-W810-12, 神奈川 (2016 年 3 月).

10. 楠本 多聞, 森 豊, 金崎 真聡, 小平 聡, 北村 尚, 小田 啓二, 誉田 義英, 藤乗 幸子, 山内 知也, PADC 検出器中重イオントラック形成機構における低エネルギー電子の役割, 第 76 回応用物理学会秋季学術講演会, 16p-W2-5, 名古屋 (2015 年 9 月).
11. 楠本 多聞, 森 豊, 金崎 真聡, 小田 啓二, 小平 聡, 北村 尚, 山内 知也, PADC 検出器中重イオントラック内に形成されるヒドロキシル基の役割, 第 62 回応用物理学会春季学術講演会, 13p-A19-14, 神奈川 (2015 年 3 月).

12. 楠本 多聞, 上野 琢也, 小田 啓二, 山内 知也, 従来型実効電荷と加速器物理等で用いられる実効電荷の相互比較, 第 29 回固体飛跡検出器研究会, 10, 敦賀 (2015 年 3 月)

13. 楠本 多聞, 森 豊, 金崎 真聡, 小田 啓二, 小平 聡, 北村 尚, 山内 知也, PADC 検出器中重イオントラック内に形成されるヒドロキシル基の役割, 第 29 回固体飛跡検出器研究会, 9, 敦賀 (2015 年 3 月)

14. 楠本 多聞, 森 豊, 金崎 真聡, 小平 聡, 北村 尚, 小田 啓二, 誉田 義英, 藤乗 幸子, 山内 知也, PADC 検出器中重イオントラックの赤外分光分析, 第 28 回固体飛跡検出器研究会, 9, 神戸 (2014 年 3 月)

15. 楠本 多聞, 森 豊, 金崎 真聡, 小田 啓二, 小平 聡, 北村 尚, 山内 知也, PADC 検出器中重イオントラックの赤外分光分析(1), 第 61 回応用物理学会春季学術講演会, 18a-F1-1, 神奈川 (2014 年 3 月)

16. 楠本 多聞, 森 豊, 小田 啓二, 小平 聡, 小西 輝昭, 安田 仲宏, 山内 知也, 重イオンに対する PADC 検出器の応答特性, 第 74 回応用物理学会秋季学術

講演会, 18p-A12-6, 京都 (2013 年 9 月)

17. 楠本 多聞, ハッサン ナビル, 服部 篤人, 森 豊, 小田 啓二, 小平 聡, 小西 輝昭, 安田 仲宏, 山内 知也, 重イオンに対する PADC 検出器の応答特性, 第 27 回固体飛跡検出器研究会, 18, 神戸 (2013 年 3 月)

・Poster presentation

1. 楠本 多聞, クロウティエ ピエール, フロム ミッシェル, A.バス アンドリュ, サンチェ レオン, 山内 知也, 低エネルギー電子のエーテル基やカルボニル基を含む単量体への影響, 第 60 回放射線化学討論会, P-25, つくば (2017 年 9 月)

Awards

1. 第 1 種放射線取扱主任者試験(筆記合格). 2014 年 10 月
2. 楠本 多聞 (第 59 回放射線化学討論会学生優秀発表賞). 2016 年 9 月
3. Tamon Kusumoto (Aide à la mobilité internationale). December 2016
4. 楠本 多聞 (平成 28 年度神戸大学学生優秀学術表彰). 2017 年 3 月
5. 楠本 多聞 (第 60 回放射線化学討論会優秀賞若手ポスター部門). 2017 年 9 月

References

Agostinelli, S., Allison, J., Amako, K., Apostolakis, J., Araujo, H., Arce, P., Asai, M., Axen, D., Banerjee, S., Barrand, G., Behner, F., Bellagamba, L., Boudreau, J., Broglia, L., Brunengo, A., Burkhardt, H., Chauvie, S., Chuma, J., Chytracek, R., Cooperman, G., Cosmo, G., Degtyarenko, P., Dell'Acqua, A., Depaola, G., Dietrich, D., Enami, R., Feliciello, A., Ferguson, C., Fesefeldt, H., Folger, G., Foppiano, F., Forti, A., Garelli, S., Giani, S., Giannitrapani, R., Gibin, G., Gómez Cadenas, G.G., González, I., Gracia Abril, G., Greeniaus, G., Greiner, W., Grichine, V., Grossheim, A., Guatelli, S., Gumplinger, P., Hamatsu, R., Hashimoto, K., Hasui, H., Heikkinen, A., Howard, A., Ivanchenko, V., Johnson, A., Jones, F.W., Kallenbach, J., Kanaya, N., Kawabata, M., Kawabata, Y., Kawaguti, M., Kelner, S., Kent, P., Kimura, A., Kodama, T., Kokoulin, R., Kossov, M., Kurashige, H., Lamanna, E., Lampén, T., Lara, V., Lefebure, V., Lei, F., Liendl, M., Lockman, W., Longo, F., Magni, S., Maire, M., Medernach, E., Minamimoto, K., Mora de Freitas, P., Morita, Y., Murakami, K., Nagamatu, M., Nartallo, R., Nieminen, P., Nishimura, T., Ohtsubo, K., Okamura, M., O'Neale, S., Oohata, Y., Paech, K., Perl, J., Pfeiffer, A., Pia, M.G., Ranjard, F., Rybin, A., Sadilov, S., Di Salvo, E., Santin, G., Sasaki, T., Savvas, N., Sawada, Y., Scherer, S., Sei, S., Sirotenko, V., Smith, D., Starkov, N., Soecker, H., Sulkimo, J., Takahata, M., Tanaka, S., Tcherniaev, E., Safai Tehrani, E., Tropeano, M., Truscott, P., Uno, H., Urban, L., Urban, P., Verderi, M., Walkden, A., Wander, W., Weber, H., Wellisch, J.P., Wenaus, T., Williams, D.C., Wright, D., Yamada, T., Yoshida, J., Zschieche, D., 2003, GEANT4 - A simulation toolkit, *Nucl. Instrum. Meth. A* **506**, 250-303.

Akselrod, M.S., Yoder, R.C., Akselrod, G.M., 2006. Confocal fluorescent imaging of tracks from heavy charged particles utilizing new Al_2O_3:C,Mg crystals, *Radiation Protection Dosimetry*, 1-6.

Alizadeh, E., Ptasińska, S., Sanche, L., 2016. Transient anions in radiobiology and radiotherapy: From Gaseous Biomolecules to Condensed Organic and Biomolecular Solid, *Radiation Effects in Materials*, 179-230.

Allison, J., Amako, K., Apostolakis, J., Araujo, H., Arce Dubois, P., Asai, M., Barrand, G., Capra, R., Chauvie, S., Chytracek, R., Cirrone, G.A.P., Cooperman, G., Cosmo, G., Cuttone, G., Daquino, G.G., Donszelmann, M., Dressel, M., Folger, G., Foppiano, F., Generowicz, J., Grichine, V., Guatelli, S., Gumplinger, P., Heikkinen,A., Hrivnacova, I.,

Howard, A., Incerti, S., Ivanchenko, V., Johonson, T., Jones, F., Koi, T., Kokoulin, R., Kossov, M., Kurashige, H., Lara, V., Larsson, S., Lei, F., Link, Longo, F., Maire, M., Mantero, A., Mascialino, B., McLaren, I., Mendez Lorenzo, P., Minamimoto, K., Murakami, K., Nieminen, P., Pandola, L., Parlati, S., Peralta, L., Perl, J., Pfeiffer, A., Pia, M.G., Ribon, A., Rodrigues, P., Russo, G., Sadilov, S., Santin, G., Sasaki, T., Smith, D., Starkov, N., Tanaka, S., Tcherniaev, E., Tome, B., Trindade, A., Truscott, P., Urban, L., Verderi, M ., Walkden, A., Wellisch, J.P., Williams, D.C., Wright, D., Yoshida, H., 2006. *IEEE Trans on Nuclear Science* **53**, 270-278.

Allison, J., Amako, K., Apostolakis, J., Arce, P., Asai, M., Aso, T., Bagli, E., Bagulya, A., Banerjee, S., Barrand, G., Beck, B.R., Bogdanov, A.G., Brandt, D., Brown, J.M.C., Burkhardt, H., Canal, Ph., Cano-Ott, D., Chauvie, S., Cho, K., Cirrone, G.A.P., Cooperman, G., Cortés-Giraldo, M., Cosmo, G., Cuttoe, G., Depaola, G., Desorgher, L., Dong, X., Dotti, A., Elvira, V.D., Folger, G., Francis, Z., Galoya, A., Garnier, L., Gayer, M., Genser, K.L., Grichine, V.M., Guatelli, S., Guèye, P., Gumplinger, P., Howard, A.S., Hřivnáčová, I., Hwang, S., Incerti, S., Ivanchenko, A., Ivanchenko, V.N., Jones, F.W., Jun, S.Y., Kaitaniemi, P., Karakatsanis, N., Karamitros, M., Kelsey, M., Kimura, A., Koi, T., Kurashige, H., Lechner, A., Lee, S.B., Longo, F., Maire, M., Mancusi, D., Mantero, A., Mendoza, E., Morgan, B., Murakami, K., Nikitina, T., Pandola, L., Paprocki, P., Perl, J., Petrović, I., Pia, M.G., Pokorski, W., Russo, G., Satin, G., Sasaki, T., Sawkey, D., Shin, J.I., Strakovsky, I.I., Taborda, A., Tanaka, S., Tomé, B., Toshito, T., Tran, H.N., Truscott, P.R., Urban, L., Uzhinsky, V., Verbeke, J.M., Verderi, M., Wendt, B.L., Wenzei, H., Wright, D.H., Yamashita, T., Yarba, J., Yoshida, H., 2016. Recent developments in Geant4, *Nucl. Instrum. Meth. B*. **28**, 49-52.

Barillon, R., Fromm, M., Katz, R., Chambaudet, A., 2002, Chemical bonds broken in latent tracks of light ions in plastic track detectors, *Radiat. Prot. Dosim*. **99**, 1-4.

Barillon, R., Mori, Y., Kanasaki, M., Yamauchi, T., Yasuda, N., 2013. Chemical cross sections induced by ions in solid organic detectors: experimentation and simulation, *Radiat. Meas*. **50**, 38-42.

Barillon, R., Yamauchi, T., Mori, Y., Raffy, Q., 2015. A first attempt to simulate oxidization effects on latent track structure in PADC combining the radial dose theory and a radio-oxidation kinetic model, *Radiat. Meas*. **83**, 1-4.

Barkas, M.J., Barkas, W.H., 1963. Studies in penetration of charged particles in matter, Publ 1133, In: *Nucl. Sci. Ser. Rep*., **39** NAS NRC.

Bazin, M., Ptasińska, S., D Bass, A., Sanche, L., 2009. Electron induced dissociation in condensed-phase nitromethane I: desorption of ionic fragments, *Phys. Chem. Chem. Phys.* **11**, 1610-1618.

Berger, M., Coursey, J., Zucker, M., Chan, J., 2005. ESTAR, PSTAR, and ASTAR: Computer programs for calculating stopping-power and range tables for electrons, protons, and helium ions, Version 1.2.3.

Bernal, M.A., Bordage, M.C., Brown, J.M.C., Davídková, M., Delage, E., EL Bitar, Z., Enger, S.A., Francis, Z., Guatelli, S., Ivanchenko, V.N., Karamitros, M., Kyriakou, I., Maigne, L., Meylan, S., Murakami, K., Okada, S., Payno, H., Perrot, Y., Petrovic, I., Pham, Q.T., Ristic-Fira, A., Sasaki, T., Štěpán, V., Tran, H.N. Villagrasa, C., Incerti, S., 2015. Track structure modeling in liquid water: A review of the Geant4-DNA very low energy extension of the Geant4 Monte Carlo simulation toolkit, *Phys. Med.* **31**, 861-874.

Benton, E.R., Benton, E.V., Frank, A.L., 2002. Passive dosimetry aboard the Mir Orbital Station: internal measurements, *Radiat. Meas.* **35**, 439-455.

Benton, E.V., Nix, W.D., 1969. The restricted energy loss criterion for registration of charged particle in plastics, *Nucl. Instr. Meth*. **67**, 343-347.

Böhler, E., Warneke, J., Swiderek, P., 2013. Control of chemical reactions and synthesis by low-energy electrons, *Chem. Soc. Rev*. **42**, 9219.

Böhlke, S., Hermsdorf, D., 2008. Correlation of track etching properties of SSNTDs with the density of free radicals produced by charged particles in PADC, *Radiat. Meas*. **43**, 65-75.

Cartwright, B.G., Shirk, E.K., Price, P.B., 1978. A nuclear-track-recording polymer of unique sensitivity and resolution, *Nucl. Instrum. Meth. B*. **41**, 447-460.

Doke, T., Hayashi, T., Nagaoka, S., Ogura, K., Takeuchi, R., 1995. Estimation of dose equivalent in STS-47 by a combination of TLDs and CR-39, *Radiat. Meas.* **24**, 75-82.

Drach, J., Price, P.B., Salamon, M.H., 1987. Characteristics of cronar polyethylene terephthalate track detector, *Nucl. Instrum. Meth. B*. **28**, 49-52.

Durrani, S.A., Bull, R.K., 1987. *Solid state nuclear track detection, International series in natural philosophy* **111**.

Fleischer, R.L., Price, P.B., Walker, R.M., Hubbard, E.L., 1967. Criterion for registration in dielectric track detectors, *Phys. Rev*. **156**, 353-355.

Fleischer, R.L., 1998. Tracks to innovation-Nuclear Tracks in Science and Technology, *Springer-Verlag, New York*.

Font, L., 2009. On radon surveys: design and data interpretation, *Radiat. Meas.* **44**, 964-968.

Francis, Z., EL Bitar, Z., Incerti, S., Bernal, M.A., Karamitros, M., Tran, H.N., 2017. Calculation of lineal energies for water and DNA bases using the Rudd model cross sections integrated within the Geant4-DNA processes, *J. Appl. Phys*. **122**, 014701.

Fujii, M., Yokota, R., Atrashi, Y., 1988. New polymeric track detectors of high sensitivity (SR-86), *Nucl. Tracks Radiat. Meas*. **15**, 107-110.

Fujii, M., Asari, T., Yokota, R., Kobayashi, T., Hasegawa, H., 1993. Aging effects on a new polymeric track detector SR-90 and a model of the nuclear track formation, Nucl. Tracks *Radiat. Meas*. **22**, 199-204.

Fukuda, T., Kodama, K., Komatsu, M., Miyamoto, S., Morishima, K., Nakano, T., Omura, T., Sakatani, Y., Sato, O., 2010. The analysis of interface emulsion detector for the OPERA experiment in JAPAN Scanning facility, *J. Instrum*. **5**, P04009.

Fukuda, Y., Faenov, A.Ya., Tampo, M., Pikuz, T.A., Nakamura, T., Kando, M., Hayashi, Y., Yogo, A., Sakaki, H., Kameshima, T., Pirozhkov, A.S., Ogura, K., Mori, M., Esirkepov, J.T.Zh., Koga, J., Boldarev, A.S., Gasilov, V.A., Magunov, A.I., Yamauchi, T., Kodama, R., Bolton, P.R., Kato, Y., Tajima, T., Daido, H., Bulanov, S.V., 2009. Energy increase in multi-MeV ion acceleration in the interaction of a short pulse laser

with a Cluster-Gas target, *Phy. Rev.Lett*. **103**, 165002.

Fulford, J., Bonner, P., Goodhead, D.T., Hill, M.A., O'Neill, P., 1999. Experimental determination of the dependence of OH radical yield on photon energy: A comparison with Theoretical simulations, *J. Phys. Chem. A* **103**, 11345-11349.

Groetz, J.-E., Ounoughi, N., Mavon, C., Belafrites, A., Fromm, M., 2014. Conception and realization of a parallel-plate free-air ionization chamber for the absolute dosimetry of an ultra soft X-ray beam, *Rev. Sci. Instrum.* **85**, 083304.

Hassan, N.M., Matai, Y., Kusumoto, T., Mori, Y., Kanasaki, M., Oda, K., Kitamura, H., Konishi, T., Kodaira, S., Yasuda, N., Yamauchi, T., 2013. On the mechanism of the sensitization of PADC (Poly(allyl diglycol carbonate)) track detectors by carbon dioxide treatment, *Radiat. Meas.* **59**, 23-29.

Incerti, S., Ivanchenko, A., Karamitros, M., Mantero, A., Moretto, P., Tran, H.N., Mascialino, B., Champion, C., Ivanchenko, V.N., Bernal, M.A., Francis, Z., Villagrasa, C., Baldacchino, G., Guèye, P., Capra, R., Nieminen, P., Zacharatou, C., 2010. Comparison of Geant4 very low energy cross section models with experimental data in water, *Med. Phys.* **37**, 4692-4708.

Incerti, S., Psaltaki, M., Gillet, P., Barberet, Ph., Bardiés, M., Bernal, M.A., Bordage, M.-C., Breton, V., Davidkova, M., Delage, E., EL Bitar, Z., Francis, Z., Guatelli, S., Ivanchenko, A., Ivanchenko, V., Karamitros, M., Lee, S.B., Maigne, L., Meylan, S., Murakami, K., Nieminen, P., Payno, H., Perrot, Y., Petrovic, I., Pham, Q.T., Ristic-Fira, A., Santin, G., Sasaki, T., Seznec, H., Shin, J.I., Stepan, V., Tran, H.N., Villagrasa, C., The Geant4-DNA Collaboration, 2014. Simulating radial dose of ion tracks in liquid water simulated with Geant4-DNA: A comparative study, *Nucl. Instrum. Meth. B*. **333**, 92-98.

Kanasaki, M., Jinno, S., Sakaki, H., Kondo, K., Oda, K., Yamauchi, T., Fukuda, Y., 2016. The precise energy spectra measurement of laser-accelerated MeV/n-class high-Z ions and protons using CR-39 detectors, *Plasma Physics and Controlled Fusion* **58**, 034013.

Kanazawa, M., Hojo, S., Sugiura, A., Honma, T., Tashiro, K., Okada, T., Kamiya, T., Takahashi, Y., Suzuki, H., Uchihori, Y., Kitamura, H., 2010. Present operational status

of NIRS cyclotrons. In : Proceedings of the 19th International Conference on Cyclotrons and their Applications. Lanzhou, China.

Katz, R., Pinkerton, F.E., 1975. Response of nuclear emulsion to ionizing radiation, *Nucl. Instrum. Methods* **130**, 105-119.

Kodaira, S., Yasuda, N., Konishi, T., Kitamura, H., Kurano, M., Kawashima, H., Uchihori, Y., Ogura, K., Benton, E.R., 2013. Caribration of CR-39 with atomic force microscope for the measurement of short range tracks from proton-induced target fragmentation reactions, *Radiat. Meas.* **50**, 232-236.

Kodaira, S., Konishi, T., Kobayashi, A., Maeda, T., Ahbrizal, T., Ahmad, F.T., Yang, G., Akselrod, M.S., Furusawa, Y., Uchihori, Y., 2015. Co-visualization of DNA damage and ion traversals in live mammalian cells using a fluorescent nuclear track detector, *J. Radiat. Res*. **56**, 360-365.

Kondo, M., Shinozaki, Y., 1980. Radiation Chemistry, Corona Publishing CO., LTD., Tokyo, Japan (written in Japanese).

Kusumoto, T., Mori, Y., Kanasaki, M., Ueno, T., Kameda, Y., Oda, K., Kodaira, S., Kitamura, H., Barillon, R., Yamauchi, T., 2015. Yields on the formation of OH groups and the loss of CH groups along nuclear tracks in PADC films, *Radiat. Meas.* **83**, 59-62.

Kusumoto, T., Mori, Y., Kanasaki, M., Ikenaga, R., Oda, K., Kodaira, S., Kitamura, H., Barillon, R., Yamauchi, T., 2016a. Radiation chemical yields for the losses of typical functional groups in PADC films for high energy protons registered as unetchable tracks, *Radiat. Meas.* **87**, 35-42.

Kusumoto, T., Mori, Y., Kanasaki, M., Oda, K., Kodaira, S., Honda, Y., Tojo, S., Barillon, R., Yamauchi, T., 2016b. Sudden increase of the radiation chemical yield for loss of carbonate ester in PADC detector where the track overlapping of 28 MeV electrons becomes significant, *JPS. Conf. Proc*. **11**, 010001.

Kusumoto, T., EL Bitar, Z., Okada, S., Gillet, P., Arbor, N., Kanasaki, M., Oda, K., Nourredine, A.M., Kurashige, H., Fromm, M., Cloutier, P., D Bass, A., Sanche, L., Barillon, R., Yamauchi, T., 2017b. Radial electron fluence around ion tracks as a new

physical parameter for the detection threshold of PADC using Geant4-DNA toolkit, *ICNTRM2017*.

Lounis-Mokrani, Z., Badreddine, A., Mebhah, D., Imatoukene, D., Fromm, M., Allab, M., 2008. Determination of the proton latent track dimensions in CR-39 detectors using small angle neutron scattering, *Radiat*. *Meas*. **43**, 41-47.

Malek, M.A., Chong, C.S., 2000. FTIR study of H_2O in polyallyl diglycol carbonate, *Vib. Spectrosc*. **24**, 181-184.

Miterev, A.M., 1995. Calculation of track parameters of heavy ions in amorphous media, *High Energ. Chem*. **31**, 173-178.

Mori, Y., Ikeda, T., Yamauchi, T., Sakamoto, A., Chikada, H., Honda, Y., Oda, K., 2009. Radiation chemical yield for loss of carbonate ester bonds in PADC films exposed to gamma ray, *Radiat. Meas.* **44**, 211-213.

Mori, Y., Yamauchi, T., Kanasaki, M., Maeda, Y., Oda, K., Kodaira, S., Konishi, T., Yasuda, N., Barillon, R., 2011. Radiation chemical yields for loss of ether and carbonate ester bonds in PADC films exposed to proton and heavy ion beams, *Radiat. Meas.* **46**, 1147-1153.

Mori, Y., Yamauchi, T., Kanasaki, M., Hattori, A., Matai, Y., Matsukawa, K., Oda, K., Kodaira, S., Kitamura, H., Konishi, T., Yasuda, N., Tojo, S., Honda, Y., Barillon, R., 2012. Greater radiation chemical yields for losses of ether and carbonate ester bonds at lower stopping powers along heavy ion tracks in poly(allyl diglycol carbonate) films, *Appl. Phys. Express* **5**, 086401.

Mori, Y., Yamauchi, T., Kanasaki, M., Hattori, A., Oda, K., Kodaira, S., Konishi, T., Yasuda, N., Tojo, S., Honda, Y., Barillon, R., 2013. Vacuum effects on the radiation chemical yields in PADC films exposed to gamma rays and heavy ion, *Radiat. Meas.* **50**, 97-102.

Mori, Y., 2014. Structural modification along nuclear tracks of proton and heavy ions in poly(allyl diglycol carbonate) detectors, Ph.D. thesis.

Morishima, M., 2016. Cosmic-ray imaging of Fukushima Daiichi nuclear power plant, *Jounal of the Society of Photograpy and Imaging of Japan* **79**, 42-47. (written in Japanese)

Morishima, K., Kuno, M., Nishio, A., Kitagawa, N., Manabe, Y., Moto, M., Takasaki, F., Fujii, H., Satoh, K., Kodama, H., Hayashi, K., Odaka, S., Procureur, S., Attié, D., Bouteille, S., Calvet, D., Filosa, C., Magnier, P., Mandjavidze, I., Riallot, M., Marini, B., Gable, P., Date, Y., Sugiura, M., Elshayeb, Y., Elnady, T., Ezzy, M., Guerriero, E., Steiger, V., Serikoff, N., Mouret, J.-B., Charlés, B., Helal, H., Tayoubi, M., 2017. Discovery of a big void in Khufu's Pyramid by observation of cosmic-ray muons, *Nature* **552**, 386-390.

Nishiuchi, M., Sakaki, H., Esrikepov, T.Zh., Nishio, K., Pikuz, T.A., Faenov, A.Ya., Skobelev, I.Yu., Orlandi, R., Sako, H., Pirozhkov, A.S., Matsukawa, K., Sagisaka, A., Ogura, K., Kanasaki, M., Kiriyama, H., Fukuda, Y., Koura, H., Kando, M., Yamauchi, T., Watanabe, Y., Bulanov, S.V., Kondo, K., Imai, K., Nagamiya, S., 2015. Acceleration of highly-charged GeV Fe ions from a low-Z substrate by intense femtosecond laser, *Phys. Plasmas* **22**, 033107.

Oda, K., Yoshida, K., Yamauchi, T., 1997. Effects of low-LET radiations on CR-39 track detector, *Radiat. Meas.* **28**, 85-88.

Oda, K., Imasaka, Y., Yamauchi, T., Nakane, Y., Endo, A., Tawara, H., Yamaguchi, Y., 2005. Radiator design for detecting high-energy neutrons with a nuclear track detector, *Radiat. Meas.* **40**, 570-574.

Oganesyan, V.R., Trofimov, V.V., Gaillard, S., Fromm, M., Danziger, M., Hermsdorf, D., Orelovitch, O.L., 2005. Investigation of the response of thin CR-39 polymer foils irradiated with light ions, *Nucl. Instrum. Meth. B* **236**, 289-294.

Ogura, K., Hattori, T., Asano, M., Yoshida, M., Omichi, H., Nagaoka, N., Kubota, H., Katakai, R., Hasegawa, H., 1997. Proton response of high sensitivity CR-39 copolymer, *Radiat. Meas.* **28**, 197-200.

Ogura, K., Asano, M., Yasuda, N., Yoshida, M., 2001. Properties of TNF-1 track etch detector, *Nucl. Instrum. Meth. B*. **185**, 222-227.

Ounoughi, N., Mavon, C., Belafrites, A., Groetz, J.-E., Fromm, M., 2013. Beam Characterization of a lab bench cold chthode ultra-soft x-ray generator, *Nucl. Instrum. Meth. B* **305**, 61-66.

Price, P.B., Walker, R.M., 1962. Chemical etching of charged particle tracks in solids, *J. Appl. Phys*. **33**, 3407-3412.

Rowntree, P., Parenteau, L., Sanche, L., 1991a. Anion yields produced by low-energy electron impact on condensed hydrocarbon films, *J. Phys. Chem.* **95**, 4902-4909.

Rowntree, P., Parenteau, L., Sanche, L., 1991b. Dielectric polarization invarlance in dissociative electron attachment from condensed saturated hydrocarbons, *J. Phys. Chem.* **95**, 523-524.

Sakamoto, A., Mori, Y., Kanasaki, M., Yamauchi, T., Oda, K., 2010. Quantum yields for loss of carbonate ester bonds in polymeric nuclear track detectors under 222 nm UV radiation, *Review of Graduate School of Maritime Sciences, Kobe University* **7**, 87-98 (written in Japanese).

Salehpour, M., Hakansson, P., Sundqvist, B., 1984. Damage cross sections for fast heavy ion induced desorption of biomolecules, *Nucl. Instrum. Meth. B* **2**, 752-756.

Sanche, L., 2000. Electron resonances in DIET, *Surface Science* **451**, 82-90.

Sato, T., Niita, K., Matsuda, N., Hashimoto, S., Iwamoto, Y., Noda, S., Ogawa, T., Iwase, H., Nakashima, H., Fukuhori, T., Okumura, K., Kai, T., Chiba, S., Fruta, T., Sihver, L., 2013. Particle and Heavy Ion Transport code System, PHITS, version 2.52, *J. Nucl. Sci. and Technol.* **50**, 913-923.

Schiwietz, G., Grande, P.L., 2001. Improved charge-state formulas, *Nucl. Instrum. Meth. B*. **175**, 125-131.

Seki, S., Tsukuda, S., Maeda, K., Matsui, Y., Saeki, A., Tagawa, S., 2004. Inhomogeneous distribution of crosslinks in ion tracks in polystyrene and polysilanes, *Phys. Rev. B* **70**, 144203.

Silk, E.C.H., Barnes, R.S., 1959. Examination of fission fragment tracks with an electron microscope, *Phil. Mag*. **4**, 970-972.

Somogyi, G., Szalay, S.A., 1973. Track-diameter kinetics in dielectric track detectors, *Nucl. Instrum. Meth.* **109**, 211.

Somogyi, G., Grabishe, K., Shcerzer, R., Enge, W., 1976. Revision of the concept of registration threshold in plastic track detectors, *Nucl. Instrum. Meth.* **109**, 211.

Tse, K.C.C., Nikezic, D., Yu, K.N., 2006. Photo-degradation of PADC by UV radiation at various wavelengths, *Polym. Degradation Stability* **91**, 2380-2388.

Tse, K.C.C., Nikezic, D., Yu, K.N., 2008. Effects of UVC irradiation on alpha-particle track parameters in CR-39, *Radiat. Meas.* **43**, S98-S101.

Waligórski, M.P.R., Hamm, R.N., Katz, R., 1986. The radial distribution of dose around the path of a heavy ion in liquid water, *Nucl. Tracks Radiat. Meas*. **11**, 309-319.

Yamauchi, Y., Taniguchi, T., Oda, K., Ikeda, T., Honda, Y., Tagawa, S., 1999. Dose-rate effects on the bulk etch-rate of CR-39 track detector exposed to low LET radiations, *Radiat. Meas*. **31**, 121-126.

Yamauchi, T., Ichijo, H., Oda, K., 2000. Gamma-ray and ion irradiation effects on the optical property of CR-39 detector and their latent track size, *Proceedings of the First International Symposium on Supercritical Water-cooled Reactor, Designed Technology (SCR-2000)* **407**, 274-287.

Yamauchi, T., 2003. Studies on the nuclear tracks in CR-39 plastics, *Radiat. Meas.* **36**, 73-81.

Yamauchi, T., Mineyama, D., Nakai, H., Oda, K., Yasuda, N., 2003a. Track core size estimation in CR-39 track detector using atomic force microscope and UV-Visible spectrophotometer, *Nucl. Instrum. Meth. B* **208**, 149-154.

Yamauchi, T., Nakai, H., Somaki, Y., Oda, K., 2003b. Formation of CO_2 gas and OH

groups in CR-39 plastics due to gamma-ray and ions irradiation, *Radiat. Meas.* **36**, 99-103.

Yamauchi, T., Somaki, Y., Nakai, H., Oda, K., Ikeda, T., Honda, H., Tagawa, S., 2003c. Oxidative degradation of CR-39 track detector in the surface region during gamma-irradiation, *Nucl. Instrum. Meth. B* **208**, 489-494.

Yamauchi, T., Yasuda, N., Asuka, T., Izumi, K., Masutani, T., Oda, K., Barillon, R., 2005a. Track core size estimation for heavy ions in CR-39 by AFM and UV methods, *Nucl. Instrum. Meth. B* **236**, 318-322.

Yamauchi, T., Barillon, R., Balanzat, E., Asuka, T., Izumi, K., Masutani, T., Oda, K., 2005b. Yields of CO_2 formation and scissions at ether bonds along nuclear tracks in CR-39, *Radiat. Meas.* **40**, 224-228.

Yamauchi, T., Mori, Y., Oda, K., Yasuda, N., Kitamura, H., Barillon, R., 2008a. Structural modification along heavy ion tracks in poly(ally diglycol carbonate) films, *Jpn. J. Appl. Phys.* **47**, 3606-3609.

Yamauchi, T., Watanabe, S., Seto, A., Oda, K., Yasuda, N., Barillon, R., 2008b. Loss of carbonate ester bonds along Fe ion tracks in thin CR-39 films, *Radiat. Meas.* **43**, 106-110.

Yamauchi, T., Mori, Y., Oda, K., Yasuda, N., Barillon, R., 2010. On the tracks of proton and heavy ions in PC and PADC plastics detectors, *KEK Proc. Radiation Detectors and Their Uses*, 1-6.

Yamauchi, T., Mori, Y., Morimoto, A., Kanasaki, M., Oda, K., Kodaira, S., Konishi, T., Yasuda, N., Tojo, S., Honda, Y., Barillon, R., 2012. Thresholds of Etchable Track Formation and Chemical Damage Parameters in Poly(allyl diglycol carbonate) films at the stopping powers ranging from 10 to 12,000 keV/μm, *Jpn. J. Appl. Phys*., **51**, 056301.

Yamauchi, T., Kusumoto, T., Mori, Y., Kanasaki, M., Oda ,K., Kodaira, S., Barillon, R., 2017. Distinct step-like changes of G values for the losses of typical functional groups in poly(ethylene terephthalate) along B ion tracks around the detection threshold, *ICNTRM 2017*.

Yildrim, Y., Balcan, M., D Bass, A., Cloutier, P., Sanche, L., 2010. Electron stimulated desorption of anions and cations from condensed allyl glycidyl ether, *Phy. Chem. Chem. Phys*. **12**, 7950-7958.

Young, D.A., 1958. Etching of radiation damage in lithium fluoride, *Nature* **182**, 1958.

Ziegler, J.F., 2004. SRIM-2003, *Nucl. Instrum. Meth. B*. **219-220**, 1027-1036.

Zylstra, A.B., Frenje, J.A., Séguin, F.H., Gatu Johnson, M., Casey, D.T., Rosenberg, M.J., Waugh, C., Sinenian, N., Manuel, M.J.-E., Li, C.K., Petrasso, R.D., Kim, Y., Herrmann, H.M., 2012. A new model to account for track overlap in CR-39 data, *Nucl. Instrum. Meth. A*. 68, 184-190.